A Comparison of the Effects of Local and Global Environment on Galaxy Evolution in Low Redshift Galaxy Clusters

by

Brittany Howard
B.Sc., University of Michigan - Dearborn, 2017

A Thesis Submitted in Partial Fulfillment of the
Requirements for the Degree of

MASTER OF SCIENCE

in the Department of Physics and Astronomy

A Comparison of the Effects of Local and Global Environment on Galaxy Evolution in Low Redshift Galaxy Clusters

by

Brittany Howard
B.Sc., University of Michigan - Dearborn, 2017

Supervisory Committee

Dr. J. Willis, Supervisor
(University of Victoria Department of Physics and Astronomy)

Dr. L. Simard, Co-Supervisor
(University of Victoria Department of Physics and Astronomy)

ABSTRACT

Using the redMaPPer catalog of 21709 galaxy clusters and photometric information for 455946 galaxies from SDSS DR8, we study the effects of local and global environment on galaxy evolution within clusters in the redshift range $0.2 \leq z \leq 0.5$ and the richness range $20 \leq \lambda \leq 236$. We use cluster richness λ as a proxy for global environment and cluster-centric radius d_{BCG} to represent the local environment within clusters. We measure giant-to-dwarf ratio (GDR) which gives insight regarding the composition of the red sequence, and we measure red fraction which holds information about the rate at which galaxies falling into clusters cease to form new stars and build up the red sequence in a phenomenon called quenching. We observe that red fraction decreases with redshift, increases with λ, and decreases with d_{BCG}. GDR, meanwhile, decreases with redshift, does not vary significantly with λ, and decreases with d_{BCG}. All together, our results tell the story of clusters starting with bright, massive galaxies which accrete smaller and smaller galaxies over time. The galaxies are quickly quenched upon entering clusters environment. We observe that most quenching occurs on smaller richness scales than our data covers, and that by the time clusters have grown to the richnesses redMaPPer is sensitive to, ram pressure stripping is likely to be the dominant quenching mechanism.

Contents

List of Tables

List of Figures

List of Equations

Acknowledgements

I would like to thank:

Jon Willis, for direction, encouragement, and advice. Thank you also for the many meetings spent talking about sea creatures and geology.

Maan Hani, for helping me squash bugs in my code, for late night curry in the office, for coaching me in soccer, and for making work fun.

Mallory Thorp, for being my writing buddy, teaching me to knit, and always knowing exactly what to say.

Ruth Digby, for being my other writing buddy and for all of the delicious desserts.

Myself, for finally finishing this.

Dedication

To my parents. Thank you for the love, encouragement, education, and support.
My success is your success.

Glossary

Background subtraction: Monte Carlo method To isolate the cluster members from an aperture's worth of galaxies, we define a probability for each galaxy to be a cluster member based on its position in color-magnitude space. Cluster member galaxies are selected using a Monte Carlo approach with this probability (Pimbblet et al., 2002; Urquhart et al., 2010). See Section 3.5.

Background subtraction: statistical method Color-magnitude diagrams are created for a stacked sample of cluster aperture galaxies and for a scaled sample of field galaxies. The latter is subtracted from the former, leaving the distribution of cluster member galaxies typical of the stacked sample of clusters (De Lucia et al., 2007; Bildfell et al., 2012). See Section 4.1.2.

Blue cloud A term used in the literature for cluster member galaxies which are not members of the red sequence; these galaxies are star-forming and therefore have not experienced quenching. See Section 1.3.

Bremsstrahlung German for "breaking radiation". The radiation that results from the deceleration of a charged particle when it is deflected electromagnetically by another charged particle. The ICM emits radiation via bremsstrahlung which allows the detection of galaxy clusters in the X-ray regime. See Section 1.7.2.

Brightest Cluster Galaxy (BCG) The galaxy used by redMaPPer to represent the projected centroid of each galaxy cluster. BCGs are the brightest and most massive galaxies in their clusters.

Butcher-Oemler effect A strong bimodality in color-magnitude space among cluster member galaxies. Two populations of galaxies naturally emerge from clusters: the red sequence and the blue cloud, which represent the quenched and un-quenched populations respectively. This effect becomes more pronounced in denser environments. See Section 1.4.

Cosmological distance modulus The relationship between apparent and absolute magnitude as a function of redshift, taking into account the evolution of the object's spectrum and the filter through which the object is observed. Given by Equation 3.1 and described in Section 3.2.

Cluster aperture galaxies Galaxies which are present in a cluster aperture before performing background subtraction. They comprise of galaxies which are true members of the cluster as well as contaminating field galaxies from the background or foreground. Background subtraction is needed to filter out these contaminating galaxies.

Cluster member galaxies Galaxies which remain in a cluster aperture after performing background subtraction. These galaxies are true members of the cluster.

Colour-Magnitude Diagram (CMD) A diagram on which cluster member galaxies are plotted in color-magnitude space to reveal their bimodality. See Figures 3.8 and 3.12 for examples of CMDs before and after background subtraction, respectively.

Cosmic Microwave Background (CMB) The residual heat from the universe's formation which has a temperature of $T \approx 2.7$ K and emits in millimeter wavelengths. We can exploit the Sunyaev-Zel'dovicheffect to detect galaxy clusters in observations of the CMB; see Section 1.7.3.

d_5 The distance (measured in kpc in this thesis) between a cluster member galaxy and its fifth nearest neighbor galaxy within the cluster. Representative of the local environment inside a cluster. See Section 4.3.

Dark matter halo The dark matter associated with a galaxy cluster which dominates the cluster's mass budget. See Section 1.2.

(e+k) correction When an astronomical object is observed through a filter, $k_\lambda(z)$ is the k-correction factor which accounts for the filter through which the source is observed, and $e_\lambda(z)$ is a correction factor which accounts for the source's evolution with redshift. $k_\lambda(z) + e_\lambda(z)$ is known as the (e+k) correction; see Section 3.2.1.

Field galaxy A galaxy which is not a member of a cluster or group; field galaxies constitute the sample of "background" galaxies used in this thesis for background subtraction.

Galaxy cluster A region of space characterized by an over-density of galaxies, a dark matter halo, and hot, diffuse baryonic material known as the ICM. See Section 1.2.

Galaxy group A smaller version of a galaxy cluster. Due to the hierarchical model of structure formation in the universe, galaxy groups will merge or accrete smaller objects to become clusters.

Giant-to-dwarf ratio (GDR) The ratio of number of giant galaxies to number of dwarf galaxies within the red sequence of a cluster, where the distinction between giant and dwarf galaxies is some characteristic luminosity. See Section 1.8.2.

Harassment When a galaxy is in a dense environment, several smaller galaxies make passes by the galaxy in question, not merging but pulling small amounts of matter - particularly star-forming cold gas- to regions of lower gravitational potential and sometimes ripping them free of the original galaxy altogether. Contributes to quenching and occurs preferentially outside the group's or cluster's virial radius (Boselli et al., 2016). See Section 1.5.

Intra-Cluster Medium (ICM) The hot plasma and gas that fills the space between galaxies in a galaxy cluster. The ICM is not associated with individual galaxies, but rather with the cluster as a whole. It emits bremsstrahlung radiation in the X-ray regime. See Section 1.7.2.

Inverse Compton scattering Occurs when an electron of high kinetic energy interacts with a photon of a lower energy. When the electron and photon interact, the photon absorbs some of the electrons energy and has a higher frequency than it had before scattering. Inverse Compton scattering of CMB photons off the electrons in a galaxy cluster's ICM create the Sunyaev-Zel'dovicheffect.

Ram pressure stripping When a galaxy enters a dense environment, it tends to lose its hot gas halo, and winds generated by supernovae and active galactic nuclei become very efficient at blowing the remaining cool gas from the galaxy, effectively leaving no raw material with which to form new stars. This effect is referred to in the literature as ram pressure stripping. See Section 1.5.

Richness (of a galaxy cluster) A quantity portraying the scaled number of galaxies within a cluster. Represents the global environment within the cluster. See Section 2.3 for details on redMaPPer 's richness estimator λ.

Red fraction The fraction of a cluster's member galaxies which lie along the red sequence. See Section 1.8.1.

Red sequence The fraction of a galaxy cluster's member galaxies which lie along the red sequence. We can use the red fraction to gain insight about the rate at which galaxies are quenched within clusters. See Section 1.8.1.

redMaPPer The survey of galaxy clusters analyzed in this thesis; for a full description of the dataset and the algorithm used to detect the clusters, see Section 2.2.

Sloan Digital Sky Survey (SDSS) A large survey designed to photometrically image 104 square degrees of the sky. Its eighth data release is the source of the photometric data used in this thesis. See section 2.1 for details.

Sunyaev-Zel'dovicheffect Phenomenon which creates deficits in the brightness of the CMB when its photons interact with a galaxy clusters hot ICM via inverse Compton scattering. Allows the detection of galaxy clusters in the millimeter-wavelength regime. See Section 1.7.3.

Threshing Another term used in the literature for harassment. See Section 1.5.

Quenching A term used in the literature to describe galaxies which experience a suppression and eventual cessation of star formation. Occurs due to internal effects based on galaxy mass as well as external effects based on environment. The mechanisms which cause quenching under varying circumstances are debated. See Section 1.4.

Weak lensing The phenomenon by which massive objects such as galaxy clusters distort spacetime in such a way that light curves around them, effectively acting as lenses. Weak lensing causes background galaxies to appear stretched along an arc centered on the galaxy clusters center of mass. We can take advantage of weak lensing to identify galaxy clusters. See Section 1.7.4.

4000 Ångstrom break A distinct discontinuity visible in the spectrum of galaxies at 4000 Ångstroms in the rest-frame. See the model stellar population spectrum in Figure 3.4 for an example.

Chapter 1

Introduction

1.1 The history of the study of galaxy clusters

Originally, galaxy clusters were identified as regions of overdensity in the number of "nebulae" (at the time, people did not realize these nebulae were in fact galaxies) visible in the sky. Astronomers such as William Herschel and Charles Messier were among the first to catalog these clusters (Messier, 1783, 1784). As our observational technology improved, the evidence accumulated for these nebulae's tendency to cluster. In the 1920's, Edwin Hubble determined the nebulae were in fact galaxies at great distances (Hubble, 1925, 1926). Astronomers realized then that the clusters of nebulae that they had been observing were really clusters of galaxies, and they were of gargantuan physical size.

The next major discovery involving galaxy clusters was the enormous mass they encompass. Hubble & Humason (1931) measured the velocities of galaxies near clusters, and along with the assumption that the galaxies within the clusters were sufficiently relaxed to obey the virial theorem, these measurements were used to determine the total cluster masses for the Coma and Virgo clusters by Fritz Zwicky (Zwicky & Andernach, 1933; Zwicky, 1937) and Smith & Sinclair (1936), respectively. For a galaxy cluster to be in a state of virial equilibrium simply means that its member galaxies obey the virial theorem, given by:

$$2K + U = 0, \tag{1.1}$$

where K is the time-averaged total kinetic energy of the cluster galaxies, and U is their time-averaged total potential energy. The virial theorem is used to describe stable, gravitationally-bound systems, such as galaxy clusters.

A great surprise came with these measurements: the measured mass of each cluster as implied by the velocity dispersion of its associated galaxies was about 300 times greater than the combined mass of all of the stars associated with the galaxies within that cluster. To remedy this discrepancy, Zwicky proposed that the galaxy clusters must contain some sort of material which interacts gravitationally but is not visible. He named this material "dark matter" and asserted that galaxy clusters must be composed of primarily dark matter by mass fraction.

The existence of dark matter was - and still is - debated. However, the case for dark matter was bolstered when we began to observe the sky at X-ray wavelengths and discovered the extended hot intracluster medium (ICM) in the 1970's. The ICM is the result of thermal bremsstrahlung radiation (described in Section 1.7.2) in X-ray energies which was found to smoothly fill the space between galaxies within galaxy clusters (e.g. Cavaliere & Colafrancesco, 1989; Gursky et al., 1972; F. Meekins et al., 1971; Forman et al., 1972; Kellogg et al., 1973).

Using X-ray detectors, the temperature of the ICM was measured, and it was such that additional mass besides the visible stellar mass and ICM was needed to build up the gravitational potential well of the clusters to an appropriate depth to explain the high velocity dispersions of galaxies in clusters. This was an independent set of measurements from Zwicky's original argument for dark matter, and as such lent additional credence to the idea.

Another method of detecting galaxy clusters came with the discovery of the Sunyaev-Zel'dovich effect, in which photons from the cosmic microwave background (CMB) interact with the thermal electrons of the hot ICM through inverse Compton scattering (e.g. Sunyaev & Zeldovich, 1970, 1972; Sunyaev & Zel'dovich, 1980). Through this mechanism, the CMB appears slightly dimmer in the regions where clusters lie, and we can exploit this fact to survey for clusters. See Section 1.7.3 for more details.

Another innovation is the ability to search the sky for instances of gravitational lensing. Weak lensing, in particular, is a signature of the great mass held by the dark matter halo of a cluster. Gravitational lensing occurs when a very massive object - like a galaxy cluster - distorts local spacetime so that nearby light's path is altered, effectively acting as a lens. By searching for instances of gravitational lensing in the sky, we can identify galaxy clusters and gain insight regarding their mass. Weak lensing is the most frequently-observed manifestion of gravitational lensing for galaxy clusters, simply because of the precise alignment required for strong lensing. See

Section 1.7.4 for further details.

1.2 Components of a galaxy cluster

Simply put, a galaxy cluster is an overdensity of galaxies in virial equilibrium encompassed by a dark matter halo and a field of hot diffuse plasma known as the intra-cluster medium (ICM).

To unpack this definition, let us first focus on the baryonic component of a galaxy cluster; the baryons in the cluster are responsible for emitting all of the light emitted by the cluster. The galaxies in a cluster must be in sufficiently close proximity to be gravitationally bound to each other, they must be present with a greater number density than elsewhere in the universe, and they must have been clustered together long enough to be in a state of virial equilibrium (see Equation 1.1). The galaxies in clusters follow a consistent luminosity function, several examples of which are shown in Figure 1.8.

Just how overdense is a galaxy cluster? If ρ_0 is the typical density of galaxies in the field, then the core of a rich cluster would host a density of galaxies $\approx 100\rho_0$ (Geller & Huchra, 1989).

The other baryonic component of a galaxy cluster is its ICM. It consists of diffuse plasma which is not associated with individual galaxies within the cluster. The ICM is hot, with a temperature $T \approx 10^7 - 10^8$ K (Sarazin, 1986). Of the baryonic matter in a typical galaxy cluster, most of the mass is in the ICM rather than in the stellar component (galaxies). Figure 1.2 illustrates this well; we observe a tight correlation between the mass of a galaxy cluster's ICM and the mass of its stellar component, and we note that the ICM tends to be approximately 10 times more massive than the galaxies within a cluster (Giodini et al., 2009; Kravtsov & Borgani, 2012; Lin et al., 2011).

Galaxy clusters also have a non-baryonic component: a halo of dark matter. In fact, their mass budget is strongly dominated by dark matter. The Coma cluster, for example, is composed of 85% dark matter, 14% baryons in the ICM, and 1% baryons in galaxies (Łokas & Mamon, 2003). Figure 1.3 provides some exemplary images of galaxy clusters which highlight all three of the components described above.

Two well-known examples of nearby galaxy clusters are Virgo and Coma. Virgo is the richest galaxy cluster within 35 Mpc, and because of its richness and proximity, is also the most thoroughly-studied galaxy cluster (Boselli et al., 2018). It is quite close,

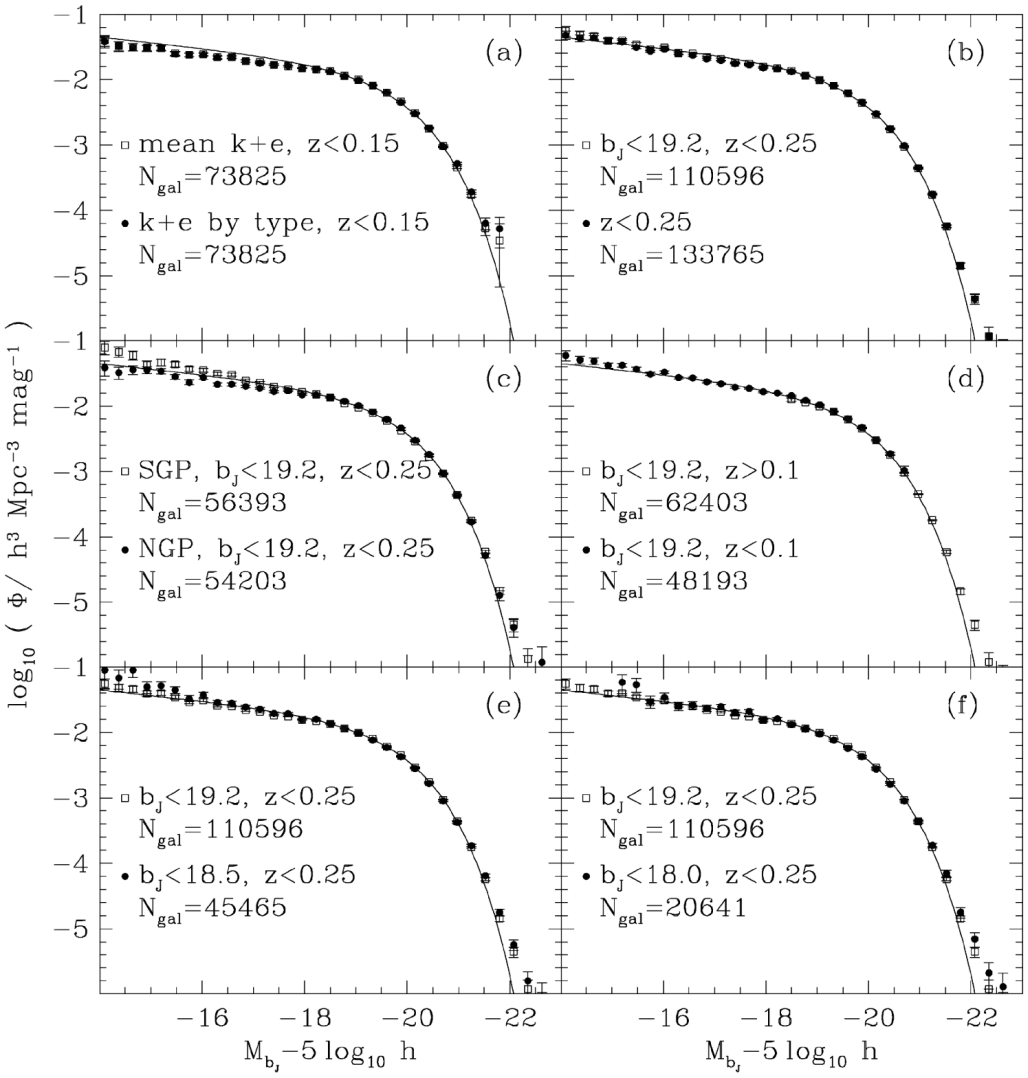

Figure 1.1: Luminosity functions for different sub-populations of galaxies from the2dF galaxy redshift survey (2dFGRS) (Norberg et al., 2002). The y-axes are a measure of the number of galaxies while the x-axes represent luminosity. The sub-populations are separated by redshift and apparent b_j magnitude. The smooth curves are Schechter functions fitted to the data. Note how for all bins, the luminosity function is nearly the same. Figure from Norberg et al. (2002).

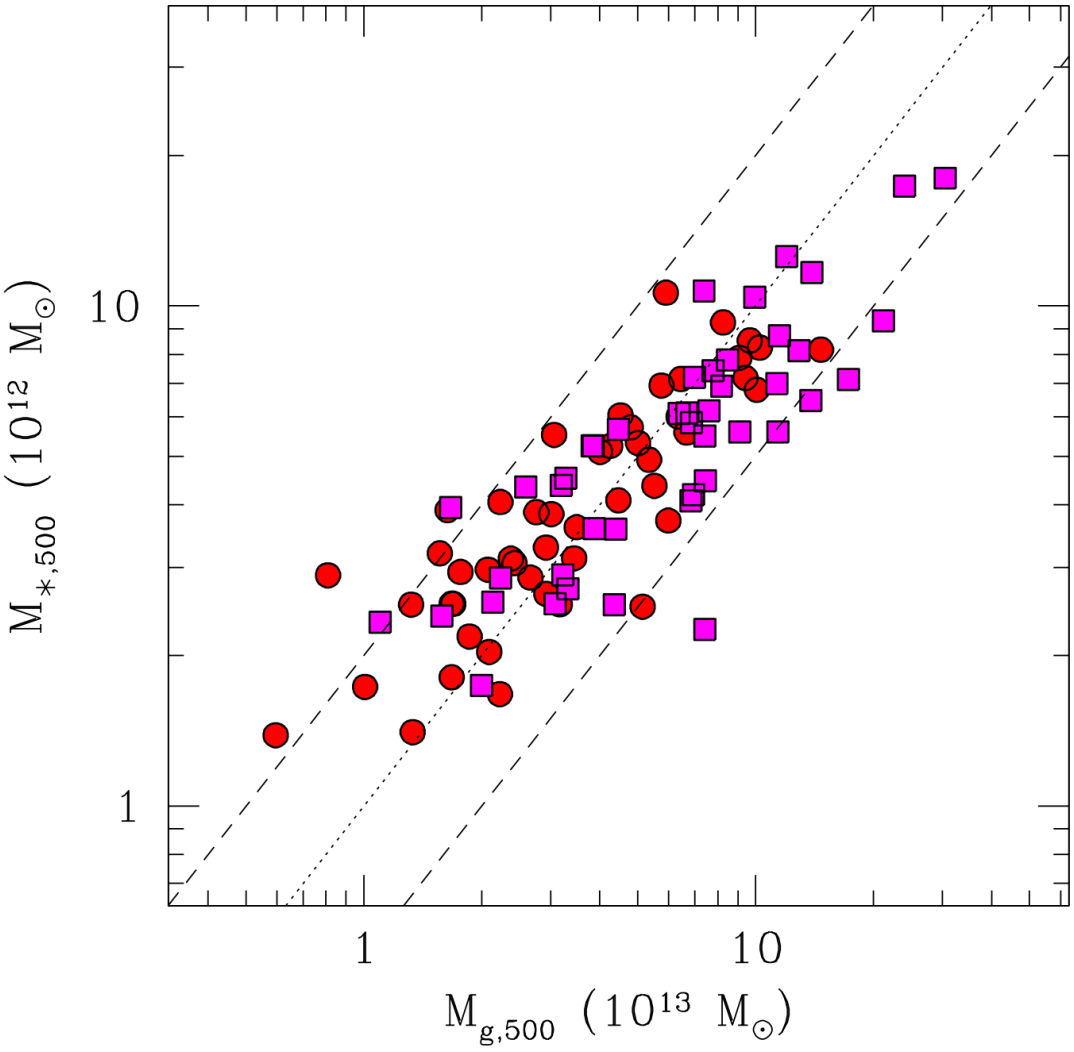

Figure 1.2: Stellar versus ICM mass within galaxy clusters. All masses are measured within the radius R_{500}, the radius enclosing a mean overdensity of $\Delta_c = 500\rho_{cr}$. Red circles show clusters with redshift $z < 0.1$, and magenta squares show higher-redshift clusters with $0.1 < z < 0.6$ (Lin et al. (2011)). The dotted line corresponds to the constant stellar-to-gas mass ratio $M_{,500}/M_{g,500} = 0.1$, while the dashed lines correspond to the values of 0.05 and 0.2 for this ratio. Figure from Kravtsov & Borgani (2012).

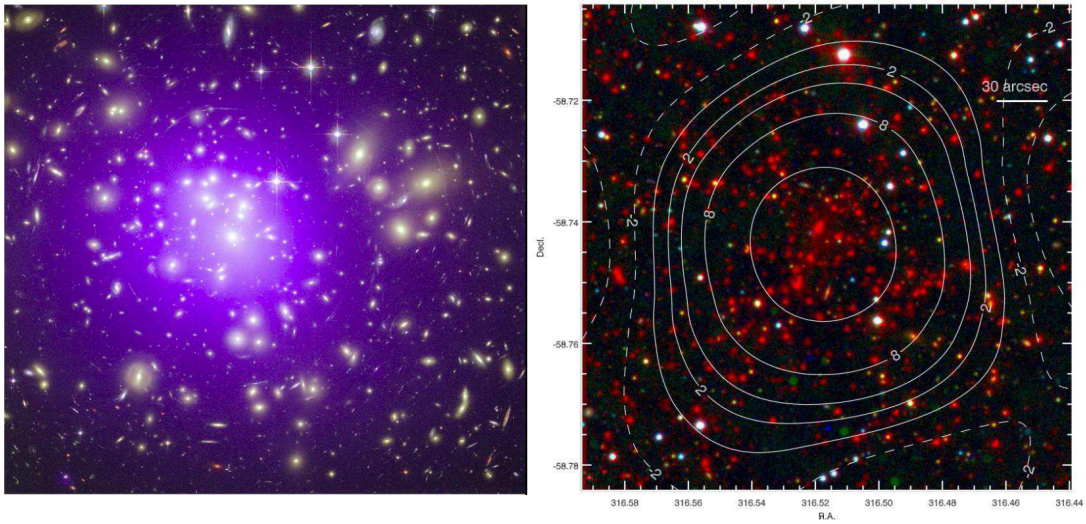

Figure 1.3: Example multi-band galaxy cluster images. The left panel shows the composite X-ray/optical image of the galaxy cluster Abell 1689. The scale of the image is 556 x 556 kpc, and the cluster is at redshift $z = 0.18$. Optical images of the galaxies are colored in yellow and were taken with the Hubble Space Telescope. The purple haze is X-ray emission from ICM of temperature $T \approx 10^8$ K, and it was observed by the Chandra X-ray Observatory (see Section 1.7.2 for more details on X-ray emission in galaxy clusters). Gravitational lensing effects are visible as the arced elongations of the background galaxies in the image. For more details on weak lensing, see Section 1.7.4. (Image credit: X-ray: NASA/CXC/MIT; Optical: NASA/STScI). The right panel shows the galaxy cluster SPT-CL J2106-5844, which is the most massive known cluster of redshift greater than 1 (its redshift is $z = 1.133$) discovered as a result of the Sunyaev-Zeldovich effect (see Section 1.7.3). The color image is the Magellan/LDSS3 optical and Spitzer/IRAC mid-infrared measurements corresponding to the blue-green-red color channels. The image size is 2.4 x 2.4 Mpc. The white contours correspond to the South Pole Telescope Sunyaev-Zel'dovich effect significance values, as labeled, and dashed contours are used for the negative significance values. (Image credit: Foley et al. (2011)). Figure from Kravtsov & Borgani (2012).

at a distance of only 16.5 Mpc (Gavazzi & Soucail, 2006; Mei et al., 2007; Blakeslee et al., 2009), and it contains a mass $M_{200} = (2.8\pm\ 1.4) \times 10^{14}$ $M_\odot$. [1] (Nulsen & Bohringer, 1995; Schindler et al., 1998; McLaughlin, 1998; Urban et al., 2011). The Virgo cluster's viral radius is 740 kpc (Su et al., 2019) [2].

The Coma cluster, on the other hand, is farther away at a distance of 106.11 ± 7.43 Mpc (Struble & Rood, 2002), but more massive with a mass of $M_{200} = (4.50\pm\ 0.48) \times 10^{14}$ $M_\odot$ (Rines et al., 2016). It has a virial radius of $2.9h_{70}^{-1}$ Mpc (Łokas & Mamon, 2003); assuming $h_{70} = 0.7$, the Coma cluster's virial radius is 420 kpc.

1.3 Color bimodality in cluster member galaxies

Having defined galaxy clusters, why are they interesting to study? The hierarchical model of galaxy formation states that all structure in the universe starts as small regions of overdensity which grow over time through accretion and mergers, becoming larger and more massive as time passes. As the largest structures currently visible in the universe, galaxy clusters represent the most evolved regions in the universe, so we may be able to see phenomena within in them which are not manifest in any other environments. One such phenomena is quenching, which will be discussed in Section 1.4. Another is the existence of a colour-magnitude relation known as the red sequence, which will be discussed later in this section.

Clusters are one of a few classes of environment that one typically uses to compare regions of the universe. The majority of the universe, where galaxies are present at a relatively low concentration, is called the field. Regions of the universe which contain the densest concentrations of galaxies are called galaxy clusters. Somewhere between these two extremes are galaxy groups. As collections of galaxies have a continuous mass range, the cutoff point between galaxy group and galaxy cluster is arbitrary, and the exact mass value chosen varies in the literature. Typically, though, one takes a mass of $10^{14}m_\odot$.

One interesting property of galaxy clusters is the natural division of their member galaxies into two relatively distinct classes. As shown by Baldry et al. (2006) in Figure 1.4, as galaxies enter increasingly dense environments, a greater proportion

[1] M_{200} is defined as the total mass within the radius at which the mean mass density is 200 times larger than the critical cosmic mass density.

[2] The virial radius of a cluster is the radius within which its member galaxies obey the virial theorem given by Equation 1.1; it is conventionally the radius at which the mean mass density is 200 times larger than the critical cosmic mass density.

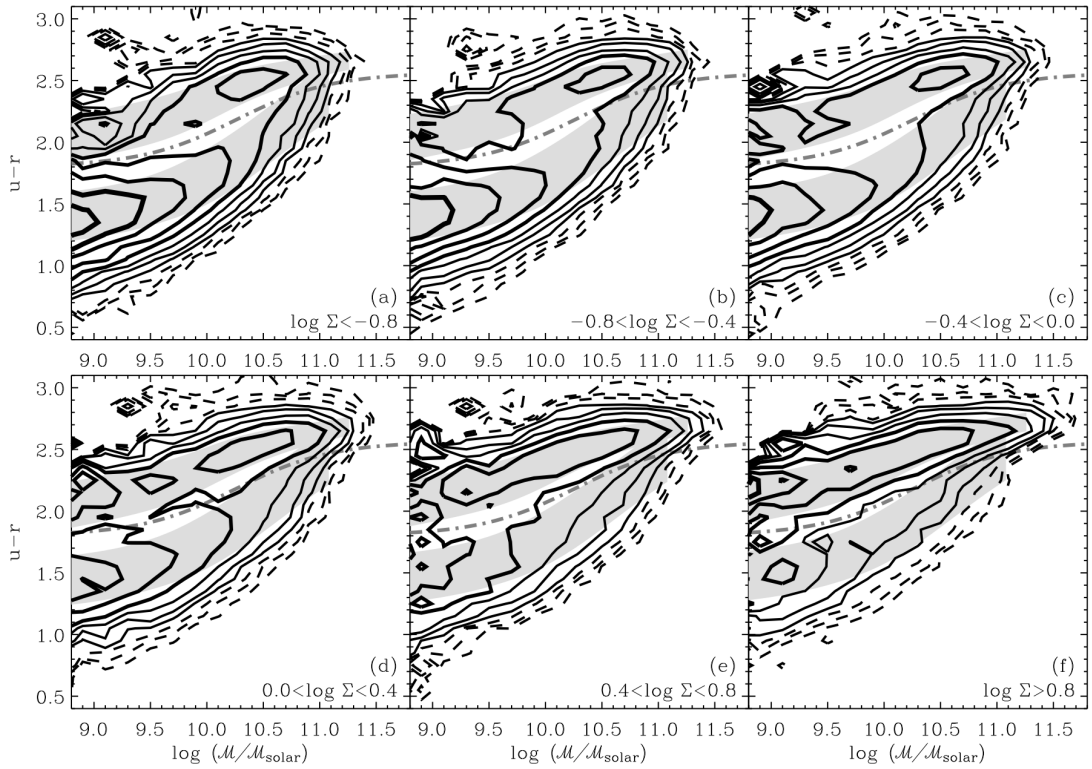

Figure 1.4: Colour versus stellar mass relations for different environments in increasing order of density. Panel (a) represents void-like environments while panel (f) represents cluster-like environments. The dashed and solid lines represent logarithmically-spaced density contours. The grey regions outline the red sequence and blue cloud. The dash-and-dotted lines show the best-fit divider between these two populations. Figure from Baldry et al. (2006).

of them become red in color as compared to galaxies in field environments. This is apparent when we progress from panels (a) through (f) and observe that the galaxy distribution becomes more strongly bimodal as the environment becomes denser, and that the redder group of galaxies - the upper shaded region in each of the panels - in particular becomes more dominant in denser environments. This colour-magnitude relation's existence has been known for decades (de Vaucouleurs & Gerard, 1961; Visvanathan & Sandage, 1977), and the evolution of the extent of this bimodality versus redshift and environment was originally known as the "Butcher-Oemler effect" (Butcher & Oemler, 1978, 1984).

The upper shaded region in Figure 1.4 is known as the red sequence, and it is a defining characteristic of galaxy clusters, present in clusters as early as $z \approx 1$ (Stanford et al., 1998; Bell et al., 2004; Mei et al., 2006). Indeed, many cluster

finding algorithms work by searching astronomical survey data for evidence of the red sequence (for more details, see Section 1.7.1). The red sequence represents the galaxies which have experienced a reduction or even cessation of star formation in a process known as quenching, which will be described in the following section.

Balogh et al. (2004) found that the mean position of the red sequence becomes marginally redder as environmental density increases. They compared galaxy clusters of a fixed luminosity to obtain these results. Baldry et al. (2004) and Rykoff et al. (2014) confirmed these observations. As a cluster's luminosity and its richness are both proxies for its mass, we can expect that we will observe the same trend of migrating red sequences for a sample of galaxies in clusters (in this thesis, we use galaxies included in the Sloan Digital Sky Survey's 8th data release; see Section 2.1 for details) when they are grouped into cluster richness bins[3]. Indeed, when we do so with the data used in this thesis (see Chapter 2 for details), we observe that this is the case, as shown in Figure 1.5. The red sequence also displays a marginal evolution with redshift.

The lower shaded regions in each panel of Figure 1.4 are called the blue cloud. This population represents the galaxies which are still forming stars, and converse to the red sequence, it is more numerically significant in field environments than in denser regions such as clusters.

1.4 Defining quenching

"Quenching" is the term commonly used to describe the suppression and eventual cessation of star formation in galaxies when they enter a dense environment such as a galaxy group or galaxy cluster. Quenching is caused by the removal of a galaxy's cold gas reservoir, essentially leaving it with no material with which to form new stars. When star formation stops, passive stellar evolution proceeds, and the galaxy becomes redder in color.

Star-forming galaxies appear bright and blue because of the young stars they contain. See the Hertzsprung-Russell diagram in Figure 1.6 for a visual aid depicting the types of stars that form in new galaxies. The bright, blue stars in the upper left of the diagram experience a significantly shorter main sequence lifetime than their dimmer, redder counterparts in the lower right.

[3]Cluster richness is a measurement of the number of galaxies a cluster contains and is described in detail in Section 2.3.

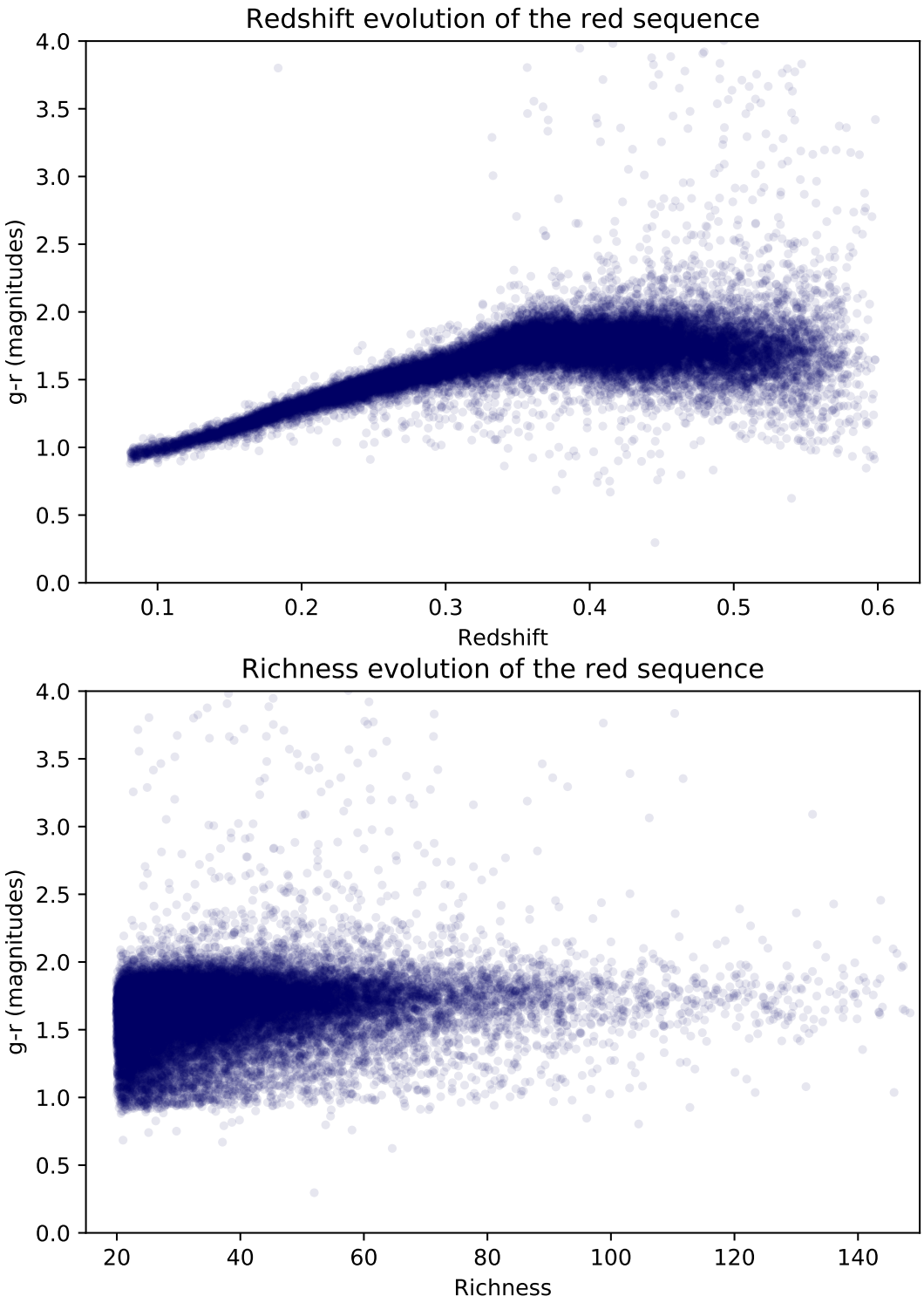

Figure 1.5: Top panel: evolution of the red sequence $g - r$ color with respect to redshift. Bottom panel: evolution of the red sequence $g - r$ color with respect to cluster richness λ in our central redshift bin. Datapoints represent clusters' brightest central galaxies.

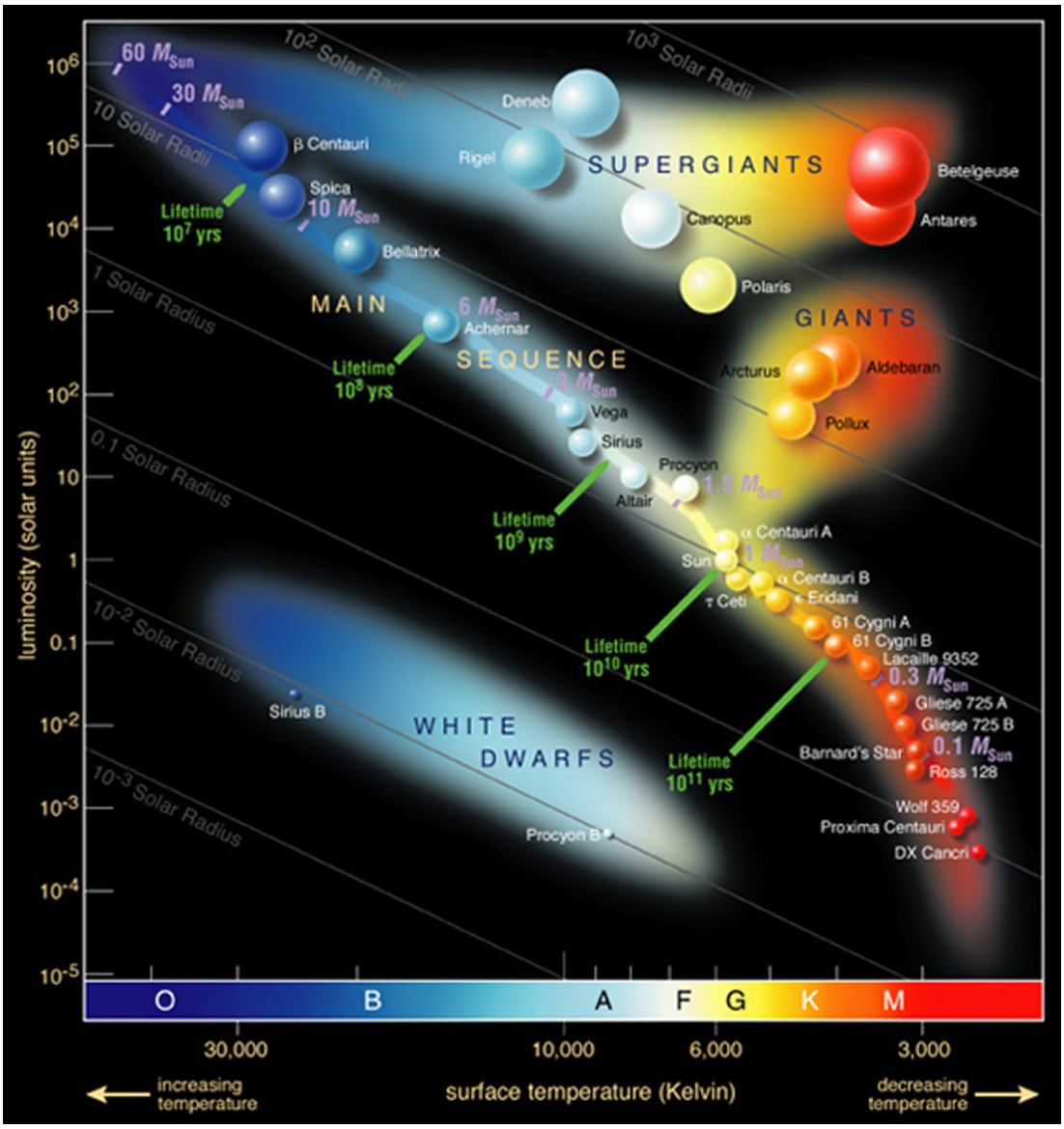

Figure 1.6: Hertzsprung-Russell diagram. The main sequence of stars runs from the upper left to the lower right of the diagram. The faint diagonal lines are lines of constant radius, and stellar types are listed within the color bar. We observe that blue stars are massive and hot, while red stars are smaller and dimmer. A young galaxy will appear blue because of the blue stars it contains; however, when then blue stars turn off the main sequence and die, the galaxy will become increasingly red in color (image credit: ESO[4]).

As a galaxy ages, its stars begin to turn off of the main sequence with the most massive stars evolving first. As a star's mass is correlated with its color, the first stars in a galaxy to turn off the main sequence are the bluest ones, and assuming no new stars are formed (as in the case of quenching), the overall color of the galaxy becomes redder. This causes the galaxy to move upward on the simplified CMD in Figure 1.7. Post-quenching, the galaxy will appear redder, possess a diminished gas and dust content, and have a lower star formation rate (SFR) (Jian et al., 2017). Most galaxies are quenched within one pass of the cluster's center, or about 1.5 Gyr after entering the cluster (Jung et al., 2018).

While it is universally accepted that quenching does occur, the details concerning how and why it occurs are debated. A fundamental question in the study of galaxy clusters is which physical process or processes cause quenching to occur? Additionally, if it is a combination of processes, which is dominant under various circumstances? In the following section, we will explore several mechanisms which could be responsible for quenching.

1.5 Proposed quenching mechanisms

There are two classes of quenching mechanisms: internal and external. Internal quenching mechanisms are primarily tied to a galaxy's mass. On the other hand, external causes of quenching relate to a galaxy's environment, which we can effectively classify as being within the field, a group, or a cluster, while internal quenching is correlated with a galaxy's mass. To gain insight regarding the relative significance of each quenching mechanism as a function of internal factors such as galaxy mass and external factors such as redshift and environment type, many galaxies should be observed and searched for tell-tale signs of individual quenching mechanisms so that statistical claims can be made. Each type of possible quenching mechanism will be described below.

1.5.1 Internal quenching mechanisms

Internal quenching mechanisms are mostly dependent on a galaxy's mass, being significantly more efficient for more massive galaxies. Possible mechanisms include stellar winds, winds from supernovae, and active galactic nuclei (AGN) feedback.

Stellar winds (sometimes referred to in the literature as starburst winds) are driven by the mechanical energy and momentum associated with star formation. Stellar

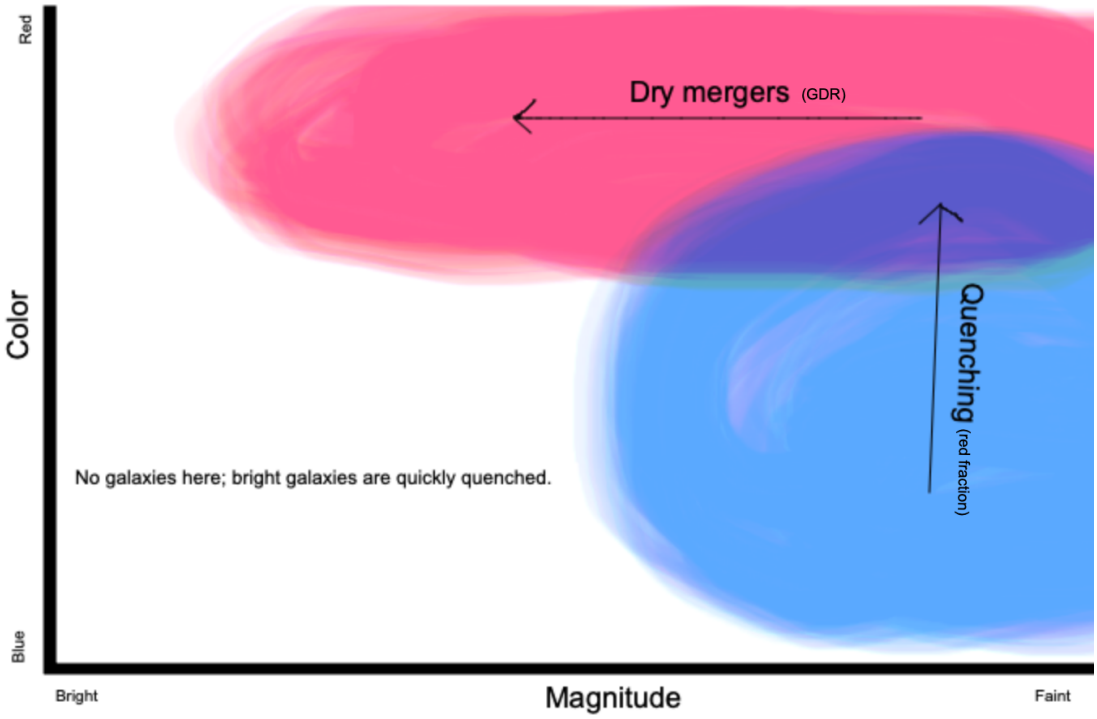

Figure 1.7: Illustration of the processes which move galaxies around the color-magnitude diagram. The red sequence galaxies are represented in red, while the blue cloud galaxies are represented in blue. When a galaxy falls into a cluster, it interacts with the cluster's ICM and gravitational potential well and its cold gas reservoir is stripped away in a process called quenching. As passive stellar evolution proceeds within the galaxy, it becomes redder in color and moves upward on the CMD. By measuring the red fraction of a cluster, we gain insight about the progress of quenching in its galaxies (see Section 3.9). Inside a galaxy cluster, quenched galaxies interact through dry (gas-less) mergers to form increasingly massive galaxies. The more massive a galaxy, the brighter it will be, causing it to move leftward along the red sequence in the CMD. This process can be tracked by measuring a galaxy cluster's GDR (see Section 3.11).

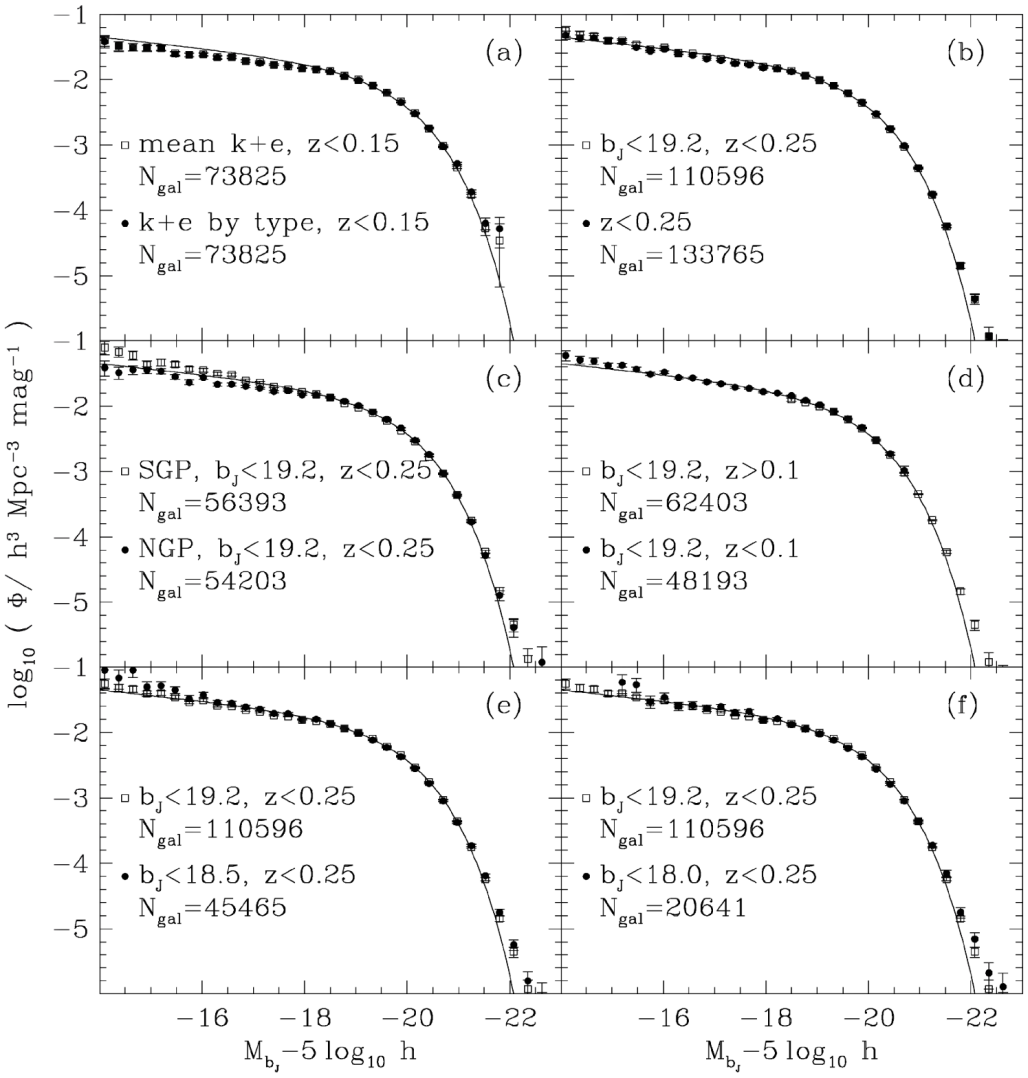

Figure 1.8: Luminosity functions for different sub-populations of galaxies from the2dF galaxy redshift survey (2dFGRS) (Norberg et al., 2002). The y-axes are a measure of the number of galaxies while the x-axes represent luminosity. The sub-populations are separated by redshift and apparent b_j magnitude. The smooth curves are Schechter functions fitted to the data. Note how for all bins, the luminosity function is nearly the same. Figure from Norberg et al. (2002).

winds are significant for only young ($\lessapprox 10^7$ yr) starbursts that form many high-mass ($60M_\odot$) stars in a metal-rich ($Z > Z_\odot$) environment. Under any other circumstance, winds from supernovae play a more significant role in the energetics of a galaxy (Veilleux et al., 2005).

AGN also play a role; as the supermassive black hole in the center of a galaxy accretes material, there are many processes by which the energy released can drive galactic winds which remove gas from the galaxy and results in quenching. Radiative processes in particular can achieve this in a variety of ways: radiation can create a force on surrounding gas by electron scattering, scattering and absorption with dust grains, photoionization, or scattering in atomic resonance lines (Veilleux et al., 2005).

Galaxies become more susceptible to internal quenching mechanisms as they increase in mass. Jian et al. (2017) analyzed a catalog of 1600 Pan-STARRS1 groups and found that for all galaxies, the median star formation rate (SFR) decreases when approaching an over-dense region from the field. This effect is more pronounced for less massive galaxies than more massive ones, for galaxies at lower redshift than those at higher redshift, and for galaxies in clusters rather than those in groups. They suggest that, although environmental quenching efficiency ϵ was found to be higher for more massive galaxies, these galaxies' increased mass causes them to be more susceptible to mass-dependent, non-environmental quenching mechanisms and are more likely to already be dead or dying for redshifts less than $z \approx 0.8$ (Tanaka et al., 2005). This is why no galaxies are present in the lower left corner of the CMD in Figure 1.7; bright, blue galaxies are quickly quenched, and so by the low redshift range we consider in this thesis, none of these massive galaxies are left in the blue cloud. The question remains, though, which quenching mechanisms are most significant for galaxies of lower mass as a function of environment.

1.5.2 Environmental quenching mechanisms: gravitational interactions

We can classify environmental quenching mechanisms into two subgroups, the first of which is based upon gravitational interactions, either with other galaxies or with the overall potential representing the group or cluster.

When galaxies interact with each other, one possibility is that of a galaxy-galaxy merger. Mergers act on a relatively short timescale of less than 1 Gyr (Boselli et al., 2016). Denser environments such as clusters or groups correlate with an increased merger rate as compared to the field (Dressler et al., 1994; Makino & Hut, 1997;

van Dokkum et al., 1999); however, the relative significance of mergers for quenching peaks in group environments, because clusters tend to exhibit velocity dispersions too high for mergers to be an efficient source of quenching (Boselli et al., 2016). This tendency for some galaxies to be quenched in lower density environments before entering clusters is refereed to in the literature as "preprocessing".

The result of a merger depends on the mass ratio of the galaxies involved. If their masses are significantly different, the smaller galaxy will experience a burst of star formation, while the larger one may or may not experience the same (Cox et al., 2007). Mass ratios close to unity create a stronger effect; the galaxies experience complete tidal disruption and form a single bulge-dominated system with a strong but short-lived central burst of star formation (Di Matteo et al., 2007). The star burst rapidly gives way to an exhaustion of the cold gas supply, and quenching ensues.

Another possibility when galaxies interact with each other is referred to in the literature as harassment or threshing, a process which preferentially occurs outside the groups or clusters virial radius, before the galaxy is accreted (Boselli et al., 2016). Through harassment, several smaller galaxies make passes by the galaxy in question, not merging but pulling small amounts of matter - particularly star-forming cold gas - to regions of lower gravitational potential and sometimes liberating them from the larger galaxy altogether (Moore et al., 1995).

Galaxies can interact not only with each other, but also with the gravitational potential wells present in overdense regions of the universe such as clusters. As a galaxy approaches such a region, the galaxy will experience tidal stripping which pulls some of its material out to areas of lower potential. This improves the efficiency with which other quenching mechanisms can remove material from the galaxy.

1.5.3 Environmental quenching mechanisms: interactions with the intracluster medium

The second subgroup of environment quenching mechanisms involves galaxies interacting with the hot, dense ICM once inside an overdense environment. When a galaxy falls into a group or cluster, the gas component of a galaxy experiences a ram pressure force resulting from its motion through the gaseous ICM. This effective energy input into the galaxy's gas either unbinds it, in the case of stripping, or raises it to greater galacto-centric radius (associated with a lower binding energy) where internal effects (such as winds from star formation, super novae, or AGN) may ultimately

strip it, leaving no material with which to form new stars (Gunn & Gott, 1972; Abadi et al., 1999; Kawata & Mulchaey, 2008). This process is referred to as ram pressure stripping.

Ram pressure stripping can be identified from the telltale stream of gas and dust trailing behind the galaxys stellar contents as it is accreted by the cluster. Poggianti et al. (2016) conducted a survey to identify galaxies of this type, which they dub "jellyfish galaxies" and discovered 344 candidate jellyfish galaxies distributed among 71 galaxy clusters in the redshift range from $z = 0.04$ to $z = 0.07$. For a color-composite image of one of the jellyfish galaxies they found, see Figure 1.9.

For a few more concrete examples of ram-pressure stripping in progress, Chung et al. (2007) and Boselli et al. (2016) present clear observations of ongoing ram pressure stripping in galaxies within the Virgo cluster; they detect tails of diffuse, ionized gas extending from the galaxies, trailing behind their stellar contents, identifying these galaxies as jellyfish galaxies.

1.6 Approaches to studying galaxy clusters

Having established that galaxy clusters are of scientific interest, what methods can we use to study them? There are two mutually-exclusive approaches one can take:

- The first option is to look at a few high redshift clusters in hopes of observing them during their formation at a large look-back time, when interesting effects such as quenching and mergers may be observed in progress. The Spitzer Adaptation of the Red-sequence Cluster Survey (SpARCS) cluster survey is an example of this type of effort. SpARCS observes galaxy clusters at redshifts greater than $z = 1$ in the optical and infrared bands over a total area of 41.9 square degrees (Muzzin et al., 2009; Wilson et al., 2009).

- The other option for studying galaxy clusters is to obtain a large sample of many low redshift galaxies, stack them into bins, and make statistical statements. Although we cannot usually see phenomena such as quenching or mergers in progress at this redshift, we can see their results in the distribution of member galaxies as a function of observables such as colour, morphology, and emission line indices. With the advent of large surveys such as the Sloan Digital Sky Survey (SDSS) described in Section 2.1, the Dark Energy Survey (DES) (Collaboration, 2005), and the upcoming Large Synoptic Survey Telescope (LSST)

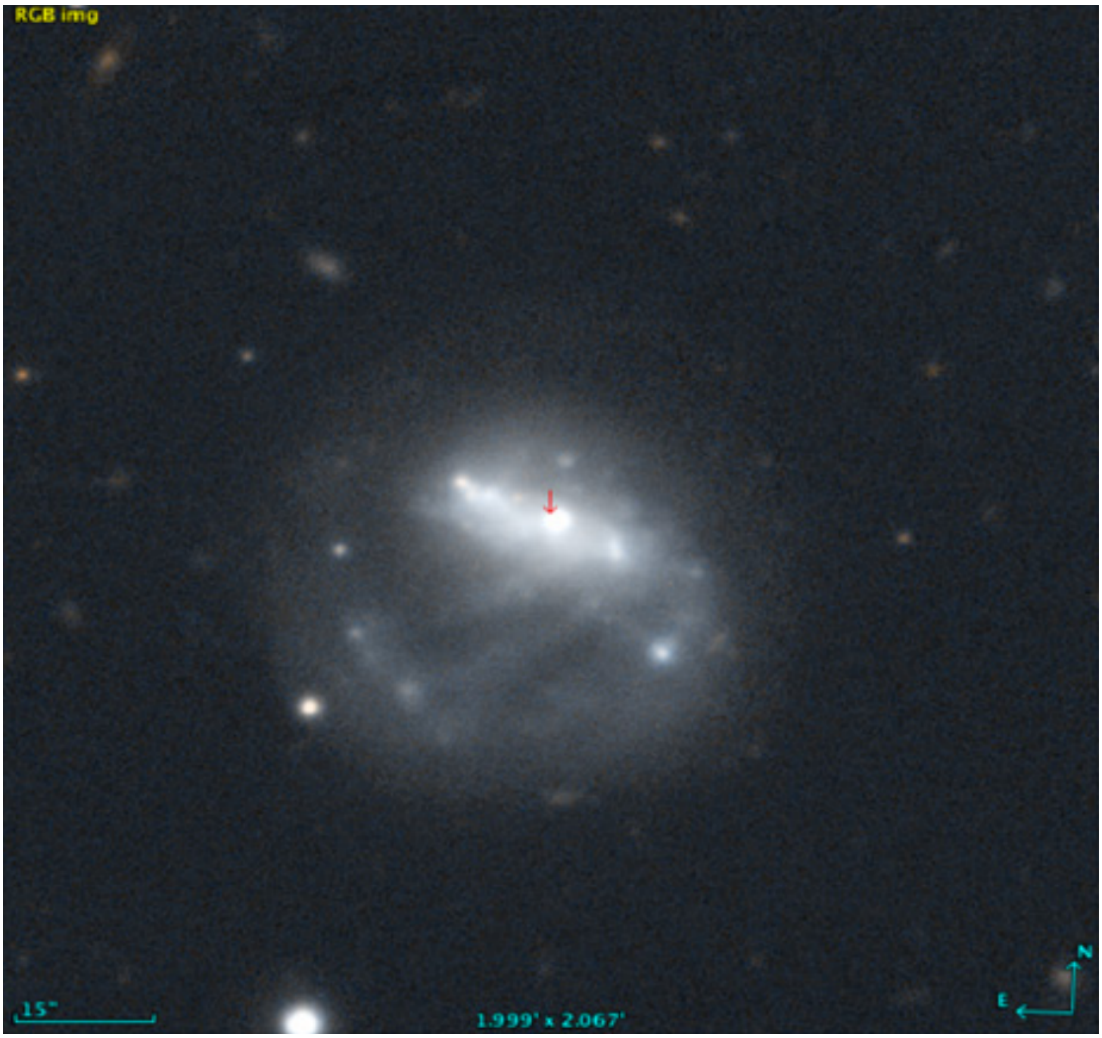

Figure 1.9: Color-composite image of ram-pressure stripping in progress within a galaxy. Galaxies such as this one which display tentacle-like tails of diffuse, ionized gas trailing behind their stellar contents are sometimes referred to as "jellyfish galaxies". Figure from Poggianti et al. (2016).

(Collaboration, 2012) among others, this is becoming an increasingly attractive approach. Indeed, it is the approach taken in this thesis, and has also been used by various authors including but not limited to De Lucia et al. (2007) and Bildfell et al. (2012).

The primary benefit of this approach is the ability to stack galaxies in bins and do statistical background subtraction in order to obtain a statistically pure sample of cluster galaxies, as described in Section 3.5.

1.7 Methods of detecting galaxy clusters

Both of the methods listed above for studying galaxy clusters depend on first detecting said clusters. There are a few options for doing so which will be listed below.

1.7.1 Optical cluster detection via red sequence identification

One option for detecting clusters is to observe large regions of the sky and then take advantage of the known colour-magnitude relation of cluster galaxies described in Section 1.3. This is what redMaPPer does. Details of its algorithm will be discussed in Section 2.2.

In general, though, this type of cluster detection works by first searching for areas of galaxy overdensity along the line-of-sight, and then using the red sequence and redshift measurements (when available) to identify which galaxies within that overdensity are likely to be cluster members.

When comparing the different methods of detecting clusters, it can be helpful to consider what signal is being measured for each method. For optical cluster detection with the red sequence, the signal is number of galaxies per unit area satisfying an evolving brightness and colour threshold; it is a number density. Beside redMaPPer, a few examples of this type of cluster finder are *K2* (Thanjavur et al., 2009), the Northern Sky Optical Cluster Survey (Gal et al., 2000), the Palomar Distant Clusters Survey (Postman et al., 1996), and the Red-Sequence Cluster Survey (Gladders et al., 2007).

1.7.2 X-ray cluster detection

Bremsstrahlung is German for "breaking radiation", and it is the radiation that results from the deceleration of a charged particle when it is deflected electromagnetically by

another charged particle. The kinetic energy lost by the particle when it decelerates is emitted as a photon, and the law of conservation of energy is satisfied. In galaxy clusters, the ICM emits bremsstrahlung radiation in the X-ray energy band as its thermally-excited electrons are decelerated in the Coulomb fields of protons. For an example of what such emission looks like within a galaxy cluster, see the left panel of Figure 1.3.

The signal of interest for X-ray cluster detection is the projection of the square of the free electron density in the ICM, and it displays a weak dependence upon the ICM temperature (Willis et al., 2018). Some efforts to find galaxy clusters by detecting this X-ray bremsstrahlung radiation include the Einstein Observatory Extended Medium Sensitivity Survey (EMSS; Gioia & Luppino, 1994), the ROSAT-ESO Flux-limited X-Ray Survey (Bohringer et al., 2002, REFLEX;), and the XMM Survey (Mehrtens et al., 2012).

1.7.3 Cluster detection with the Sunyaev-Zel'dovich effect

The Sunyaev-Zel'dovich effect creates deficits in the brightness of the CMB when its photons interact with a galaxy cluster's hot ICM via inverse Compton scattering [5]. Therefore by observing the CMB in the millimeter wavelength scale, we can locate clusters. The signal measured in this case is the apparent decrement in the brightness of the CMB (Sunyaev & Zeldovich, 1970, 1972). There have been several efforts to measure the CMB, such as COBE (Fisenko & Lemberg, 2018; Odegard et al., 2019), Planck (Planck Collaboration et al., 2018), and WMAP (Bennett et al., 2012).

Once the observations of the CMB have been made, it is possible to comb through and identify galaxy clusters. Some such efforts include work by Vanderlinde et al. (2010), Staniszewski et al. (2008), Marriage et al. (2010), and Reichardt et al. (2012), among others. The right panel of Figure 1.3 shows the galaxy cluster SPT-CL J2106-5844, which is the most massive known cluster of redshift greater than 1 (its redshift is $z = 1.133$) discovered as a result of the Sunyaev-Zel'dovich effect.

1.7.4 Cluster detection with weak lensing

Extremely massive objects (such as galaxy clusters, and particularly their dark matter components) distort spacetime in such a way that light curves around them, effectively

[5]Inverse Compton scattering occurs when an electron of high kinetic energy interacts with a photon of a lower energy. When the electron and photon interact, the photon absorbs some of the electron's energy and has a higher frequency than it had before scattering

acting as lenses. This process is known as gravitational lensing, and it can manifest in two different ways: as strong lensing or as weak lensing.

Strong lensing is the most extreme form of gravitational lensing, wherein the cluster acting as a lens is massive enough and close enough to a background galaxy that the light from the background galaxy takes multiple paths around the cluster and multiple images of the background galaxy are visible. In the less extreme and more common case in which the galaxy cluster is less massive or farther away from the background galaxy, weak lensing occurs. In this regime, the image of the background galaxy will not be repeated, but it will be distorted and appear stretched along an arc centered on the galaxy cluster's center of mass. An excellent example of weak lensing is shown in the left panel of Figure 1.3.

The signal used for cluster searches via weak lensing observations is the integrated shear signal injected into the shapes of background galaxies due to the effects of the cluster's mass on spacetime (Kaiser et al., 1995). A few examples of efforts to do so include work by Stern et al. (2018), Gavazzi & Soucail (2006), Wittman et al. (2005), and Miyazaki et al. (2002).

1.8 Diagnostic observables of the cluster member galaxy populations

Given our question of how local and global environments affect galaxy evolution within clusters, what observable properties can we use to gain insight? In this thesis, we consider red fraction and giant-to-dwarf ratio, described in the following subsections.

1.8.1 Red fraction

Put simply, the red fraction of a cluster is the fraction of its member galaxies which lie along the red sequence above a given brightness threshold. If n_{red} is the number of galaxies in a given cluster which lie along its red sequence, and n_{total} is the total number of galaxies within the cluster, then its red fraction f_r is given by:

$$f_r = n_{red}/n_{total}. \tag{1.2}$$

By observing how a sample of clusters' red fraction changes with redshift, we can learn about the rate at which galaxies within them are quenched with respect to

time. In other words, red fraction controls the vector moving from blue to red on the cartoon CMD shown in Figure 1.7. Understanding the behavior of clusters' red fractions allows us to discriminate between potential quenching mechanisms due to the fact that each tends to act on its own characteristic timescale.

Note that some other authors (De Lucia et al., 2007; Urquhart et al., 2010; Butcher & Oemler, 1978, 1984) use blue fraction rather than red fraction, but this is simply defined as $1-f_r$, and so represents the same information. The details of our calculation of red fraction are given in Section 3.8.

1.8.2 Giant-to-dwarf ratio

The giant-to-dwarf ratio of a cluster is the ratio of number of giant galaxies to number of dwarf galaxies within the red sequence of the cluster, where the distinction between giant and dwarf galaxies is some characteristic luminosity. This luminosity is in principle arbitrary, and different values are used by different authors. Within a given brightness range, the giant galaxies are defined as being brighter than this luminosity, and the dwarf galaxies are defined as being fainter. If n_{giants} is the number of giant galaxies within a cluster's red sequence and n_{dwarfs} is the number of dwarf galaxies along its red sequence, then the cluster's giant-to-dwarf ratio GDR is given by:

$$GDR = n_{giants}/n_{dwarfs}. \tag{1.3}$$

The GDR of a galaxy cluster represents a compression of its luminosity function's information; it tells us the slope of the Schechter function, a typical example of which is shown in Figure 1.8. As such, some authors such as De Lucia et al. (2007) and Capozzi et al. (2010) refer to the GDR as the luminous-to-faint ratio.

Observing the change in a typical cluster's GDR with respect to redshift is interesting because it informs us about how a cluster's red sequence builds up over time. Does it start with giant galaxies and then accrete dwarfs? Or does it start with dwarfs that merge hierarchically to become giants? Perhaps is it a more or less even mix of giant and dwarf galaxies all along? Observing the change in GDR with respect to redshift (a proxy for time) tells us when in the universe's history different types of galaxies are quenched, and this in turn could help us discriminate between potential quenching mechanisms. The details of our calculation of GDR are given in Section 3.10.

1.9 Thesis overview

Chapter 1 provides an introduction to the problem and a review of previous work, followed by an overview of the structure of the document itself.

Chapter 2 provides an overview of the data used in this thesis.

Chapter 3 discusses the methods used for measuring red fraction and giant-to-dwarf ratio as a function of cluster redshift and richness. This represents the effects of global environment. It then lists the results and gives a discussion of their implications.

Chapter 4 discusses the methods used for measuring red fraction and giant-to-dwarf ratio as a function of cluster redshift and d_{BCG}, representative of local environment. It then lists the results and gives a discussion of their implications.

Chapter 5 summarizes our conclusions and provides suggestions for future work on the topic.

Chapter 2

Data

Data used for this thesis came from two sources. The first, redMaPPer, is a catalog of galaxy clusters, and the second, the Sloan Digital Sky Survey, was used to gather photometric information about galaxies within the redMaPPer clusters. redMaPPer is an algorithm which locates galaxy clusters in photometric surveys using the red sequence detection method outlined in Section 1.3, and it is fully described in its introductory paper by Rykoff et al. (2014).

The details of the redMaPPer algorithm will be discussed below; for now, the important things to note are that when the redMaPPer algorithm is applied to the SDSS DR8 dataset, a catalog of 26111 galaxy clusters results. The redshift of these clusters runs from $z = 0.08$ to $z = 0.55$; however, we selected a central subset of these clusters with redshifts in the range from $z = 0.2$ to $z = 0.5$ to avoid issues associated with the low- and high- z tails of the distribution. See Figure 2.1 for our selected clusters' redshift distribution.

2.1 Sloan Digital Sky Survey

The redMaPPer algorithm uses the Sloan Digital Sky Survey (SDSS)'s 8th data release to locate galaxy clusters. SDSS is large survey designed to photometrically image 10^4 square degrees of the sky and obtain spectra for 10^6 objects (York et al., 2000). Its eighth data release, the primary data source used in this thesis, is fully described in its introductory paper by Eisenstein et al. (2011). We chose to use SDSS DR8 in our own analysis for two reasons. The first is for homogeneity with respect to redMaPPer , which also uses SDSS DR8 in its task of locating galaxy clusters. The second reason is because DR8 is the most recent data release with which SDSS has included photometry rather than just spectroscopy.

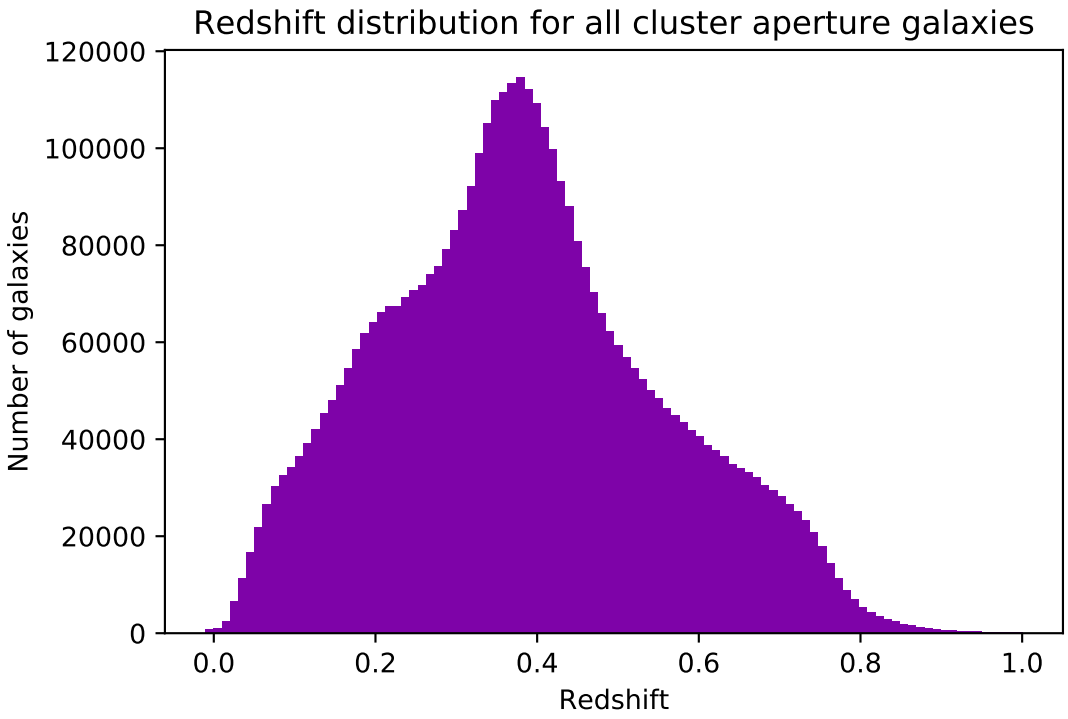

Figure 2.1: Redshift distribution of redMaPPer clusters in blue with bin edges overlaid in black. Each bin contains an approximately equal number of clusters.

SDSS makes use of a dedicated 2.5-m, f/5 focal ratio, modified Ritchey-Chretien wide-field altitude-azimuth-mounted telescope based at the Apache Point Observatory. It uses a large mosaic-style CCD camera which sits at the telescope's Cassegrain focus for photometry with five bandpass filters: u, g, r, i, and z with effective wavelengths of 355, 467, 616, 747 and 892 nm respectively. Magnitudes are measured in the AB_{95} system. The imaging CCD has a 13.52 arcminute field-of-view. SDSS photometry is calibrated using a table of standard stars published by the U.S. Naval Observatory (USNO) from their 1-m telescope (York et al., 2000). SDSS also has two digital spectrographs available. For this work, though, we only make use of the g-band and r-band photometry, so the emphasis in this thesis will be on SDSS's photometric capabilities.

Astronomical objects can be observed with the imaging CCD up to a limiting bright magnitude of approximately 14 apparent magnitudes, at which point the object becomes too bright and causes saturation (Djorgovski et al., 2012). For details on the faint magnitude limits of the SDSS survey, see Section 3.4. We use the SDSS main galaxy sample to select our data for galaxies in clusters and in the field.

2.2 The redMapper cluster-finding algorithm

redMaPPer uses a 3-part algorithm. In the first pass, it identifies a list of galaxies which could be the BCGs of clusters and evaluates the way in which the red sequence evolves with redshift. In the second part, it uses this red sequence-redshift relation to assign each galaxy a likelihood of being a cluster member. Finally, in the third stage, the final selection of galaxies within each cluster are proabapilistically determined in a process the authors refer to as "percolation".

For a flowchart detailing this iterative process, see Figure 2.2, from Rykoff et al. (2014). The three stages will be described below in greater detail.

2.2.1 Stage 1: first pass

The first stage in the redMaPPer algorithm is the calibration of the red sequence versus redshift relation in order to select a sample of BCGs which represent the centers of clusters. This process is performed iteratively; a sample of BCGs is selected, the sample of BCGs is used to refine the red sequence-redshift relationship, this relationship is used to refine the selection of BCGs, and so on. For the first iteration, redMaPPer relies on a sample of spectroscopically-observed seed galaxies (specifically,

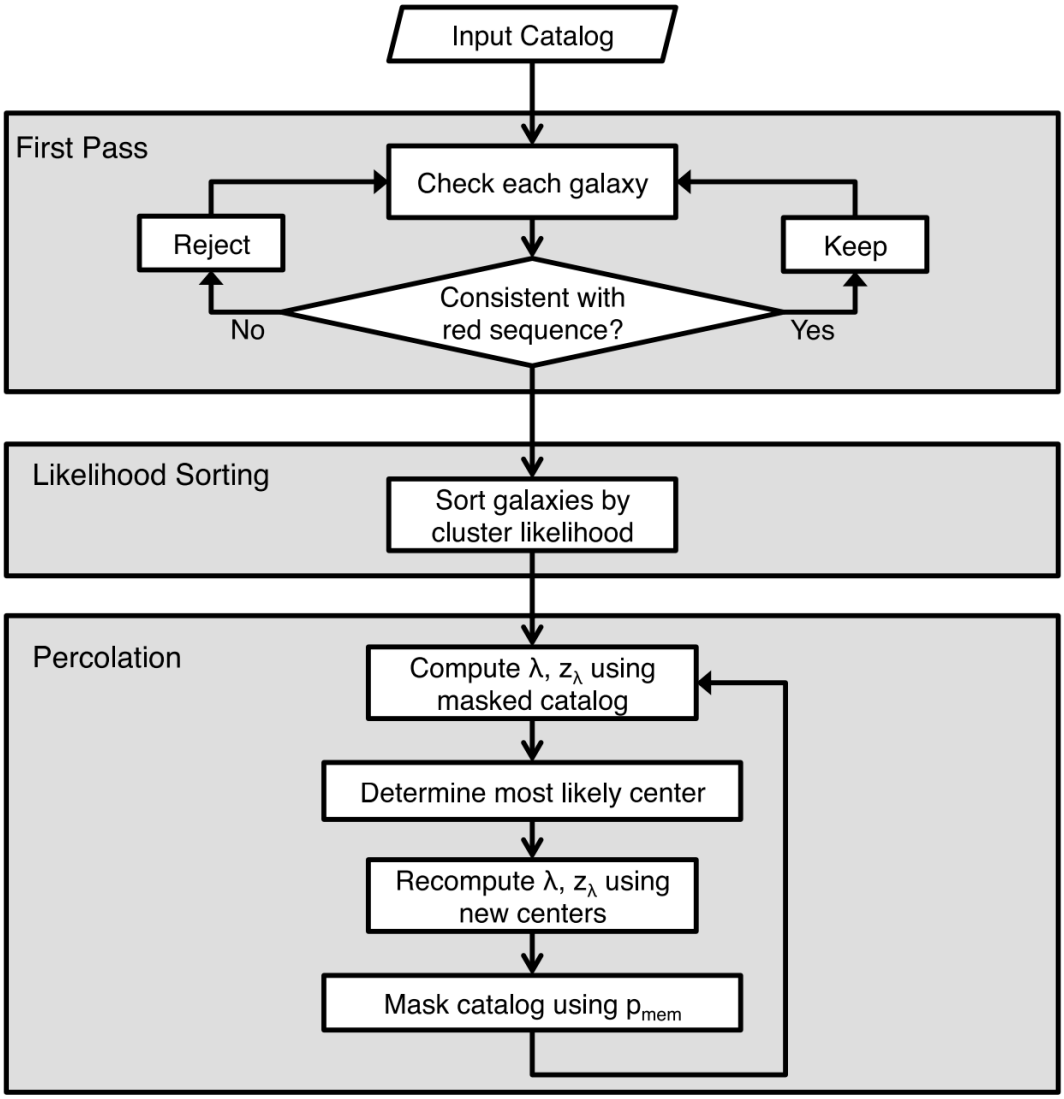

Figure 2.2: Flowchart of the redMaPPer cluster-finding algorithm, from Rykoff et al. (2014).

they use a sample of galaxies with spectroscopic observations from the SDSS DR8 dataset) to perform this calibration. The redMaPPer authors take several steps to ensure that these seed galaxies are composed fully of red galaxies within clusters. The steps for selecting the initial seed galaxies will be summarized below, following the outline by Rykoff et al. (2014):

- Identify from the full SDSS DR8 galaxy dataset those galaxies which have been spectroscopically observed.

- Choose which of these galaxies are red based on a color cut in $g-r$ for galaxies with redshift $z < 0.35$ and in $r-i$ for galaxies with redshift $z > 0.35$. These colors were chosen because they span the 4000 Ångstrom break in their respective redshift bins. To determine the exact value for the cutoff color between red and not-red, the full sample of spectroscopic galaxies was binned into redshift bins of width ± .025. The mean and intrinsic width $\sigma_{int}(z)$ are then calculated for the distribution of galaxies within each redshift bin. These values are calculated using the error-corrected Gaussian Mixture Method (Hao et al., 2009). Galaxies within $2\sigma_{int}(z)$ of the mean for red galaxies in their respective redshift bins are selected as red.

- Use this initial rough selection of red galaxies to compute their mean color with respect to redshift. The mean color-redshift relation is refined by minimizing the function $s = \sum_i |c_i - \tilde{c}(z_i)|$. $\tilde{c}(z)$ is the model for the color as a function of redshift, and it is defined via spline interpolation. The values for the spline nodes are the parameters with respect to which s is minimized. These spline nodes are distributed on a redshift grid with a spacing of 0.1.

- Determine the width of the colour-redshift relation using the mean colour-redshift relation obtained in the previous step. This is achieved with another minimization, this time of the function $s = \sum_i ||c_i - \tilde{c}(z_i)| - \text{MAD}|$, where MAD is the median absolute deviation of the sample about the median. For a Gaussian distribution, $\sigma_{int}(z) = 1.4826 \times \text{MAD}$. Like $\tilde{c}(z)$, MAD is defined with a spline interpolation where the free parameters are the values of the function at the nodes.

- Finally, it is time to select a final sample of seed galaxies. The previous steps have created a full model for the spectroscopic red galaxies, so now all galaxies

within $2\tilde{\sigma}_{int}(z)$ of the mean model color at the spectroscopic redshift of the galaxy itself are chosen as seed galaxies. As mentioned above, the colors used for this selection are $g-r$ at $z<0.35$ and $r-i$ at $z>0.35$.

At this point, the process is repeated, starting from the set of seed galaxies rather than the full set of spectroscopically-observed galaxies. The process is iterated several time until an acceptable list of cluster member galaxies is generated.

2.2.2 Stage 2: likelihood sorting

Now that the sample of BCGs has been defined, redMaPPer selects likely cluster member galaxies surrounding each of the seed galaxies. This is completed via the following steps:

- Begin with a galaxy of known spectroscopic redshift from the list generated in the first pass.
- Select galaxies which cluster around this galaxy in both projected physical space and in colour. For physical space, selected galaxies must be within 500 h^{-1} kpc of the seed galaxy. In colour space, the selected galaxies must be within 2σ of the model colour determined previously. The width σ of the colour box is set to 0.05 and 0.03 for $z<0.35$ and $z>0.35$ respectively in order to match the approximate width of the red sequence.
- Fit a linear model to the red sequence of these selected galaxies.
- Determine the value of the richness estimator λ (defined by Equation 2.5) for this group of galaxies with a fixed radius of $500h^{-1}$ kpc. Further details regarding the calculating of λ with be given in Section 2.3. This group of galaxies now represent a cluster.
- If $\lambda>10$, assign all galaxies in this cluster with $p_{mem}>0.7$ (p_{mem} is the probability of a galaxy being a cluster members, and it is defined by Equation 2.4) a redshift equal to that of the initial seed galaxy.

At this point, the redMaPPer algorithm has generated a set of red galaxies over the redshift range of interest; these galaxies may or may not be true cluster members, but there is an initial estimate for p_{mem}, the likelihood of each galaxy being a cluster

member. Additionally, for each potential cluster itself, redMaPPer computes a likelihood which is a combination of the richness likelihood and the centering likelihood. The richness likelihood $\mathcal{L}_\lambda$ is defined by

$$\ln \mathcal{L}_\lambda = -\frac{\lambda}{S} - \sum \ln(1 - p_{mem}), \tag{2.1}$$

where S is a scale value given by $S = 1/(1 - C)$, and C is the fraction of galaxies that should be masked out of the cluster to ensure photometric completeness at all redshifts (the calculation of C is beyond the scope of this thesis; for details, see Rykoff et al. (2014)). The centering likelihood $\mathcal{L}_{cen}$, meanwhile, is the likelihood of the chosen BCG being the true center of the cluster, and it is given by

$$\ln \mathcal{L}_{cen} = \ln[\phi_{cen}(m_i|z_\lambda, \lambda) G_{cen}(z_{red}) f_{cen}(w|z_\lambda, \lambda)]. \tag{2.2}$$

Here, $\phi_{cen}(m_i|z_\lambda, \lambda)$ is a luminosity filter for the cluster. $G_{cen}(z_{red})$ is a photometric redshift filter, and $f_{cen}(w|z_\lambda, \lambda)$ is a local density filter. For details on how each of these quantities is calculated, refer to Rykoff et al. (2014).

Finally, redMaPPer combines the two likelihoods to obtain the total likelihood used to rank the clusters from most likely to least likely. This total likelihood $\mathcal{L}$ is given by

$$\ln \mathcal{L} = \ln \mathcal{L}_\lambda + \ln \mathcal{L}_{cen}. \tag{2.3}$$

2.2.3 Stage 3: percolation

The percolation process involves probabilistically masking potential cluster member galaxies in order to generate the final catalog of clusters and their member galaxies. This is necessary to assign each galaxy to a cluster and to ensure that each cluster is counted only once. Percolation abides by the following steps:

- Beginning with the most highly-ranked cluster galaxy from the previous step, re-compute the richness λ (described in Section 2.3) and the richness-based redshift z_λ (this is the type of redshift used for the analysis in this thesis, and it is described in Section 2.4) for this galaxy's cluster using the percolated galaxy catalog. For the first iteration of percolation, the percolated galaxy catalog is the input galaxy catalog (SDSS DR8; see Eisenstein et al. (2011) and York et al. (2000)).

- Ascertain which galaxy should be the BCG of this cluster and compute its centering likelihood given by Equation 2.2.
- Calculate λ and z_λ again for this cluster using its newly-chosen central galaxy.
- Determine which galaxies are members of this cluster using their membership probabilities p_{mem}, as given by Equation 2.4. Use the results to update the percolated galaxy catalog.
- To ensure that each cluster is only counted once, remove all possible cluster center galaxies from the list which have a lower total likelihood $\mathcal{L}$ than the current cluster and also have a membership probability $p_{mem} > 0.5$.
- Begin this process again with the next most-highly ranked cluster galaxy in the likelihood list.

This process is repeated until a final catalog of galaxy clusters and their member galaxies is produced.

2.3 Defining the cluster richness estimator λ

The redMaPPer catalog provides a multicolor richness richness for each cluster, which Rykoff et al. (2014) call λ. To calculate λ for a cluster, redMaPPer first considers a vector $\boldsymbol{x}$ which describes all observable properties of a galaxy. They model the projected distribution of galaxies inside the cluster and within its immediate surroundings with $S(\mathbf{x}) = \lambda u(\mathbf{x}|\lambda) + b(\mathbf{x})$. Here, λ is the number of galaxies which are members of the cluster, $u(\mathbf{x}|\lambda)$ is the normalized density profile of the cluster, and $b(\mathbf{x})$ is the density of field galaxies, which are not part of the cluster. The next logical step is to determine which galaxies are actually members of the cluster and which are part of the field. For a given galaxy with observable features $\boldsymbol{x}$, the probability p_{mem} that it is a member of the cluster is given by

$$p_{mem} = p(\mathbf{x}) = \frac{\lambda u(\mathbf{x}|\lambda)}{\lambda u(\mathbf{x}|\lambda) + b(\mathbf{x})}. \tag{2.4}$$

As λ is the total number of galaxies which are true members of the cluster, the following relation must hold:

$$\lambda = \sum p(\mathbf{x}|\lambda) = \sum_{R<R_c(\lambda)} p(\mathbf{x}) = \frac{\lambda u(\mathbf{x}|\lambda)}{\lambda u(\mathbf{x}|\lambda) + b(\mathbf{x})} \tag{2.5}$$

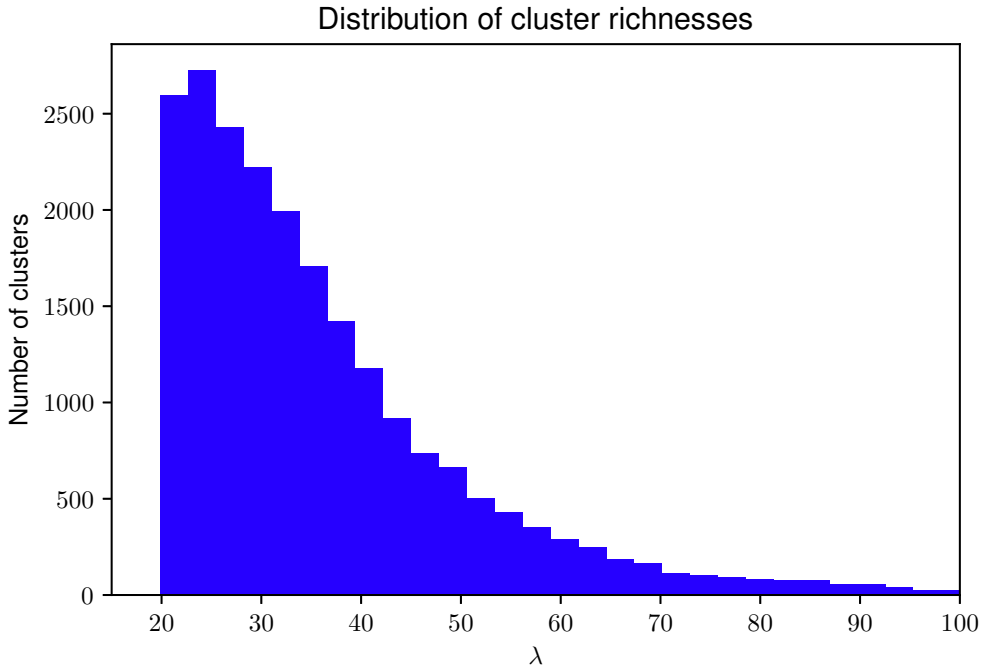

Figure 2.3: Distribution of redMaPPer cluster richnesses λ.

Here, R is radius and R_c is some cutoff radius beyond which no galaxies are considered cluster members. In previous papers (e.g. Rozo et al., 2011; Rykoff et al., 2012), the authors found that the optical radial cut which minimized scatter in the color-magnitude relation scales with richness in the following manner:

$$R_c(\lambda) = R_0(\lambda/100.0)^{\beta}, \tag{2.6}$$

where $R_0 = 1.0h^{-1}$ Mpc and $\beta = 0.2$.

To obtain the richness estimator λ for a given cluster, then, one only needs to use any numerical zero-finding algorithm to solve Equations 2.5 and 2.6 (Rykoff et al., 2014).

The statistical uncertainty for λ is given by

$$\mathrm{Var}(\lambda) = \sum p(\mathbf{x}|\lambda)[1 - p(\mathbf{x}|\lambda)]. \tag{2.7}$$

For the distribution of cluster richnesses in our sample, see Figure 2.3.

2.4 Defining the richness-based cluster redshift z_λ

z_λ is the quantity used for redshift throughout all of the analysis in this thesis. While spectroscopic redshifts are desirable because of their relatively small degree of uncertainty, not all galaxies in the SDSS sample have a spectroscopic redshift available. redMaPPer does, however, include a value of z_λ for every cluster, so we chose to use this measurement instead.

To calculate z_λ for a cluster, redMaPPer begins with its central galaxy and determines its redshift. Like most redMaPPer processes, the calculation of z_λ is iterative. In the first iteration, the central galaxy's redshift is assumed to be equal to z_{red}, an initial estimate for the redshift based on photometry and the model for red sequence galaxies. In successive iterations, z_λ is used as the central galaxy's redshift.

The next step is to calculate the richness λ in the area surrounding the central galaxy, assuming that the cluster's redshift is equal to the central galaxy's redshift (refer to Equation 2.5). Knowing λ allows the calculation of cluster membership probability p_{mem} for each galaxy surrounding the central galaxy (see Equation 2.4).

Now a new redshift for the cluster's central galaxy can be estimated by selecting galaxies with high membership probability and maximizing the following likelihood function:

$$\ln \mathcal{L} = \sum -\frac{w(p_{mem})[\chi^2 + \ln |\mathbf{C}|]}{2}. \tag{2.8}$$

Here, χ^2 represents the distribution of galaxies with a given set of color observations, and $\mathbf{C}$ is the determinant of the covariance matrix for the color observations. w is a weight which varies smoothly from $w = 1$ when $p_{mem} = 1$ to $w = 0$ when $p_{mem} = 0$, and it is given by

$$w(p_{mem}) = \frac{1}{\exp\left[(p_{70} - p_{mem})/0.04\right] + 1}, \tag{2.9}$$

where p_{70} is the probability threshold that accounts for 70% of the total richness in the calculation.

After Equation 2.8 is minimized in order to find a value of z_λ, this redshift is used to recalculate λ and p_{mem} for surrounding galaxies, and the process is repeated until the convergence condition $|z_{\lambda,i+1} - z_{\lambda,i}| < 0.0002$ is met, where i represents each iteration. The distribution of cluster redshifts calculated in this manner is shown in Figure 2.1.

2.5 Selecting cluster aperture galaxies

We selected the Brightest Cluster Galaxy (BCG) from each of the redMaPPer clusters. A BCG is the brightest galaxy in its cluster, accounting for about 5-10% of the cluster's total light (Lin & Mohr, 2004), and they typically lie at the deepest point of a cluster's gravitational well, with a notable exceptions for clusters that are undergoing or have recently undergone a merger (Sanderson et al., 2009). This makes BCGs reliable estimators for the mass-based centroid of a cluster, provided that it is isolated from other clusters.

For each cluster, we selected from SDSS every galaxy within 1 Mpc of its BCG. 1 Mpc was chosen because it is of comparable size to the virial radii of the Coma and Virgo clusters (see Section 1.2). We needed to determine the angular distance which 1 Mpc would cover at a given redshift. For this task, we utilized Astropy's cosmology package (Robitaille et al., 2013; Price-Whelan et al., 2018). We adopted the WMAP9 cosmology (Bennett et al., 2012) and determined the angular distance equivalent to 1 Mpc at the central redshift value in each of our bins; see Figure 2.4 for the evolution of this radius with redshift.

For each cluster, then, the appropriate angular radius was used when searching for galaxies around its BCG. These galaxies are referred to in this thesis as "cluster aperture galaxies", and are not to be confused with "cluster member galaxies", which are the cluster aperture galaxies remaining after performing the statistical background subtraction described in Section 3.5.

For each of these selected galaxies, we downloaded the g-band and r-band apparent model magnitudes. We chose to use these magnitudes to be consistent with redMaPPer. We chose these two bands because they showed the most apparent color bimodality. This makes sense, as at the median redshift ($z = 0.37$) of our cluster sample, the 4000 Ångstrom break falls between the g-band and r-band as seen in the model spectrum in Figure 3.4, and so this combination of filters should give us more information than any other combinations.

All data was downloaded using the SDSS DR8 SkyServer SQL Search system [1], making use of the provided `GetNearbyObjEq` function to select all galaxies within the desired angular radius from a cluster's BCG.

[1] http://skyserver.sdss.org/dr8/en/tools/search/sql.asp

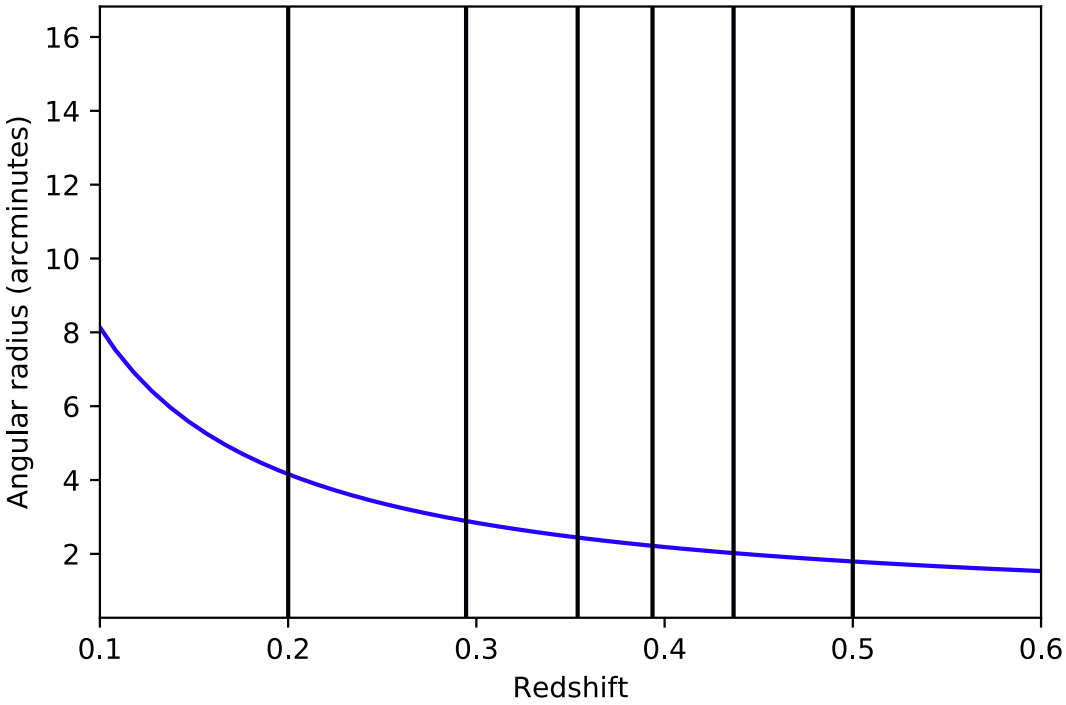

Figure 2.4: Angular radius corresponding to 1 Mpc as a function of redshift, used to select galaxies within 1 Mpc of cluster centers. The redshift bin edges are shown as black vertical lines to highlight the variation of the angular radius within each bin. For each redshift bin, the value for angular radius at the median redshift was adopted.

2.6 Defining the field galaxy population

To select field galaxies, we first needed to define suitable apertures which were representative of the field. We randomly selected 10^5 regions of the sky which were within the SDSS footprint and a minimum of 8.32 arcminutes away from any redMaPPer BCGs or other background aperture centers. Each of these circular apertures had an angular radius of 2.35 arcminutes, which corresponds to 1 Mpc at the median redshift $z_{med} = 0.37$ of our clusters. The minimum separation of 8.32 arcminutes ensured that these field apertures would not overlap with any clusters or with each other, even at a redshift of $z = 0.2$, the lowest of our clusters' redshifts. In total, the selected field regions of the sky covered 1727701 square arcminutes (equivalent to 479.9 square degrees).

Chapter 3

Investigating the effects of global environment on galaxy evolution in clusters

In this chapter we address our investigation into the effects of global environment and redshift on galaxies in clusters. Specifically, we determine the relationships between a cluster's richness and its red fraction and giant-to-dwarf ratio. We begin give a detailed description of the methods used to make the measurements and move on to the results and a discussion of their implications for galaxy evolution (refer to Section 3.9 for the red fraction results and to Section 3.11 for the giant-to-dwarf ratio results). Figure 3.1 is a flowchart providing an overview of the steps taken in this chapter; details will be given within the chapter.

3.1 Stellar population synthesis

To perform the analysis detailed in this thesis, we needed to be able to convert between apparent and absolute magnitudes. Doing so allowed us to correct for completeness, as described in Section 3.4, and to determine the giant/dwarf cutoff magnitudes used in Section 3.10.

To convert between absolute and apparent magnitudes, one uses the cosmological distance modulus, described in Section 3.2 and defined by Equation 3.1. Evaluating the equation requires knowledge of what a typical cluster member galaxy's spectrum looks like and how it evolves with redshift; this is not something we had access to, as we were using photometric data only. To work around this, we performed stellar population synthesis with the Python bindings for the FSPS (Flexible Stellar Population Synthesis) package (Conroy & Gunn (2010), Conroy et al. (2009)).

Our aim was to produce a model population which would match our redMaPPer clusters in color-redshift space as closely as possible. To do so, we began by plotting

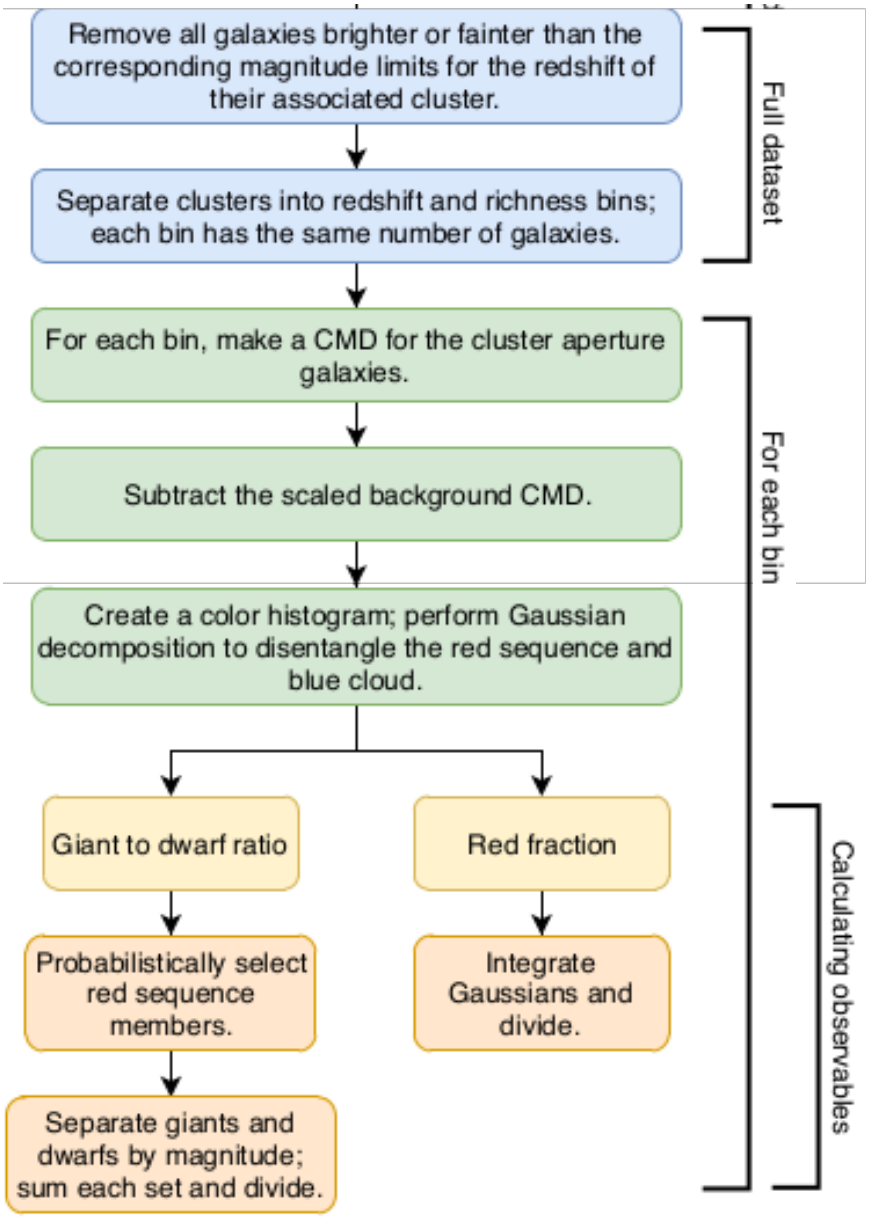

Figure 3.1: Flowchart of steps taken in Chapter 3.

the colour evolution of the BCGs of our clusters with respect to redshift. These datapoints are the blue dots in Figure 3.2. We then separated all of these datapoints into bins with respect to redshift and calculated each bin's respective median color and its standard deviation. Finally, we defined a simple model stellar population and varied its parameters until its color vs. redshift curve matched our black points as closely as possible. We used a non-linear least squares method to ensure the best fit. There is degeneracy between the effects of a stellar population's age and it's metallicity, so we had the choice of which of these two parameters to leave free. De Lucia et al. (2007) determined that for red sequence galaxies, age is the more important factor, so we chose to fix our model population's metallicity and leave age as the free parameter. At our median redshift of $z = 0.37$, the model stellar population we obtained with solar metallicity was 9.43 Gyr old, and the universe was 9.64 Gyr old. This means the population formed 0.21 Gyr after the universe did, corresponding to a formation redshift of $z = 17.99$. This value is much too high for a realistic formation redshift, and if we were doing a detailed stellar population analysis, we could vary other parameters such as metallicity to generate a more accurate formation redshift. For the purposes of this thesis, though, we only need a model which fits our data and allows us to calculate k-corrections accurately, and this model is sufficient for doing so.

3.2 Cosmological distance modulus calculations

The cosmological distance modulus allows us to convert between apparent and absolute magnitudes, taking into account an object's redshift, passive stellar evolution, and the filter through which it is observed. The cosmological distance modulus is defined by:

$$m_\lambda(z) - M_\lambda = 25 + 5\log[d_L(z)] + k_\lambda(z) + e_\lambda(z), \tag{3.1}$$

where m_λ is the apparent magnitude of a source at a given wavelength, M_λ is the source's absolute magnitude at that same wavelength, $d_L(z)$ is the luminosity distance of the source, $k_\lambda(z)$ is the k-correction factor which accounts for the filter through which the source is observed, and $e_\lambda(z)$ is a correction factor which accounts for the source's evolution with redshift. $k_\lambda(z) + e_\lambda(z)$ is known as the (e+k) correction, and it will be described in Section 3.2.1.

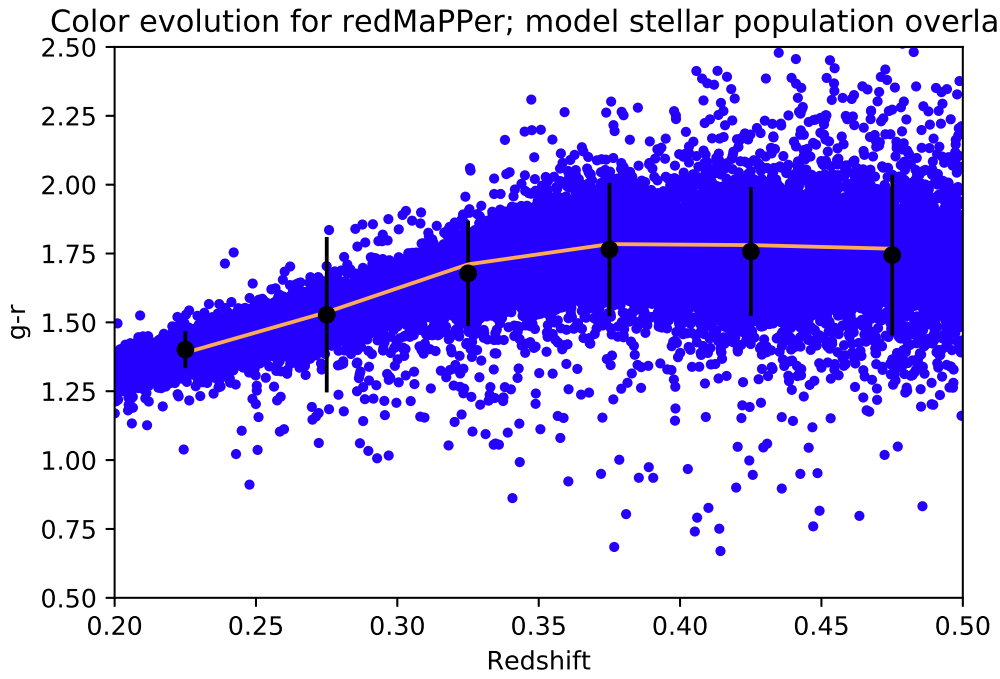

Figure 3.2: Color evolution for redMaPPer with model stellar population overlaid. Blue datapoints represent the BCGs of our entire sample of redMaPPer clusters. These datapoints were separated into bins with width $\Delta z = \pm\, 0.025$, and then the median and standard deviation within each bin was used to create the black data points and error bars respectively. The orange line is the color evolution with respect to redshift of our model stellar population, produced with the Python bindings for the FSPS package (Conroy & Gunn, 2010; Conroy et al., 2009)

.

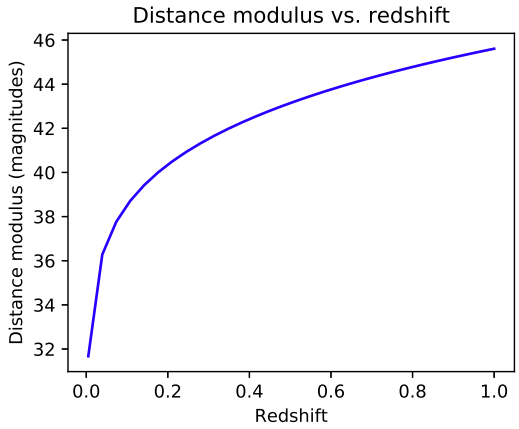

Figure 3.3: Distance modulus evolution with redshift for our model stellar population.

Using Astropy's `cosmology` package (Robitaille et al. (2013), Price-Whelan et al. (2018)) to calculate the luminosity distance and the Python bindings for the FSPS (Flexible Stellar Population Synthesis) package (Conroy & Gunn (2010), Conroy et al. (2009)) to calculate the (e+k) corrections, we were able to produce Figure 3.3, which shows how the distance modulus for our model stellar population evolves with redshift.

3.2.1 (e+k) corrections

As an astronomical source's spectrum is redshifted, different parts of its spectrum will pass through the band of the filter through which the spectrum is observed. Additionally, the source may experience passive or active stellar evolution with respect to redshift. These sources of evolution are included in our stellar population model. To account for these two effects when calculating the cosmological distance modulus given by Equation 3.1, we must calculate a quantity known as an (e+k) correction.

If $S(\lambda)$ is the spectral flux received from some source as a function of wavelength and $R(\lambda)$ filter response, $t(z)$ is the time corresponding to the redshift of the source, then we can define the wavelength-dependent (e+k) correction $(e+k)_\lambda$ at the source's redshift z by:

$$(e+k)_\lambda(z) = 2.5\log(1+z) - 2.5\log\left[\frac{\int_0^\infty S(\lambda/1+z, t(z))R(\lambda)\mathrm{d}\lambda}{\int_0^\infty S(\lambda, t(z=0))R(\lambda)\mathrm{d}\lambda}\right]. \tag{3.2}$$

The model stellar population generated in the previous step was used to create the spectrum shown in blue in Figure 3.4. In the figure it is shown at redshift $z = 0$, but

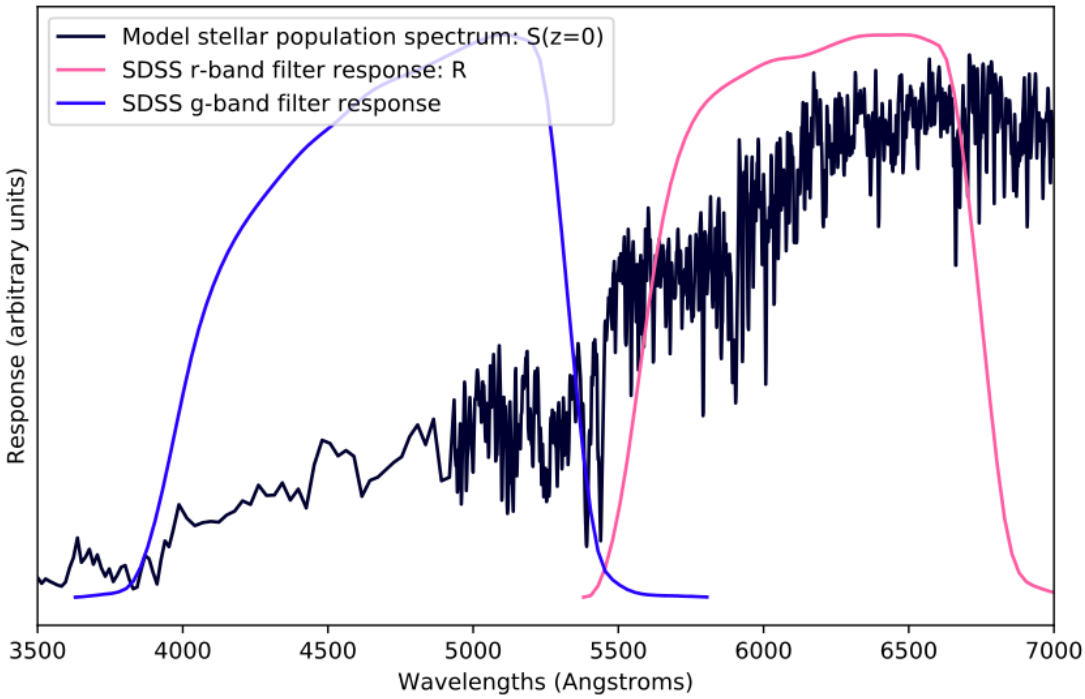

Figure 3.4: Spectral response of the SDSS r-band filter (given in Equation 3.2 as $R(\lambda)$) and model stellar population spectrum at our median cluster redshift $z = 0.37$ (given in Equation 3.2 as $S(\lambda, t(z = 0))$, as calculated by FSPS (Conroy & Gunn (2010), Conroy et al. (2009)). While the SDSS g-band filter is not used when calculating (e+k) corrections, it is included in the figure for reference. Units along the y-axis are arbitrary due to the ratio nature of Equation 3.2, as is the relative scaling between the curves. Filter response data from Gunn et al. (1998).

to calculate the (e+k) corrections it was redshifted continuously along the range from $z = 0$ to $z = 1$. This spectrum is mathematically represented as $S(\lambda)$, and the SDSS r-band filter response curve shown in red in the same figure represents $R(\lambda)$. Using these curves to evaluate Equation 3.2, we produced Figure 3.5, the (e+k) corrections for our model stellar population as a function of redshift. The results were used to evaluate the cosmological distance modulus given by Equation 3.1.

3.3 Creating redshift and richness bins

To avoid the issues inherent to low number statistics and the tails of the redshift distribution, the redMaPPer clusters of redshift less than $z = 0.2$ and greater than $z = 0.5$ were discarded. This amounted to 16.9% of the cluster population being discarded, leaving 21709 clusters for the analysis.

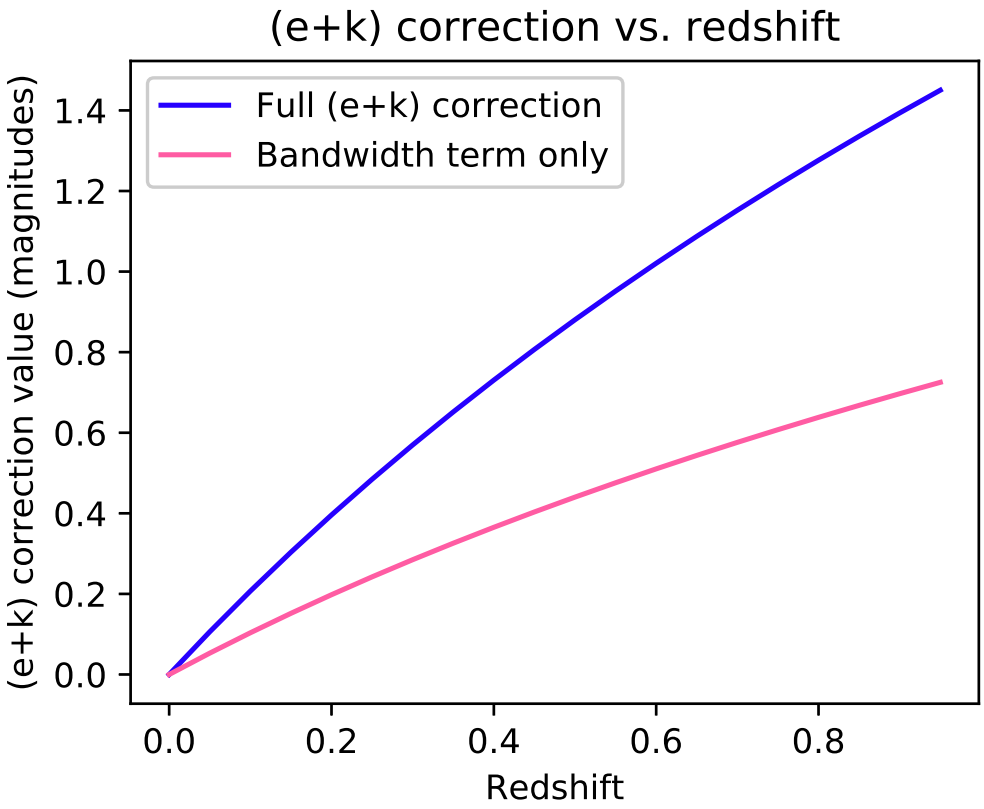

Figure 3.5: Calculated (e+k) corrections as a function of redshift for our model stellar population as observed through the SDSS r-band filter are shown in blue. For comparison, the bandwidth term of the (e+k) correction, given by $2.5\log(1+z)$, is plotted in pink.

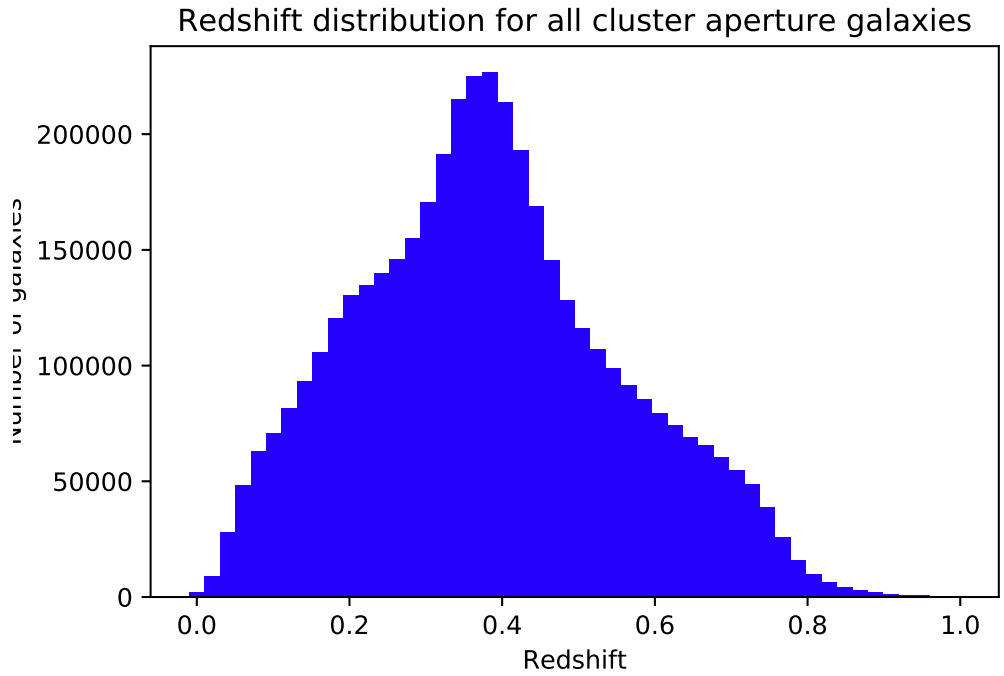

Figure 3.6: Redshift distribution of SDSS galaxies from cluster apertures.

The remaining clusters were grouped into 5 bins in redshift such that each bin contained an approximately equal number of clusters. For the redshift distribution of redMaPPer's clusters with bin edges overlaid, see Figure 2.1. Figure 3.6 shows the redshift distribution for the cluster aperture galaxies.

We then further subdivided each redshift bin's worth of clusters into five richness bins, such that each richness bin held an approximately equal number of clusters. The result is 25 bins which each cover a region of redshift-richness space, and they are summarized in Table 3.2.

Redshift	Number of clusters	Number of galaxies
0.2 - 0.2945	4342	116271
0.2945 - 0.3538	4343	104686
0.3538 - 0.3936	4342	110095
0.3936 - 0.4366	4343	110515
0.4366 - 0.5	4343	124894

Table 3.1: Summary of redshift bins. Note that the column for numbers of galaxies represents galaxies left in the cluster apertures after applying magnitude cuts to ensure completeness and avoid saturation.

Redshift	Richness	Number of clusters	Number of galaxies
0.2 - 0.2945	19.9 - 22.4	874	19983
0.2 - 0.2945	22.4 - 25.6	871	21428
0.2 - 0.2945	25.6 - 30.4	874	22740
0.2 - 0.2945	30.4 - 39.1	869	24753
0.2 - 0.2945	39.1 - 199.5	871	30783
0.2945 - 0.3538	19.9 - 22.3	869	18045
0.2945 - 0.3538	22.3 - 25.1	875	18045
0.2945 - 0.3538	25.1 - 29.8	872	19804
0.2945 - 0.3538	29.8 - 38.8	872	21684
0.2945 - 0.3538	38.8 - 166.2	870	26650
0.3538 - 0.3936	19.9 - 23.5	872	19704
0.3538 - 0.3936	23.5 - 26.9	869	20157
0.3538 - 0.3936	26.9 - 31.7	871	20849
0.3538 - 0.3936	31.7 - 40.7	871	22285
0.3538 - 0.3936	40.7 - 189.3	870	27376
0.3936 - 0.4366	22.0 - 27.6	870	17788
0.3936 - 0.4366	27.6 - 31.2	872	17788
0.3936 - 0.4366	31.2 - 36.3	874	21613
0.3936 - 0.4366	36.3 - 46.3	869	24132
0.3936 - 0.4366	46.3 - 248.4	870	27940
0.4366 - 0.5	25.2 - 34.8	872	23161
0.4366 - 0.5	34.8 - 39.4	872	23674
0.4366 - 0.5	39.4 - 45.3	872	24288
0.4366 - 0.5	45.3 - 55.7	869	25105
0.4366 - 0.5	55.7 - 299.5	870	28970

Table 3.2: Summary of redshift and richness bins. Note that the column for numbers of galaxies contained represents galaxies left in the cluster apertures after applying magnitude cuts to ensure completeness and avoid saturation.

Redshift	r_{cut}
0.2 - 0.2945	19.55
0.2945 - 0.3538	20.33
0.3538 - 0.3936	20.77
0.3936 - 0.4366	21.17
0.4366 - 0.5	21.53

Table 3.3: r-band apparent completeness cut magnitudes r_{cut} for each redshift bin.

3.4 Ensuring photometric completeness

One complication when analyzing surveys which span a range of redshifts is how to ensure an equal level of completeness with respect to redshift of observed objects of varying magnitudes. This is achieved empirically by observing the distribution of apparent magnitudes of all objects observed in the survey, and then determining an absolute magnitude by which to discard all fainter objects on the basis that they may not be detected in the higher redshift areas of the survey. In this way, one can say that their remaining objects are complete to a given level of brightness.

For this work, we plotted the distribution of SDSS galaxies' apparent r-band magnitudes shown in Figure 3.7. Using the published SDSS r-magnitude fractional completeness of galaxies plot[1], we selected a faint limit of $r = 21.7$ in order to access the faintest galaxies possible while maintaining near 100% completeness. We then used our model stellar population described in Section 3.1 to evaluate the cosmological distance modulus given by Equation 3.1. Adopting the median redshift in our highest redshift bin, the cosmological distance modulus allowed use to convert the apparent magnitude we chose in the previous step to an absolute magnitude of $M_{abs,r} = -21.44$. This is the absolute magnitude representing the faintest objects we can observe with confidence that they are statistically representative of their entire population within the redshift range we cover from $z = 0.2$ to $z = 0.5$. Using the cosmological distance modulus again, we were able to convert this absolute magnitude back to an apparent magnitude using the central redshift in each of our bins. The results are summarized by Table 3.3. For each redshift bin, we discarded all galaxies fainter than this limiting magnitude.

[1] Available at https://www.sdss.org/dr14/imaging/other_info/#DepthsoftheSDSSphotometricsurvey.

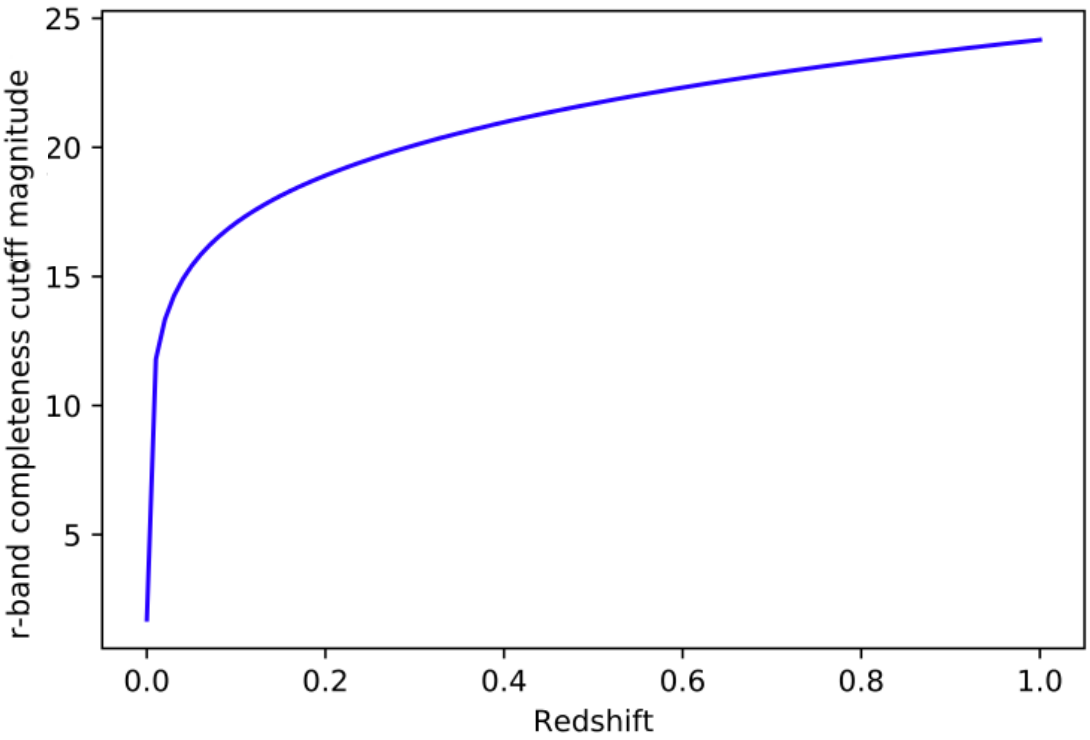

Figure 3.7: SDSS r-band magnitude apparent faint cutoff magnitudes versus redshift. Cutoffs for each redshift bin are listed in Table 3.3.

3.5 Statistical background subtraction to select cluster member galaxies

The next step was to determine which of the galaxies within the cluster apertures were actual members of the cluster, and which of those galaxies were field galaxy contaminants. We use a statistical background subtraction approach to solve this problem (Aragon-Salamanca et al., 1993; Stanford et al., 1998; Kodama & Bower, 2001; De Lucia et al., 2007; Bildfell et al., 2012, e.g.).

One of the primary benefits of having such a large sample size is that rather than definitively determining exactly which galaxies are members of exactly which clusters, we can used this binned statistical background subtraction approach to determine how many galaxies occupy a given area of parameter space for a certain category (in this case, redshift and richness make up the category) of cluster, and with that we can make statistical claims about clusters of that category in general.

3.5.1 Color magnitude diagrams

Statistical background subtraction was achieved by creating a binned colour-magnitude diagram (CMD) for the cluster aperture galaxies, and another one for the field aperture galaxies. The cells are identical in parameter space between the two CMDs. For an example for a single redshift-richness bin, see Figures 3.8 and 3.10. Figure 3.8 shows the CMD for galaxies within the redshift bin ranging $z = 0.35$ to $z = 0.4$ and the richness bin ranging from $\lambda = 27.1$ to $\lambda = 31.9$. Figure 3.10, meanwhile, shows the CMD for our sample of field galaxies. For the CMDs of cluster aperture galaxies in each redshift-richness bin respectively, see Figure 3.9.

Since the cells in each of the two CMDs are identical with respect to the parameter space they cover, one can simply subtract the value in each cell of the field galaxy CMD from the corresponding cell of the cluster aperture galaxy CMD to obtain a new, background-subtracted CMD which is statistically representative of only the galaxies which are true cluster members. Such a CMD is shown in Figure 3.12. Note the linear red sequence running horizontally at a g-r colour of approximately 1.75 and the more diffuse blue cloud below it. Some areas of slight over-subtraction are visible in black where the field population had more galaxies per cell than the cluster aperture population had. This implies the need for further scaling of the field galaxy populations, as described in the following section.

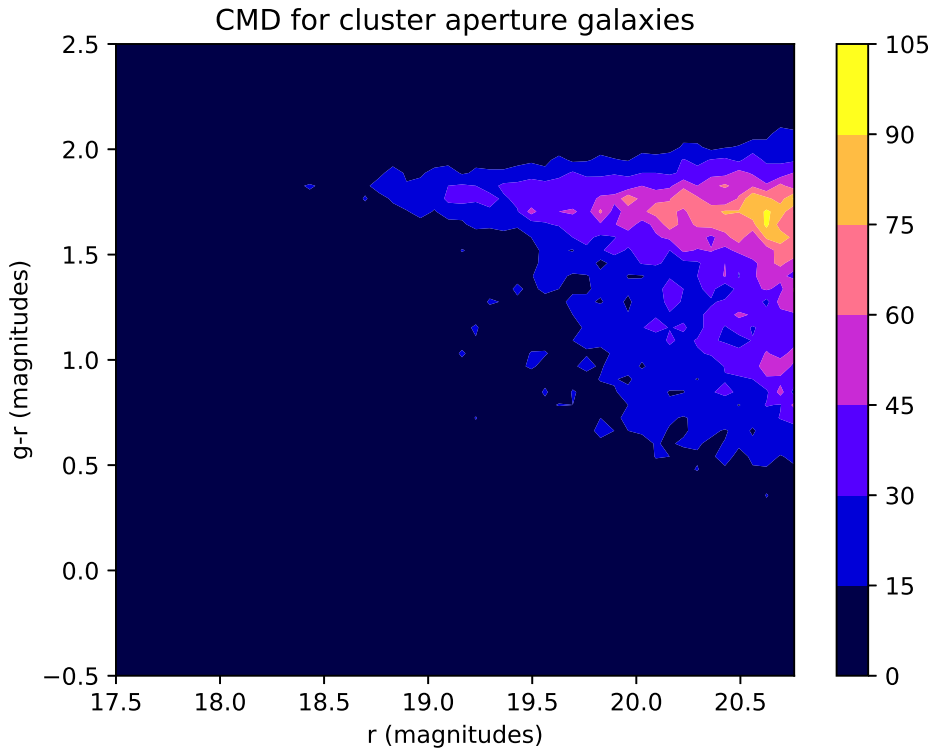

Figure 3.8: CMD for clusters within the redshift bin ranging $z = 0.35$ to $z = 0.4$ and the richness bin ranging from $\lambda = 27.1$ to $\lambda = 31.9$. Note the linear red sequence running horizontally at a g-r colour of approximately 1.75 as well the more globular-shaped blue cloud below it. These are both contributions from the cluster member galaxies, and they are overlapping the contributions from the field galaxies, which is shown in Figure 3.10.

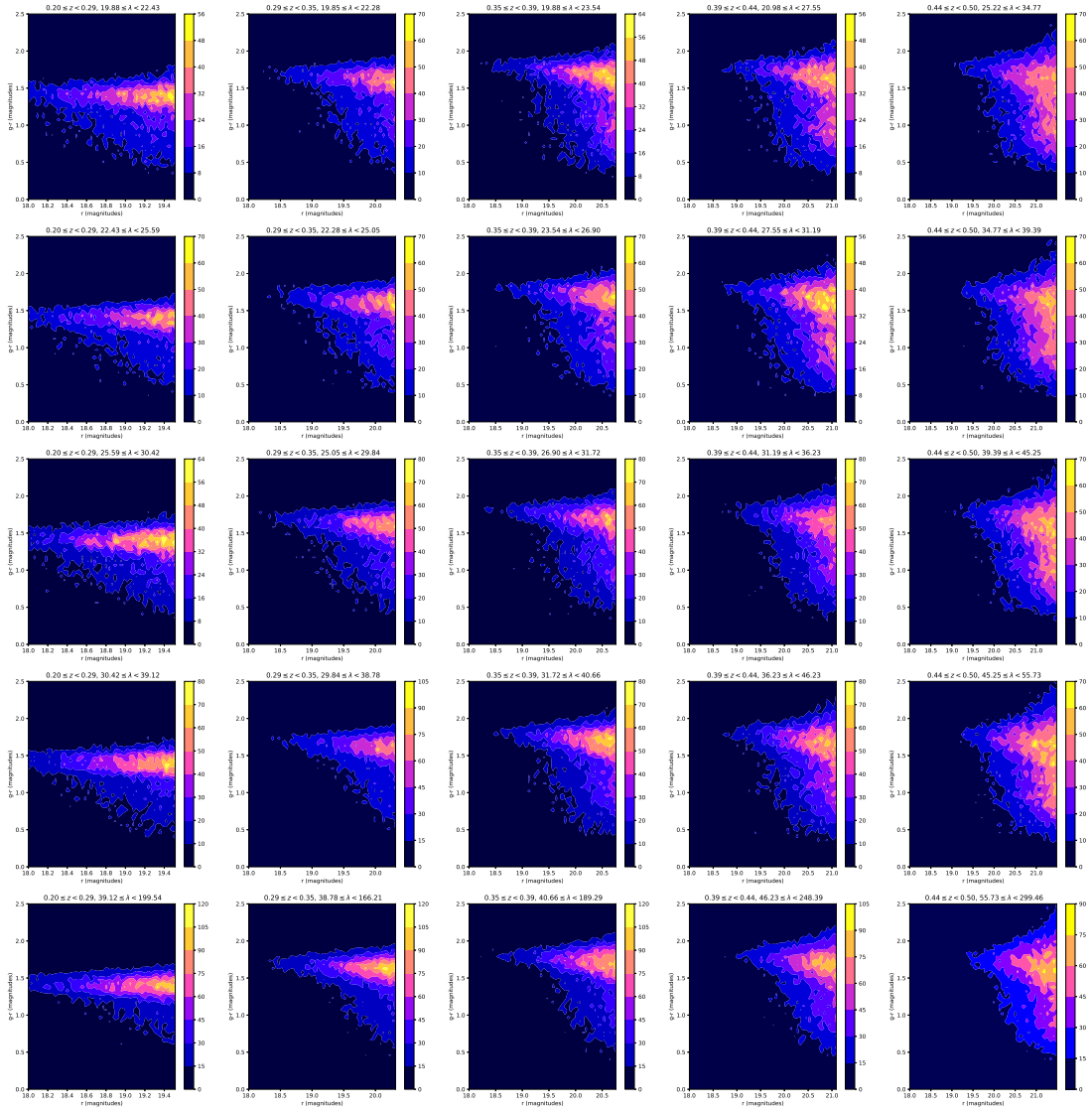

Figure 3.9: CMD of cluster aperture galaxies in each redshift-richness bin. Redshift increases from left to right, and richness increases from top to bottom.

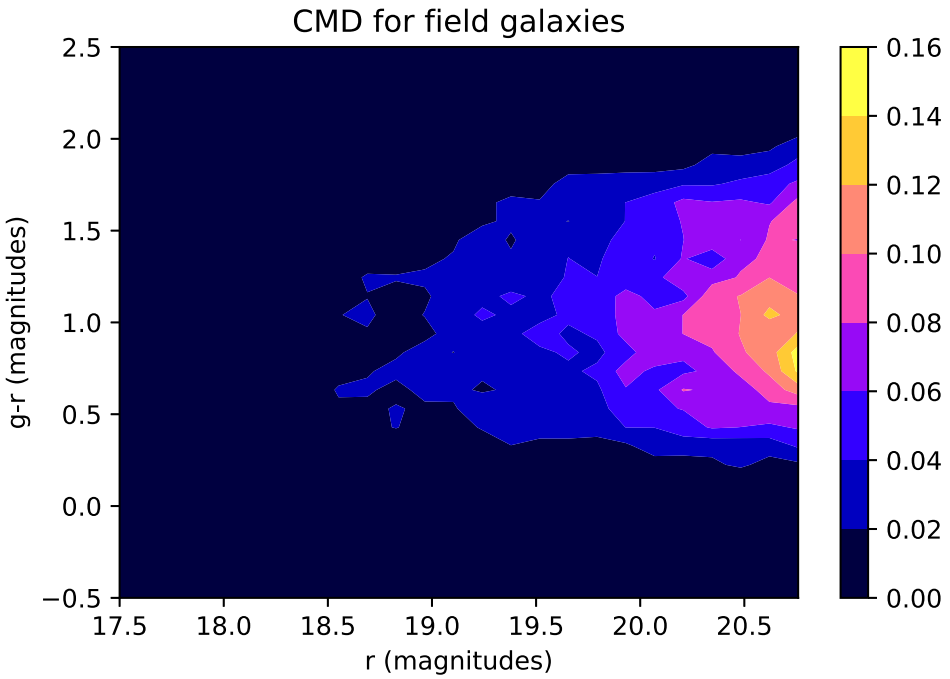

Figure 3.10: CMD for our selection of field aperture galaxies.

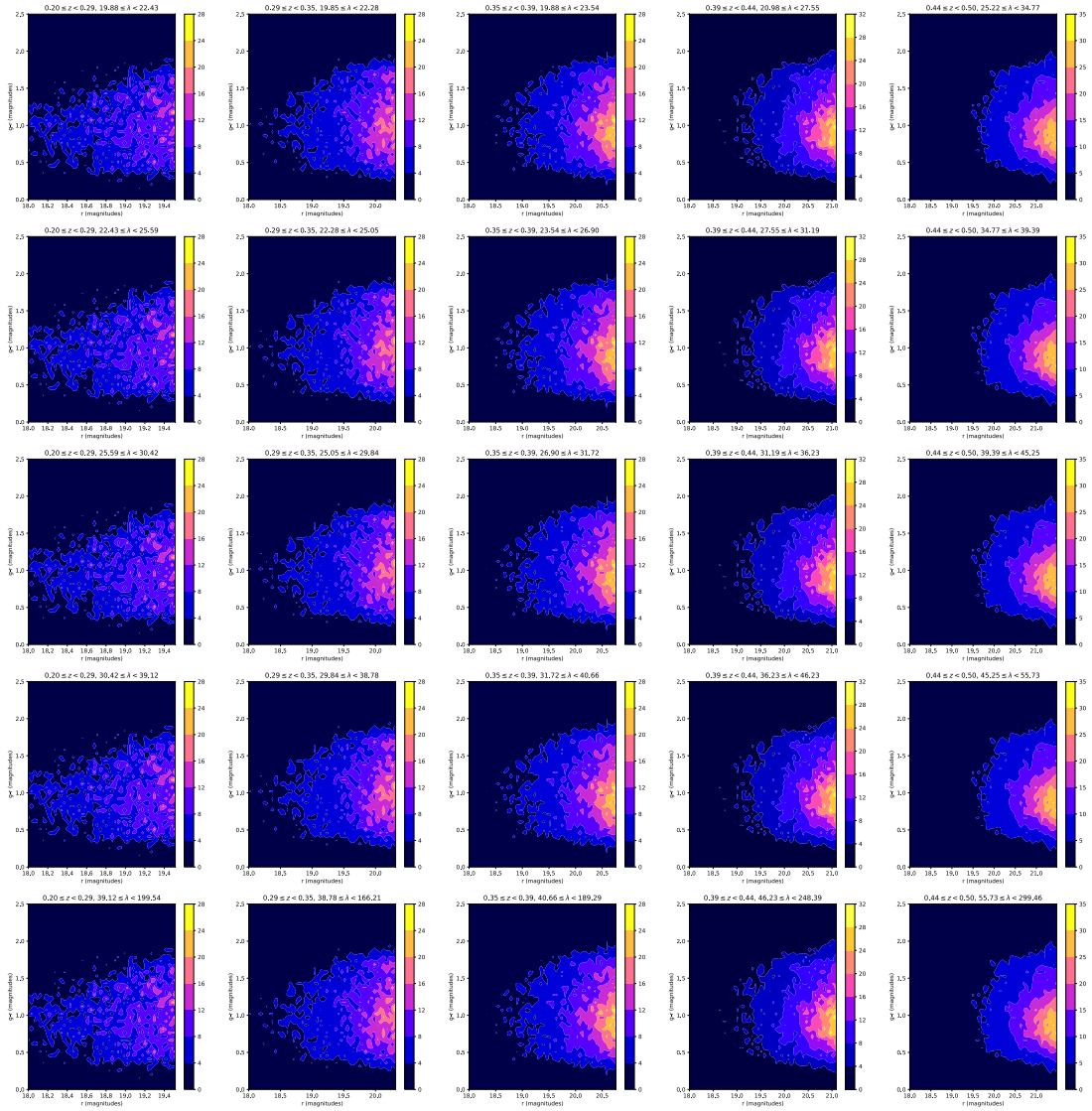

Figure 3.11: CMD of field galaxies, scaled for each redshift-richness bin. Redshift increases from left to right, and richness increases from top to bottom.

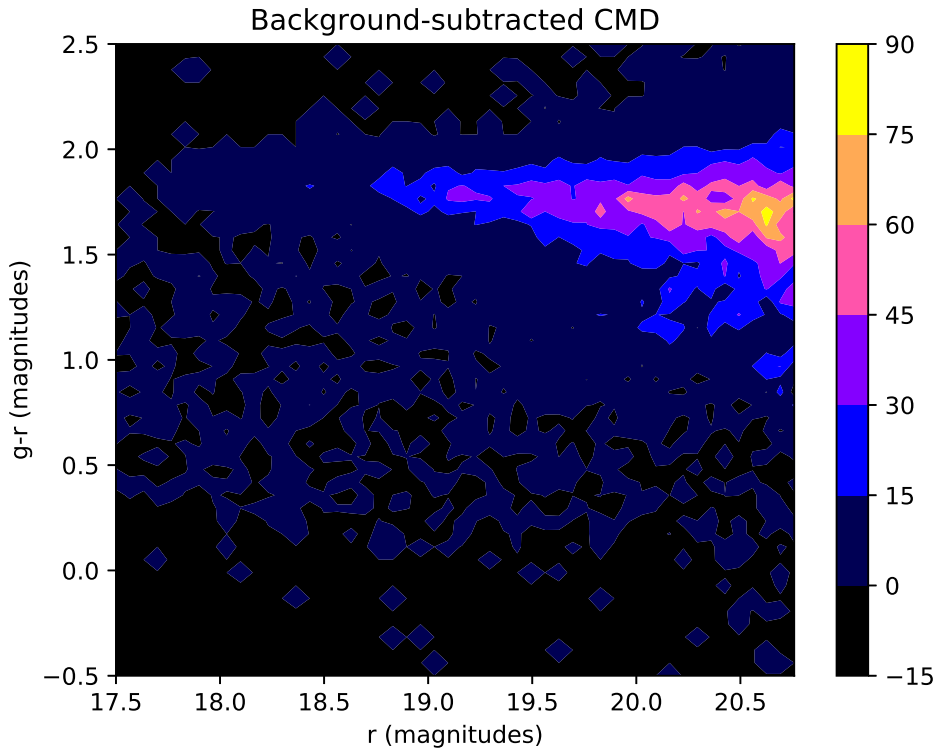

Figure 3.12: Background-subtracted cluster member colour-magnitude diagram for clusters within the redshift bin ranging $z = 0.35$ to $z = 0.4$ and the richness bin ranging from $\lambda = 27.1$ to $\lambda = 31.9$. Note the linear red sequence running horizontally at a g-r colour of approximately 1.75 and the more extended blue cloud below it. Some areas of slight over-subtraction are visible in black where the field population had more galaxies per cell than the cluster aperture population had.

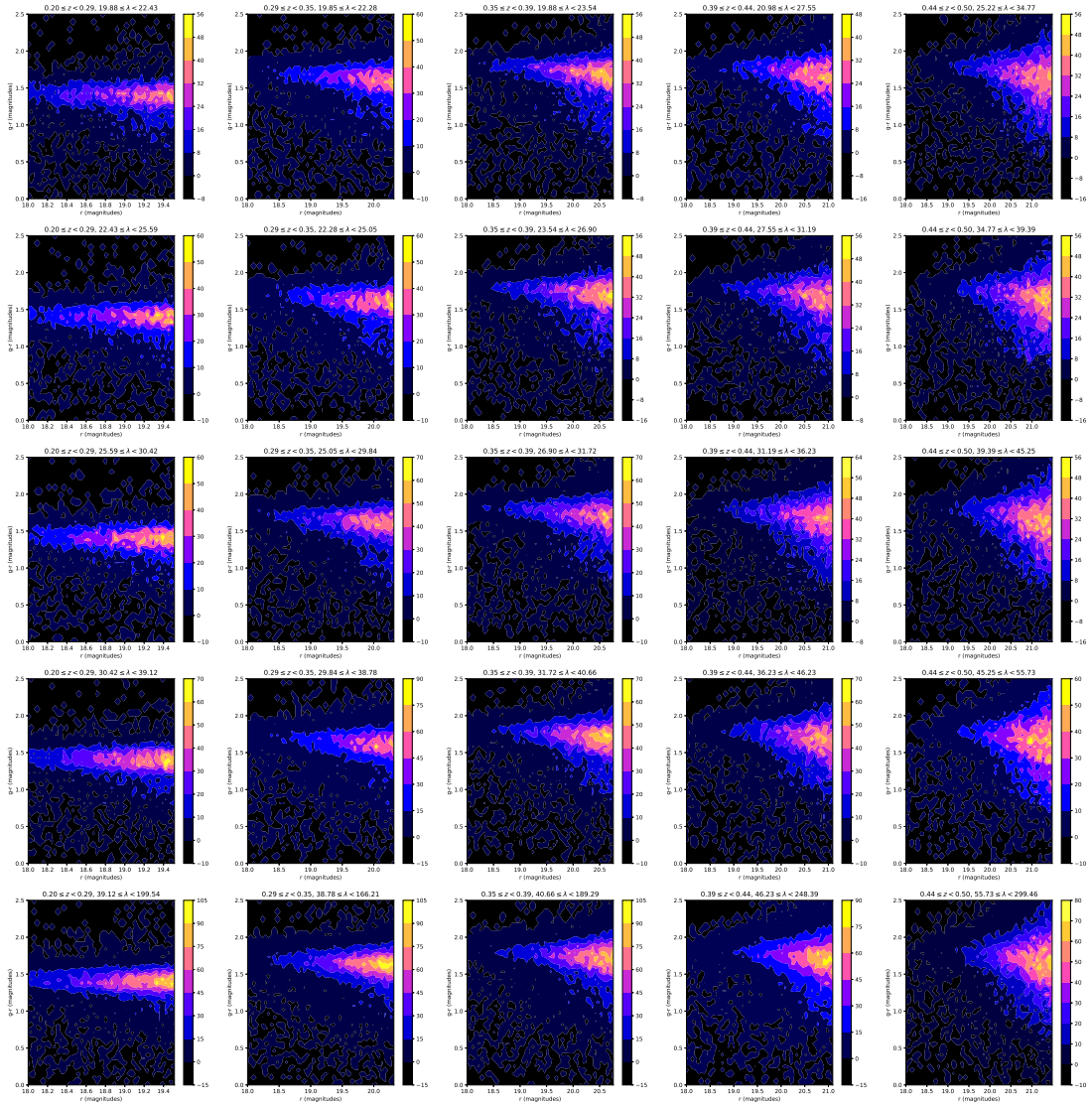

Figure 3.13: CMD for cluster member galaxies (post-background-subtraction) in each redshift-richness bin. Redshift increases from left to right, and richness increases from top to bottom.

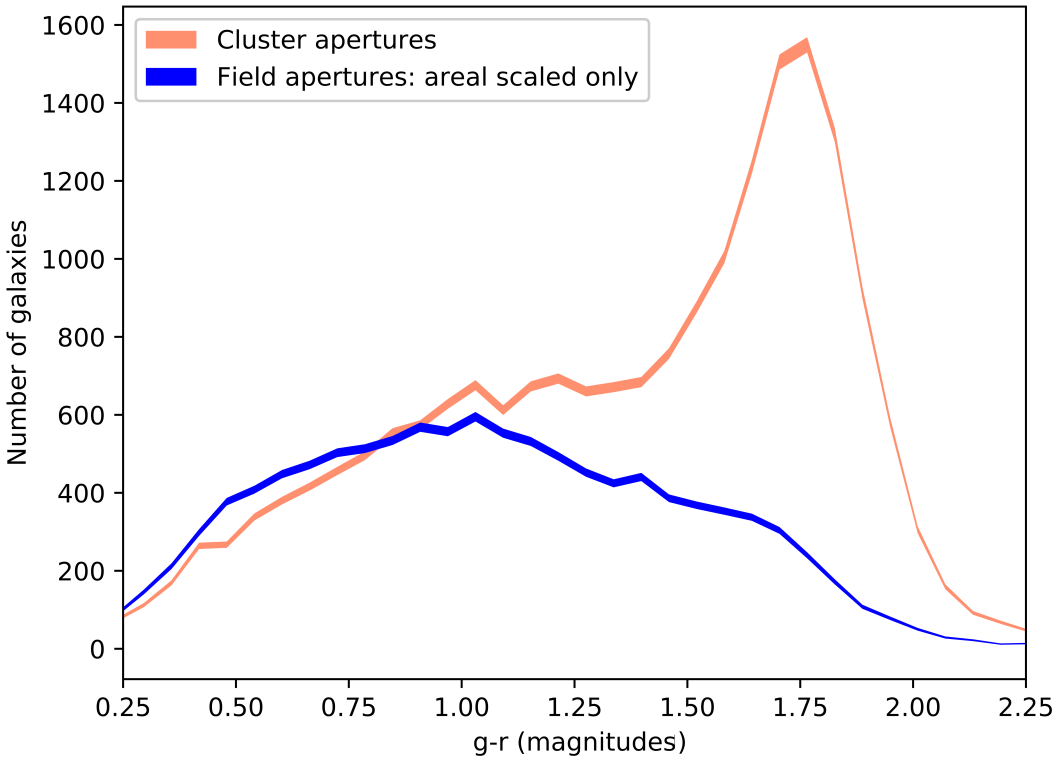

Figure 3.14: Pre-background subtraction color histogram for clusters within the redshift bin ranging $z = 0.35$ to $z = 0.4$ and the richness bin ranging from $\lambda = 27.1$ to $\lambda = 31.9$. The cluster aperture galaxy population is represented by the orange curve, and the field aperture galaxy population (after performing area scaling) is represented by the blue curve. Note the small region in which the blue curve is higher than the orange one; this represents over-subtraction, which is unphysical and supports the need for number scaling. Uncertainties are indicated by the width of the curves.

3.5.2 Color histograms

If we collapse the background-subtracted CMD in Figure 3.12 along the magnitude axis of the red sequence, we generate the black curve in Figure 3.15. In this figure, the cluster aperture galaxy population is represented by the cyan curve, and the field aperture galaxy population (after performing the area scaling described below) is represented by the magenta curve.

3.5.3 Background scaling

Most of the adjustment is performed by scaling the total sky area covered by our field apertures to the total sky area covered by our cluster apertures. Assuming that the universe is homogeneous and isotropic, the field should be statistically the same in any

region of the universe, so it will be acceptable to multiply our background population's color histogram curve by a scaling factor to account for the different areas covered. This scaling factor is simply the ratio of the area covered by the cluster apertures to the area covered by the field apertures. This correction is sufficient to perform a rough background subtraction, but some areas of under- and over-subtraction still occur. This is unphysical, so we continue to perform a smaller number scaling correction to account for cosmic variance as described below.

After performing many areal background subtractions, it was observed that almost no cluster member galaxies are present at $g-r$ values less than 0.5. Taking advantage of this observation, we scaled the field population by ensuring that the total number of galaxies with $g-r < 0.5$ was the same for the field population as it was for the cluster aperture population. In this way, we mitigated under- and over-subtraction, and we were able to perform background subtraction. The results for the sample redshift-richness bin are shown in Figure 3.15. It would be possible to perform both the areal and number scaling in a single step, but performing them separately creates the opportunity to check for cluster apertures with atypical color histograms by ensuring that the number scaling correction factor is only a few percent.

3.5.4 Uncertainty maps

For a given colour-magnitude cell on one of the CMDs, the uncertainty that a single galaxy from within that cell would contribute to a red fraction or GDR measurement was calculated. We assume Poissonian uncertainty, as is standard for counting experiments in nature. For a Poissonian distribution, the variance is equal to the mean. Therefore, since we are performing background subtraction, the uncertainty δ_{cell} in a given color-magnitude cell will be given by

$$\delta_{cell} = \sqrt{N_c + N_f} \tag{3.3}$$

where N_c is the number of cluster aperture galaxies in that cell, and N_f is the scaled number of field galaxies in that cell.

This quantity was calculated for each color-magnitude cell inside the CMDs in order to produce uncertainty maps, an example of which is shown in Figure 3.16. A unique uncertainty map was created for each redshift-richness bin and used for calculating the uncertainties on our red fraction and GDR measurements. For more details on how exactly these calculations were made, see Sections 3.8 and 3.10 respectively.

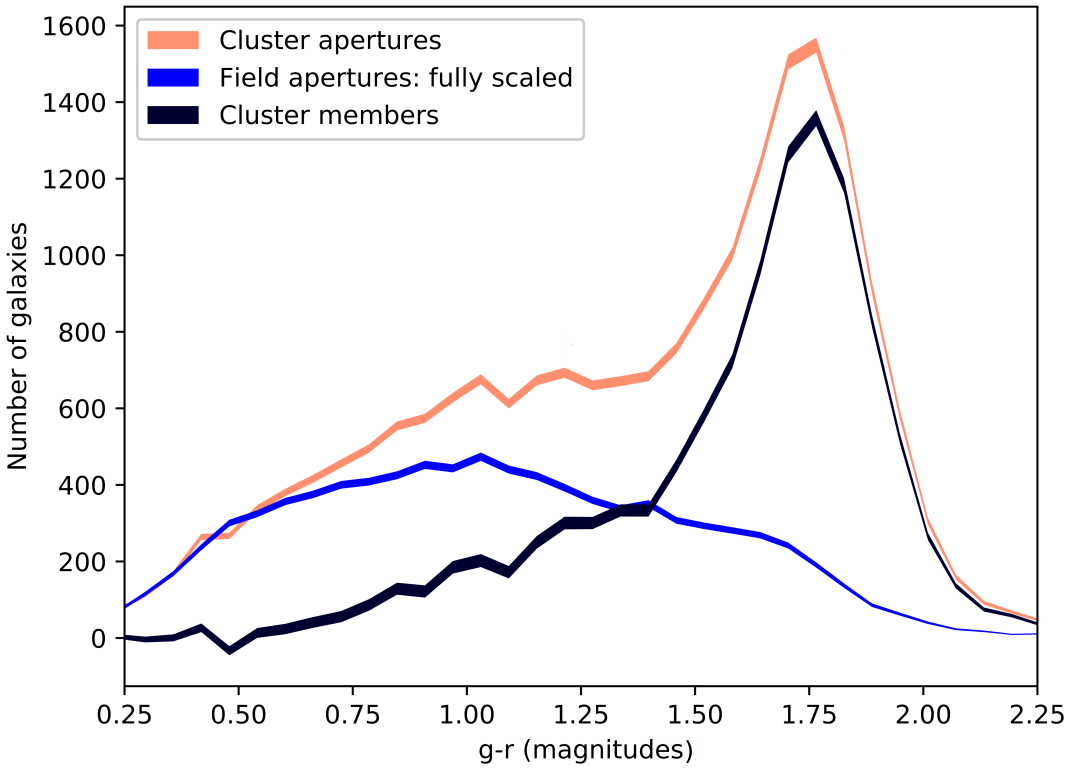

Figure 3.15: Color histogram, pre- and post- background subtraction for clusters within the redshift bin ranging $z = 0.35$ to $z = 0.4$ and the richness bin ranging from $\lambda = 27.1$ to $\lambda = 31.9$. The cluster aperture galaxy population is represented by the orange curve, and the field aperture galaxy population is represented by the blue curve. When we subtract the blue curve from the orange one, we obtain the black curve which represents the cluster member galaxy population. The uncertainty for each curve is indicated by its thickness.

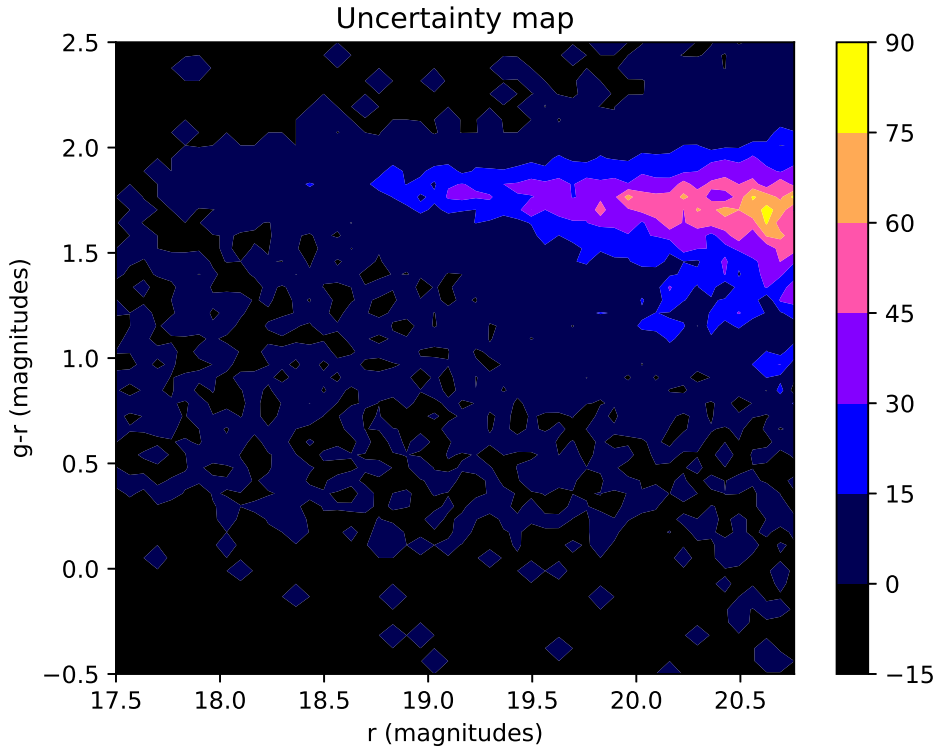

Figure 3.16: The uncertainty map for the redshift bin ranging $z = 0.35$ to $z = 0.4$ and the richness bin ranging from $\lambda = 27.1$ to $\lambda = 31.9$. The value in each colour-magnitude cell represents the uncertainty contribution that a single galaxy within that cell would contribute when calculating red fraction or GDR. More details are given in Section 3.5.4.

3.6 Disentangling red sequence and blue cloud populations

Now that the statistical background subtraction is complete, we have an accurate measure for the cluster galaxy population, which consists of galaxies from the red sequence and blue cloud populations (see Figure 3.14). In order to separate the individual contributions of these two groups, it was assumed that each population followed a Gaussian distribution on the basis of the central limit theorem, similarly to Baldry et al. (2004) and Balogh et al. (2004). This theorem states that given a sufficiently large sample size from a population with a finite level of variance (such as our cluster and field galaxy samples), the mean of all samples from the same population will be approximately equal to the mean of the population. Simply put, this means that if we sample enough galaxies, eventually their distribution should look like a Gaussian. With this in mind, we defined a function $G(x)$ such that:

$$G(x) = C_{RS}e^{-(x-\mu_{RS})^2/(2\sigma_{RS}^2)} + C_{BC}e^{-(x-\mu_{BC})^2/(2\sigma_{BC}^2)}, \tag{3.4}$$

where the first and second terms represent the contributions from the red sequence and blue cloud populations respectively. For each, μ represents the population's mean g-r colour, σ represents its standard deviation in g-r colour, and C is a scaling factor. x here represents a g-r colour, and so $G(x)$ represents the value of the collective red sequence and blue cloud population at that colour.

We then perform a non-linear least squares fitting to determine the optimal values for C_{RS}, μ_{RS}, σ_{RS}, C_{BC}, μ_{BC}, and σ_{BC}. Doing so for the same redshift and richness bin used in the previous section to perform background subtraction, we obtained Figure 3.17. The black curve here is the result of the statistical background subtraction performed in Section 3.5. It represents the cluster member galaxy population, and is the same as the purple curve in Figure 3.14. The red and blue curves represent the fitted red sequence and blue cloud respectively. The same plot for every redshift-richness bin is shown in Figure 3.18.

To visually check the goodness-of-fit, the sum of the red sequence and blue cloud curves is plotted in green in Figures 3.17 and 3.18. Upon inspection, it is very nearly identical to the black curve with which we began, indicating that our fitted red sequence and blue cloud populations are a good match for the overall cluster member galaxy population. For a quantitative check of goodness-of-fit, the standard deviation

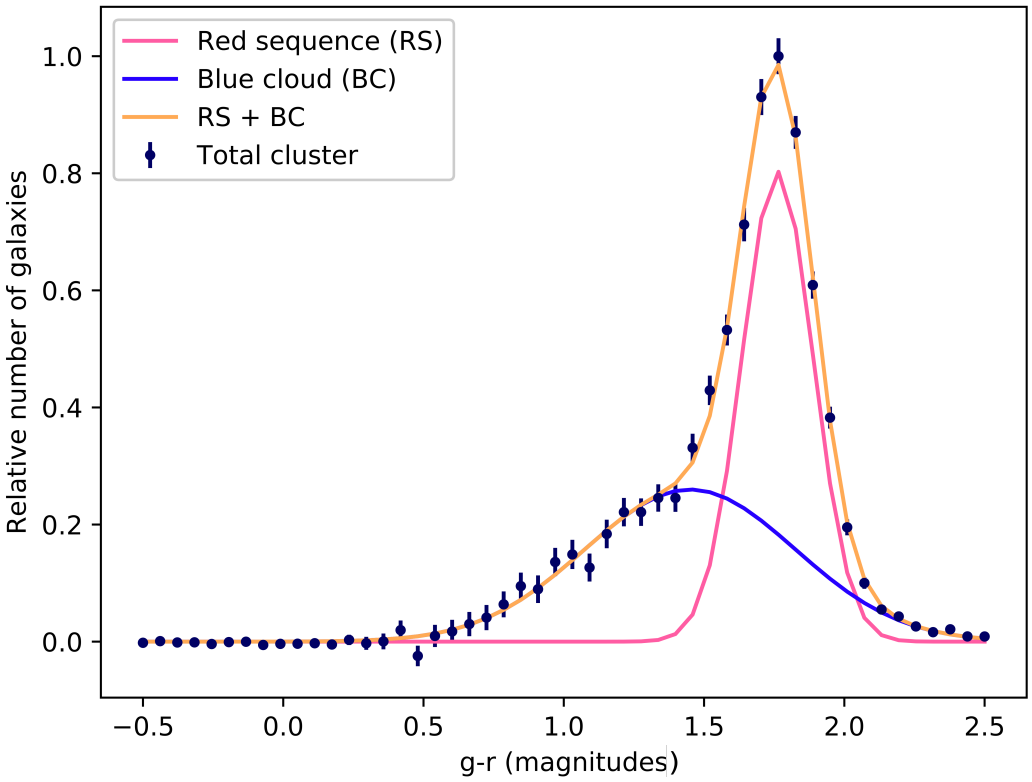

Figure 3.17: Color histogram for red sequence and blue cloud decomposition. The dark blue points here are the result of the statistical background subtraction performed in Section 3.5. They represents the cluster member galaxy population and follow the orange curve in Figure 3.14. The pink and blue curves represent the fitted red sequence and blue cloud respectively. To visually check the goodness-of-fit, the sum of the red sequence and blue cloud curves is plotted in orange.

of each fitted parameter for each of the 25 redshift-richness bins is shown in Figure 3.19.

3.7 Validating calculations with synthetic data

In order to ensure there was no bias in our methods of analysis, it was necessary to create synthetic data with injected properties and to test how well those properties could be recovered. See Figure 3.20 for an example of a CMD of a set of clusters we synthesized to have a red fraction of 0.5 as well as the CMD of a population of field galaxies we synthesized.

We varied the injected red fraction between 0.1 and 0.9 in increments of 0.1 and completed 10 realizations of each injected red fraction in which we generated a dataset

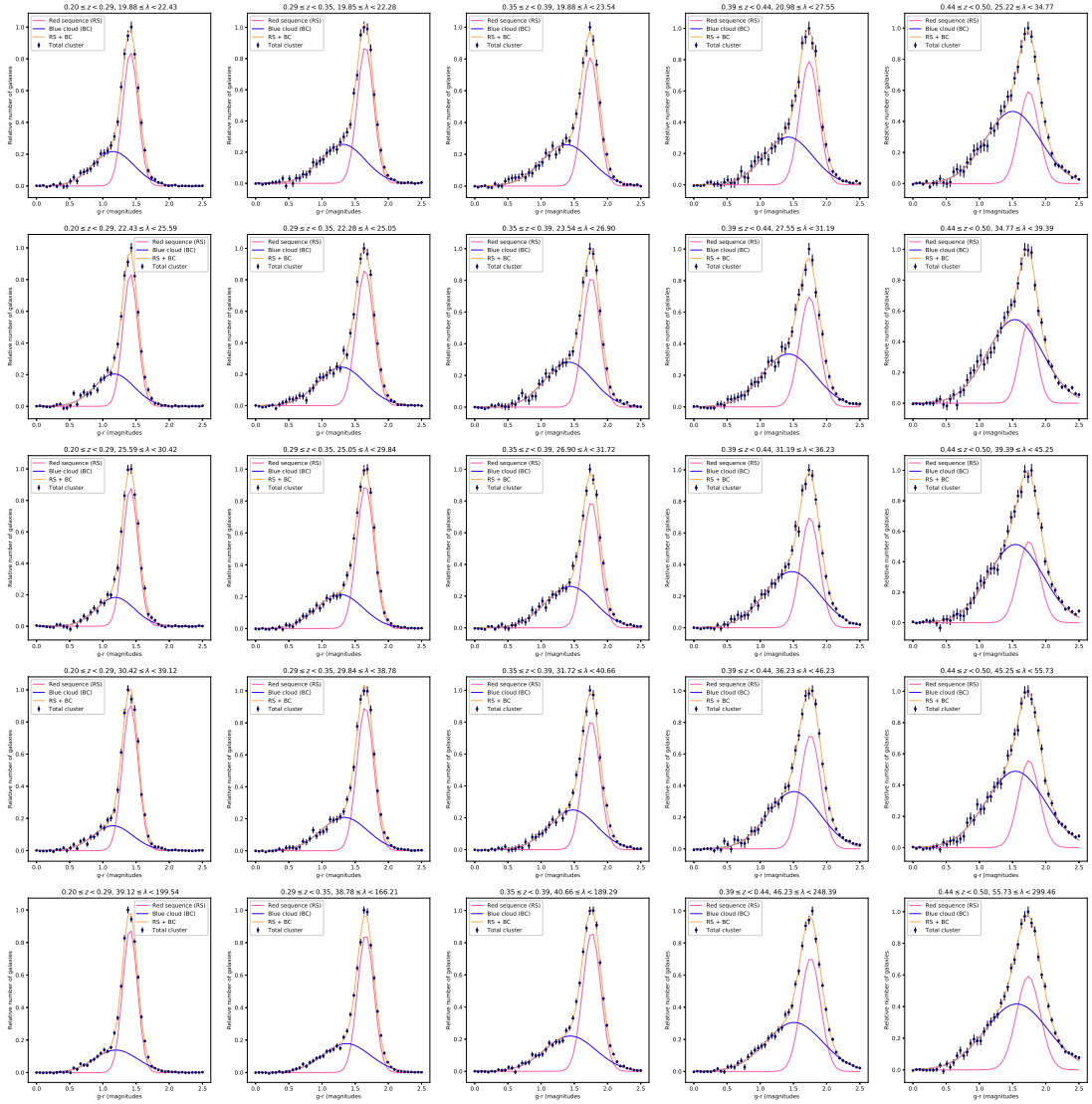

Figure 3.18: Color histogram for red sequence and blue cloud decomposition for each redshift-richness bin. The dark blue points here are the result of the statistical background subtraction performed in Section 3.5. They represents the cluster member galaxy population and follow the orange curve in Figure 3.14. The pink and blue curves represent the fitted red sequence and blue cloud respectively. To visually check the goodness-of-fit, the sum of the red sequence and blue cloud curves is plotted in orange.

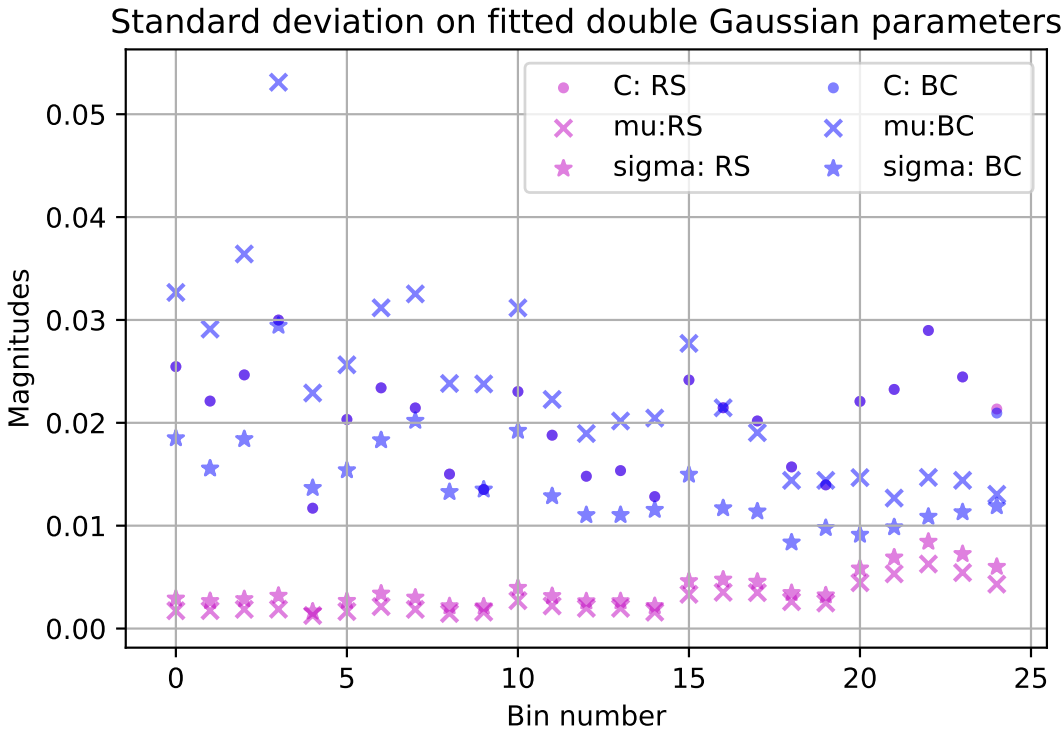

Figure 3.19: Standard deviation for each fitted parameter when disentangling the red sequence and blue cloud populations. The parameters corresponding to the red sequence are represented by pink, and the parameters corresponding to the blue cloud are represented by blue.

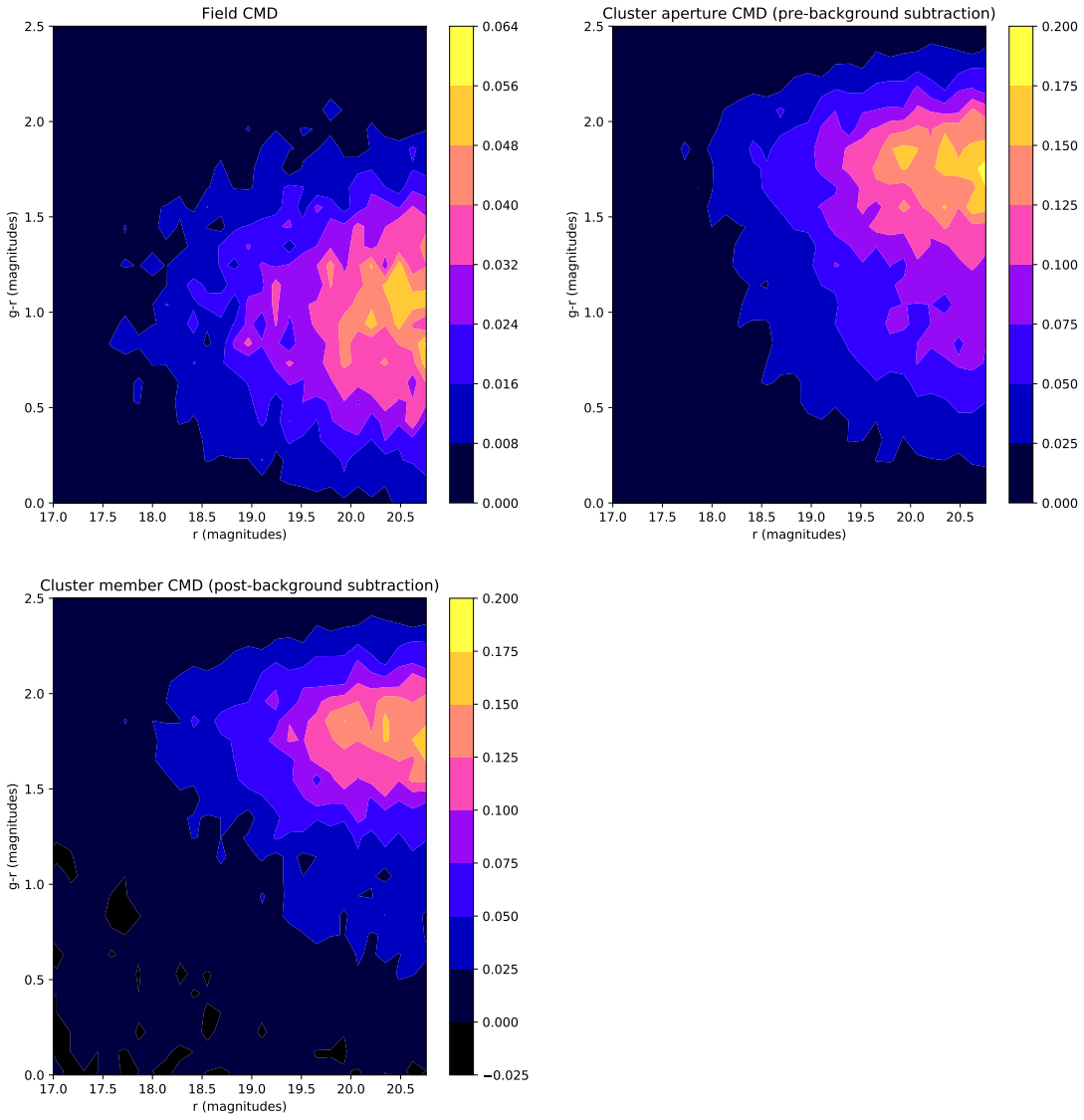

Figure 3.20: CMD of synthetic data with a red fraction of 0.5, pre- and post- background subtraction. We also synthesized the population of field galaxies represented in the upper right panel to match our background sample as closely as possible.

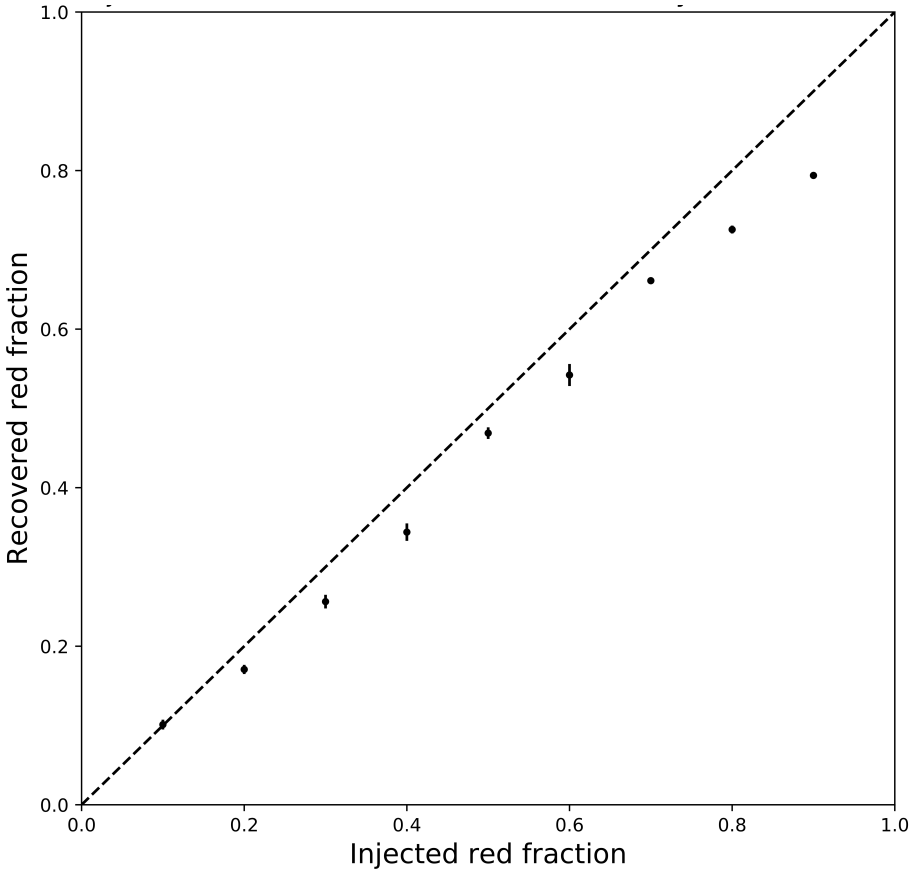

Figure 3.21: Injected versus recovered red fractions of synthesized data for 10 realizations at each injected red fraction value. Error bar lengths are calculated using the standard error on the mean. The dashed line shows the ideal one-to-one relation between the injected and recovered red fraction values.

and then measured its red fraction as described in this chapter. For the results, see Figure 3.21. We see that at all red fraction values, we are slightly underestimating the injected value; however, the slope of our true-versus-recovered red fraction is approximately 1, so this underestimation will not affect our results when we compare internally between redshift-richness bins.

3.8 Calculating red fraction as a function of cluster richness

After performing the Gaussian decomposition detailed in Section 3.6, we began with the simple method of analytically calculating the integral of each individual Gaussian profile to get the area under the curve. We then evaluated Equation 1.2, where n_{red} was the integral of the Gaussian representing the red sequence galaxies, and n_{total} was

the sum of both integrals.

Calculating uncertainty

As red fraction is a division-based measurement, we can refer to Equation 1.2 and use the standard formulas for uncertainty propagation to calculate the uncertainty δ_{RF} on the red fraction f_R as follows:

$$\delta_{RF} = f_R \sqrt{\left(\frac{\delta N_{red}}{N_{red}}\right)^2 + \left(\frac{\delta N_{total}}{N_{total}}\right)^2} \tag{3.5}$$

where N_{red} is the number of red galaxies, N_{total} is the combined number of red and non-red galaxies, and δN_{red} and δN_{total} are their respective uncertainties. Calculating δ_{red} and δ_{total} requires another standard uncertainty propagation formula, this time for addition since these quantities are sums. Let us take N_{red} for an example; for each color-magnitude cell that contains a red galaxy, we can determine what uncertainty it alone will contribute using the Poissonian uncertainty maps produced in Section 3.5.4. We define the sums' uncertainties δN_{red} and δN_{total} by

$$\delta N_{red} = \sqrt{\sum_{i}^{N_{red\ cells}} (\delta g_i)^2} \tag{3.6}$$

and

$$\delta N_{total} = \sqrt{\sum_{i}^{N_{all\ cells}} (\delta g_i)^2} \tag{3.7}$$

where $N_{redcells}$ is the number of cells containing red galaxies, $N_{allcells}$ is the total number of cells used in the calculation, and δg_i is the individual uncertainty contribution from each color-magnitude cell.

3.9 Red fraction measurements

A galaxy cluster's red fraction is interesting as it tells us about the rate at which its red sequence is built up- that is to say, it tells us about the rate at which quenching occurs. This can be achieved by monitoring the typical cluster's red fraction with respect to redshift. Meanwhile, observing the change (or lack thereof) in clusters' red

fraction with respect to their richness can lend insight on how global environment affects quenching.

3.9.1 Red fraction as a function of redshift

The red fraction as a function of redshift for each cluster richness bin is shown in the top panel of Figure 3.22. Qualitatively, these results are in agreement with De Lucia et al. (2007), who observe that for their sample of optically-selected galaxy clusters in the redshift range from $z = 0.4$ to $z = 1$, blue fraction f_B increases with redshift from $f_b \approx 0.45$ to $f_b \approx 0.95$. As blue fraction is defined as one minus red fraction, our results are consistent with theirs. Urquhart et al. (2010) also observe an increase in blue fraction with redshift, this time using X-ray detected clusters over the redshift interval $0.15 \leq z \leq 0.41$.

The decrease of red fraction with redshift implies that as the universe ages, galaxies in clusters become redder and redder. This makes intuitive sense; as the short-lived, bright, blue stars in a galaxy die, the galaxy as a whole takes on a redder appearance. The slope of the relation between redshift and red fraction can tell us something about the rate at which cluster galaxies become redder, and therefore help constrain which quenching mechanisms may be significant in clusters.

3.9.2 Red fraction as a function of cluster richness

The red fraction as a function of cluster richness for each redshift bin is shown in the bottom panel of Figure 3.22. We see that red fraction does not vary significantly with cluster richness; rather, it is dominated by the effect of redshift. For comparison to the literature, we consider Urquhart et al. (2010), who observe a clear increase in red fraction with increasing cluster x-ray temperature- a proxy for cluster richness- in the range from 5 to 15 keV. Wake et al. (2005), however, do not observe any relation between red fraction and cluster mass (another proxy for richness) using a wider range of x-ray temperatures but a relatively small sample of 12 clusters.

While some other authors observe a trend in which red fraction increases with cluster richness, we do not. However, SDSS and redMaPPer are sensitive to only the brightest (and therefore richest) of clusters, while other datasets such as the X-ray Multi-Mirror (XMM) Large Scale Structure (LSS) survey (Willis et al., 2005) used by De Lucia et al. (2007) are sensitive to a wider range of cluster scales, even down to a level that could be considered groups rather than clusters. The redMaPPer algorithm

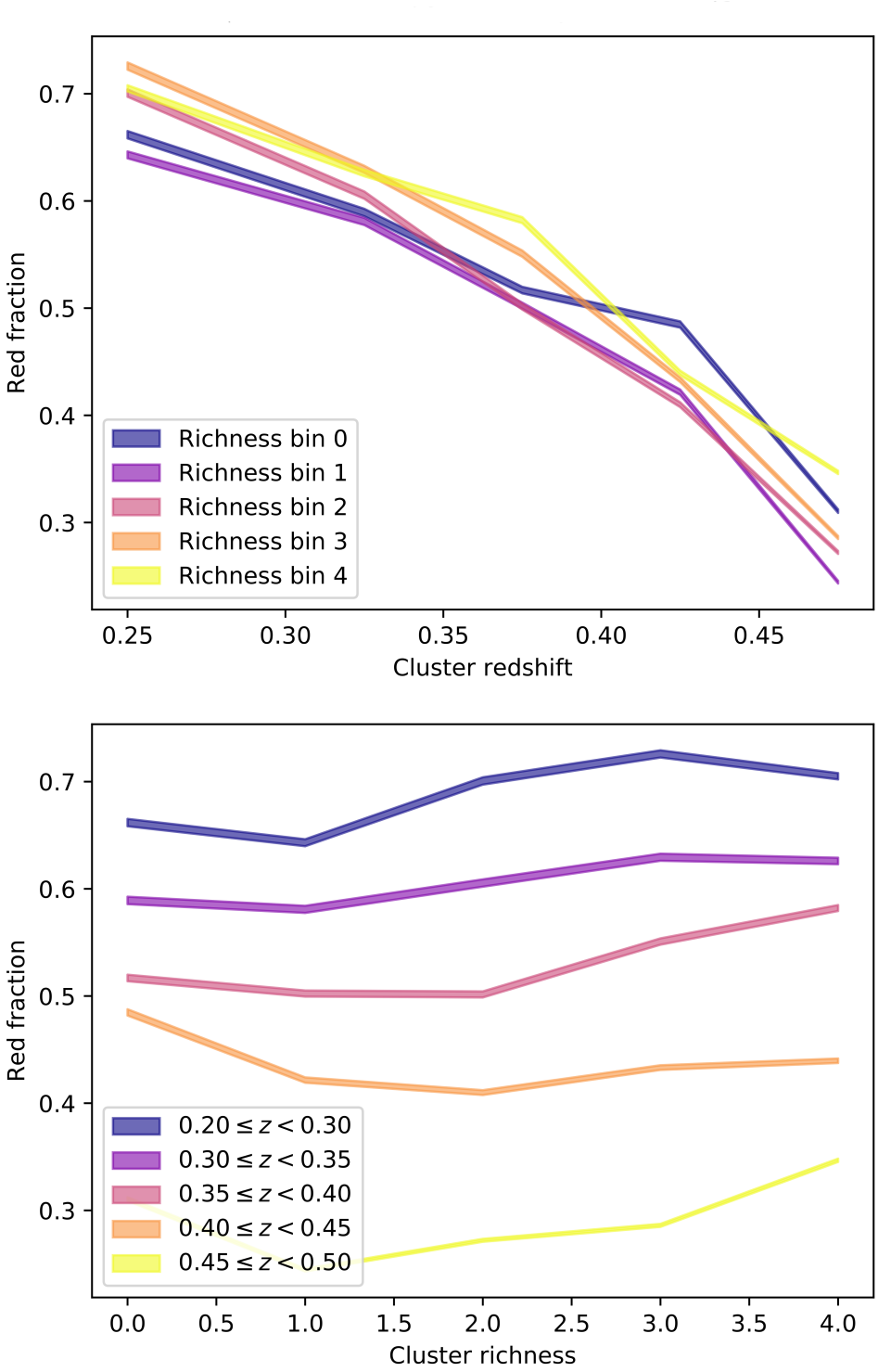

Figure 3.22: Top panel: red fraction as a function of cluster richness for each redshift bin. Bottom panel: red fraction as a function of cluster redshift for each richness bin. For both panels, the width of the lines correspond to the Poissonian-based uncertainty interval.

is sensitive only to the richest of clusters. Hollowood et al. (2019) measure the X-ray temperature of 246 redMaPPer clusters and find that the vast majority of their X-ray temperatures T are in the range 5 keV $\leq T \leq$ 10 keV. Urquhart et al. (2010) calculates blue fraction in galaxy clusters as a function of x-ray temperature and finds that most of the variation in blue fraction occurs at X-ray temperatures $T \lessapprox 5$ keV, below the detection threshold of redMaPPer. We can conclude from our failure to see a strong relationship between red fraction and richness that most quenching occurs in smaller clusters or even groups. By the time galaxies are accreted into clusters as massive and rich as those redMaPPer is sensitive to, they have already experienced so much quenching that we observe clusters "saturated" by quenching.

3.10 Calculating giant-to-dwarf ratio as a function of cluster richness

The first step to calculating GDR was to determine the absolute r-band magnitude which would separate the giants from the dwarfs. While it would have been ideal to adopt the same absolute magnitude for the cutoff between giants and dwarfs as used by De Lucia et al. (2007) and Capozzi et al. (2010), doing so was not the best option because in each redshift bin, the cutoff magnitude would have been fainter than our faint cutoff magnitude used to ensure completeness. De Lucia et al. (2007) and Capozzi et al. (2010) discriminate between giants and dwarfs using the criteria that giants have $M_V < -20$ while dwarfs have $M_V > -20$. To convert from the Johnson V-band filter they use to the SDSS r-band filter, we use the following relation:

$$V = r + 0.44(g - r) - 0.02, \tag{3.8}$$

which is accurate to 0.05 magnitudes (Fukugita et al., 1996). We use the color $g - r = 1.783$, calculated from our model stellar population at the median redshift of our clusters, $z = 0.37$. This yields the corresponding absolute magnitude of $M_r = -20.76$, which we converted to apparent magnitudes using Equation 3.1. For the redshift bins in order from low redshift to high, the respective apparent r-band magnitude for the GDR cutoff would be 20.25, 21.03, 21.48, 21.87, and 22.24 respectively, while the faint apparent r-band magnitude cutoff values were 19.55, 20.33, 20.77, 21.17, and 21.53. Therefore, for every redshift bin, the apparent magnitude which we would use to discriminate between giants and dwarfs in order to mimic the previous literature would be beyond the faint limits of our dataset. We do, however, use the De Lucia et al. (2007) system to re-calculate GDR when comparing to the literature values,

Redshift bin range	Apparent r-band giant-dwarf cutoff magnitude
0.2 - 0.2945	18.87
0.2945 - 0.3538	19.65
0.3538 - 0.3936	20.09
0.3936 - 0.4366	20.49
0.4366 - 0.5	20.85

Table 3.4: Giant-dwarf cutoff apparent r-band magnitudes in each redshift bin.

with notable caveats. See Section 3.11 for details.

Since it was not possible to adopt the same absolute cutoff magnitude as De Lucia et al. (2007) and Capozzi et al. (2010) without sacrificing completeness, we chose to use the absolute magnitude which would put the GDR for our central redshift-richness bin at a value of approximately one, i.e. we performed an internal, relative test. To determine this magnitude, we varied the apparent magnitude at which we split between dwarfs and giants in this bin until the GDR was approximately one. The apparent magnitude we obtained with this method was $r = 20.09$.

Using our model stellar population described in Section 3.1, we solved the cosmological distance modulus given by Equation 3.1 to obtain the corresponding absolute magnitude of $R = -22.12$, assuming the median redshift of this bin. For each redshift bin, we used the cosmological distance again to convert back to apparent magnitudes corresponding to the absolute magnitude of $R = -22.12$, assuming for each bin its median redshift. These calculations resulted in the list of apparent r-band magnitudes used to discriminate between giants and dwarfs in each redshift bin respectively. The results are given in Table 3.4. Figure 3.23 shows our faint cutoff magnitudes and GDR cutoff magnitudes in comparison to those of De Lucia et al. (2007).

The next step for each redshift-richness bin was to determine which of its galaxies should be considered when computing the GDR. We took the height of the normalized red sequence Gaussian profile and subtracted the height of the normalized blue sequence Gaussian profile at the $g - r$ color of each galaxy to get a proxy for the probability that the galaxy in question was a member of the red sequence. For each galaxy, then, we generated a random number from the uniform distribution between 0 and 1 and compared it to the galaxy's probability proxy. If the probability proxy was higher than the random number, the galaxy was considered a member of the red sequence for the purposes of calculating GDR.

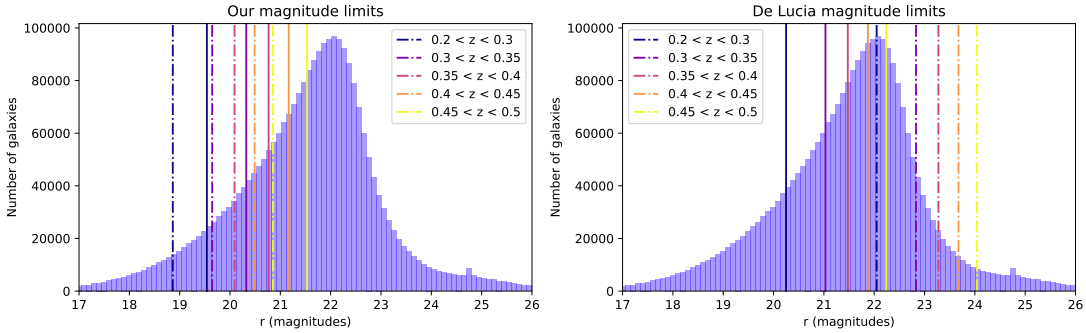

Figure 3.23: Comparison of our faint cutoff magnitudes and GDR cutoff magnitudes with those of De Lucia et al. (2007). Faint apparent magnitude cutoffs (calculated in Section 3.4) are represented by solid lines, and GDR apparent magnitude cutoffs are represented by dash-dotted lines. The distribution of our SDSS cluster-member galaxies with respect to apparent r-band magnitude is plotted to illustrate the issue of photometric incompleteness that is introduced by using De Lucia et al. (2007)'s limits.

Calculating uncertainty

As GDR is a division-based measurement, we can refer to Equation 1.3 and use the standard formulas for uncertainty propagation to calculate the uncertainty δ_{GDR} on the GDR as follows:

$$\delta_{GDR} = GDR\sqrt{\left(\frac{\delta N_{giants}}{N_{giants}}\right)^2 + \left(\frac{\delta N_{dwarfs}}{N_{dwarfs}}\right)^2} \tag{3.9}$$

where N_{giants} is the number of giant galaxies, N_{dwarfs} is the number of dwarf galaxies, and δN_{giants} and δN_{dwarfs} are their respective uncertainties. Calculating δ_{giants} and δ_{dwarfs} requires another standard uncertainty propagation formula, this time for addition since these quantities are sums. For each color-magnitude cell we use when calculating GDR, we can determine what uncertainty it alone will contribute using the Poissonian uncertainty maps produced in Section 3.5.4. We define δN_{giants} and δN_{dwarfs} by

$$\delta N_{giants} = \sqrt{\sum_{i}^{N_{giant\ cells}} \delta g_i^2} \tag{3.10}$$

and

$$\delta N_{dwarfs} = \sqrt{\sum_{i}^{N_{dwarf\ cells}} \delta g_i^2} \tag{3.11}$$

where $N_{giant\ cells}$ is the number of cells containing giant galaxies, $N_{dwarf\ cells}$ is the number of cells containing dwarf galaxies, and δg_i is the individual uncertainty contribution from each color-magnitude cell.

3.11 Giant-to-dwarf ratio measurements

The GDR is an important measurement because it gives us insight into how the red sequence is built up over time- does it begin with small galaxies which merge to create larger ones? Or does it begin with large galaxies which then accrete smaller ones? This question can be answered by considering the relationship between GDR and redshift. Meanwhile, the relationship between GDR and cluster richness can tell us whether the global environment has any effect on the red sequence's composition.

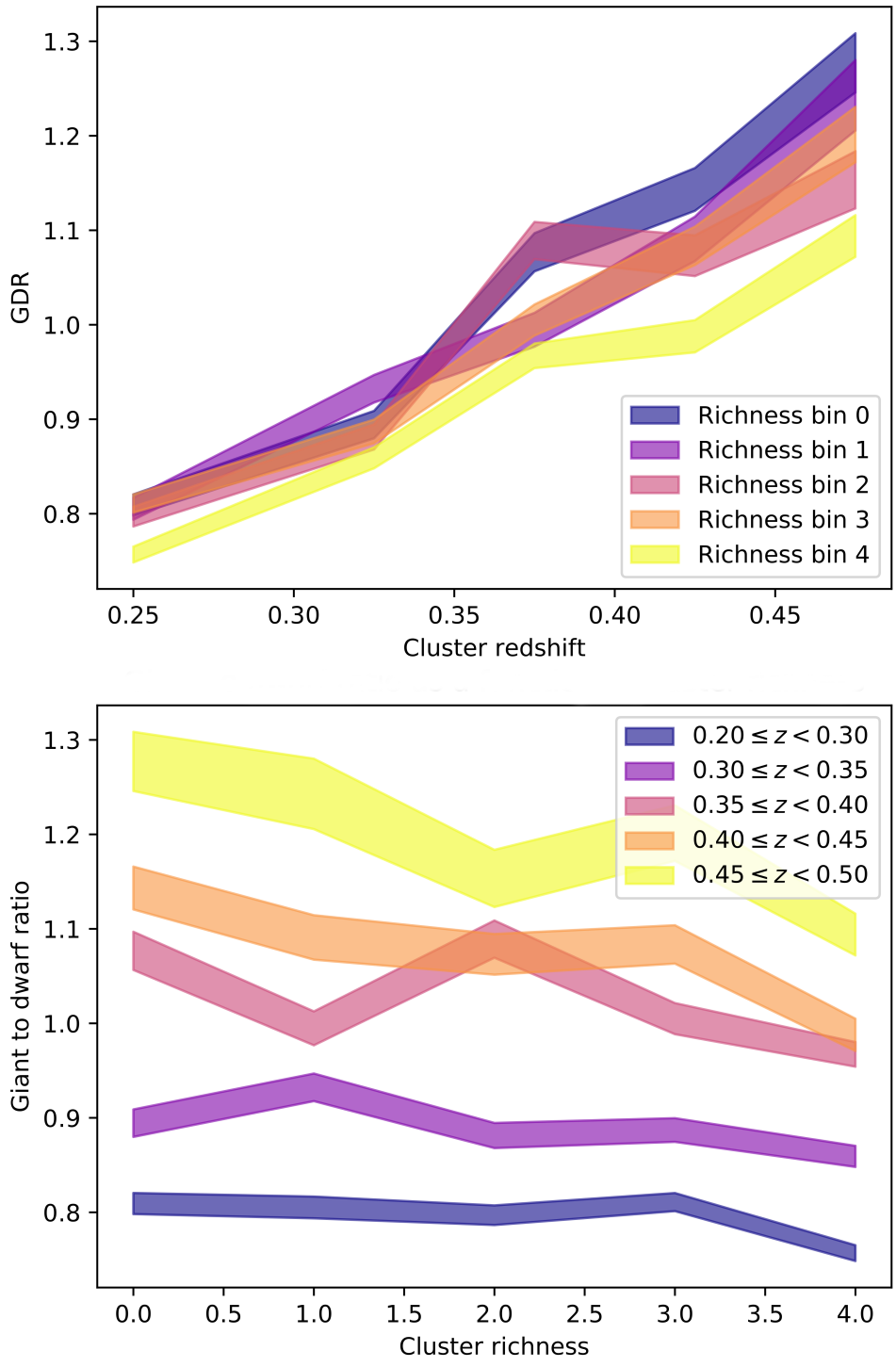

Figure 3.24: Top panel: GDR as a function of cluster redshift for each richness bin. Bottom panel: GDR as a function of cluster richness for each redshift bin. For both panels, the width of the lines correspond to the Poissonian-based uncertainty interval.

3.11.1 Giant-to-dwarf ratio as a function of redshift

The GDR as a function of cluster richness for each redshift bin is shown in the top panel of Figure 3.24. We found that the GDR increases roughly linearly with redshift for all richness bins; that is to say, at higher lookback times, there was a higher number of giant galaxies per dwarf galaxies in the average cluster's red sequence than there is presently. In other words, the faint end of the red sequence becomes more populated as redshift decreases. This phenomenon by which the red sequence begins with massive galaxies and then accretes less massive galaxies is sometimes referred to as "downsizing" in the literature, and it is supported by many including Barkhouse et al. (2007), Stott et al. (2007)), De Lucia et al. (2007), Gilbank & Balogh (2008), Hansen et al. (2009), Lu et al. (2009), and Capozzi et al. (2010) while being contested by Tanaka et al. (2005) and Andreon (2008). Andreon (2008), however, uses only single high-redshift clusters in their measurements rather than the large samples used in other studies (including this one), and so their results may require additional care in interpreting.

Our result is in qualitative agreement with many values from the literature; see Figure 3.25 for a plot of our results (re-calculated to match the absolute magnitudes used by De Lucia et al. (2007) for GDR cutoff and the faint limit as described in Section 3.10) combined with many other results from the literature which use the same magnitude limits. We observe that our data points follow a monotonically increasing trend like the others do, however we are systemically biased toward higher GDRs. This is expected, however, from the fact that our observations are not deep enough to be photometrically complete out to De Lucia et al. (2007)'s faint absolute magnitude limit, as illustrated by Figure 3.23. Therefore, there will naturally seem to be a higher ratio of bright to faint objects than there truly is. This effect will become more pronounced with increasing redshift as the faint limit grows fainter and our sample becomes more incomplete; this explains why our slope is steeper than reported in the literature. We can, however, compare the width of our error bars to the others' and see that while our results may not be accurate when we use the De Lucia et al. (2007) system due to bias, they are much more precise than previous measurements. When we use our own cutoff magnitude system to ensure photometric completeness at all redshifts, then, our results as shown in Figure 3.24 should be not only accurate but also precise.

The trend of GDR increasing with increasing redshifts implies that the red se-

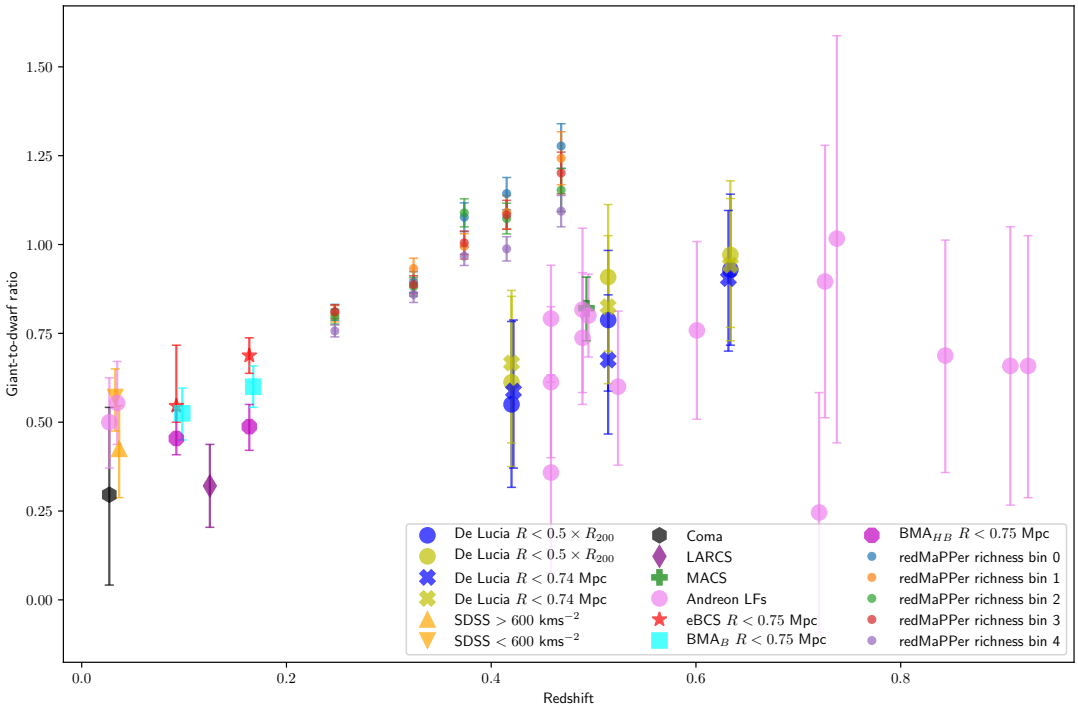

Figure 3.25: Comparison of our giant-to-dwarf ratio versus redshift results with the literature values. Our results are represented by the small dots, with colors corresponding to each richness bin. De Lucia et al. (2007) values: $R < 0.5R_{200}$ (large blue and yellow dots), $R < 0.74$ Mpc (blue and yellow crosses). Blue represents results where cluster members were selected with photometric redshifts, and yellow represents results where cluster members were selected with a statistical approach. SDSS clusters with $\sigma_r > 600$ kms^{-1} (upward facing orange triangle), SDSS clusters with $\sigma_r < 600$ kms^{-1} (downward facing orange triangle). Stott et al. (2007) values: Las Campanas Observatory and Anglo-Australian Telescope Rich Cluster Survey (LARCS; purple diamond), Massive Cluster Survey (MACS; green cross). Andreon (2008) values: large pink dots; note that each of these datapoints represents a single cluster. Lu et al. (2009) and Yang et al. (2007) value: Coma cluster, black pentagon. Capozzi et al. (2010) values:

quence is first populated with luminous, massive galaxies which are quenched by the hostile cluster environment. These galaxies tend to be located at the center of their respective clusters, as dynamical friction works very effectively on massive galaxies to spiral them in toward the center of the gravitational potential well as they fall into a cluster. As the central region of the cluster becomes increasing densely populated with these massive galaxies, it begins to accrete less massive, fainter galaxies as well, and they are also quenched and join the red sequence. This accretion of smaller and smaller galaxies over time is the driver for the trend we see of GDR increasing with redshift. Our results are in agreement with those of Lavoie et al. (2016), who found that in their sample of 100 x-ray selected clusters, BCGs grow primarily via dry mergers with quenched galaxies at $z \lessapprox 1$.

3.11.2 Giant-to-dwarf ratio as a function of cluster richness

We see in the lower panel of Figure 3.24 that there at most only a mild trend between cluster richness and GDR. As a cluster's richness is correlated with its mass, it can be instructive to compare with results from the literature which look for a relationship between a cluster's GDR and its luminosity (another proxy for cluster mass). Capozzi et al. (2010), Andreon (2008), and Gilbank & Balogh (2008) all find that there is no significant evolution in a cluster's GDR with respect to its luminosity, lending credence to the lack of relationship between a cluster's GDR and richness as we observe. However, it is possible that while a the global environment represented by the richness of the cluster has no effect on its GDR, the GDR could vary within the cluster as a result of local environment. For example, GDR could be affected by the relatively dense environment inside the cluster. This possibility will be investigated in Chapter 4).

3.12 Summary of implications for galaxy evolution

Synthesizing our results for the evolution of GDR and red fraction with respect to redshift and cluster richness, we can glean some insight to the story of galaxy evolution within clusters. Referring back to Figure 1.7, we recall that the red fraction gives us information about quenching, the process that moves galaxies from the blue cloud into the red sequence. Our analysis of SDSS galaxies within redMaPPer clusters shows that red fraction decreases notably with redshift, while there is little to no relation between red fraction and cluster richness.

The inverse relation between red fraction and redshift implies that as the universe ages, clusters become redder and redder as their member galaxies are quenched and move from the blue cloud to the red sequence. This trend is well-studied and is known as the Butcher-Oemler effect. Reproducing this widely-accepted result lends credibility to the other measurements made in this thesis.

The lack of relationship between red fraction and cluster richness is debated in the literature; many studies have been made, but most face the issue of either low sample size or sensitivity to a small range of richnesses. We observe no relation, which implies that the global environment in which a galaxy lies has either very little or no effect on the rate at which its star formation will be extinguished. The question remains, though, whether the local environment within the cluster has any effect on galaxies' degree of quenching; this topic will be explored in the following chapter.

GDR, on the other hand, is controlled by the dry mergers of already extinguished galaxies and is the process by which the red sequence accumulates over time. The GDR gives us insight into how galaxies already on the red sequence become more luminous, moving leftward on the cartoon CMD in Figure 1.7.

We observe that GDR increases significantly with redshift. The relation between GDR and redshift supports a top-down paradigm called downsizing for the buildup of the red sequence, where it begins with the brightest and most massive galaxies which are quickly quenched through internal mechanisms such as AGN and supernovae winds. These massive, quenched galaxies then accrete less massive galaxies which are less affected by internal quenching, but are quenched through external mechanisms associated with the dense environment of the cluster, such as mergers, harassment, and ram pressure stripping (see Section 1.5).

Finally, our failure to observe a relation between GDR and cluster richness suggests that the GDR of a cluster is not affected by its overall richness, at least at the high levels of richness redMaPPer is sensitive to. As discussed in Section 3.11, though, it is likely that richness does affect GDR on smaller richness scales.

Chapter 4

Investigating the effects of local environment on galaxy evolution in clusters

For this portion of the analysis, we will switch focus from investigating the effects of a global environmental factor - cluster richness - and instead looked at the changes in the galaxy population with respect to each individual cluster member galaxy's distance d_{BCG} from its corresponding BCG, as well as σ_5, a density measurement which is sensitive to clumps within the cluster as well as the smooth radial changes in density. This shift in focus was motivated by the results in the previous chapter which showed that the global environment within a cluster, represented by its richness, could not account for all of the variation in the red fraction or GDR exhibited by its member galaxies. This prompted the question of whether the local environment within a cluster (such as clumps within the cluster or the increase in density with decreasing cluster-centric radius) plays a more significant role. We split our sample of clusters into σ_5, d_{BCG}, and z bins so as to disentangle the effects of each on red fraction and GDR.

We begin with a description of how cluster member galaxies were selected, detail our process for calculating d_{BCG} and σ_5, and provide results for GDR and red fraction and a discussion of their implications for galaxy evolution. Figure 4.1 is a flowchart which gives an overview of the steps taken in this chapter.

4.1 Selecting cluster member galaxies

The focus on local environment requires a more computationally expensive cluster-by-cluster approach which we were able to avoid in the previous chapter by stacking related clusters into bins before performing the analysis. To calculate d_{BCG}, though, requires identifying the exact member galaxies of each individual cluster. For each

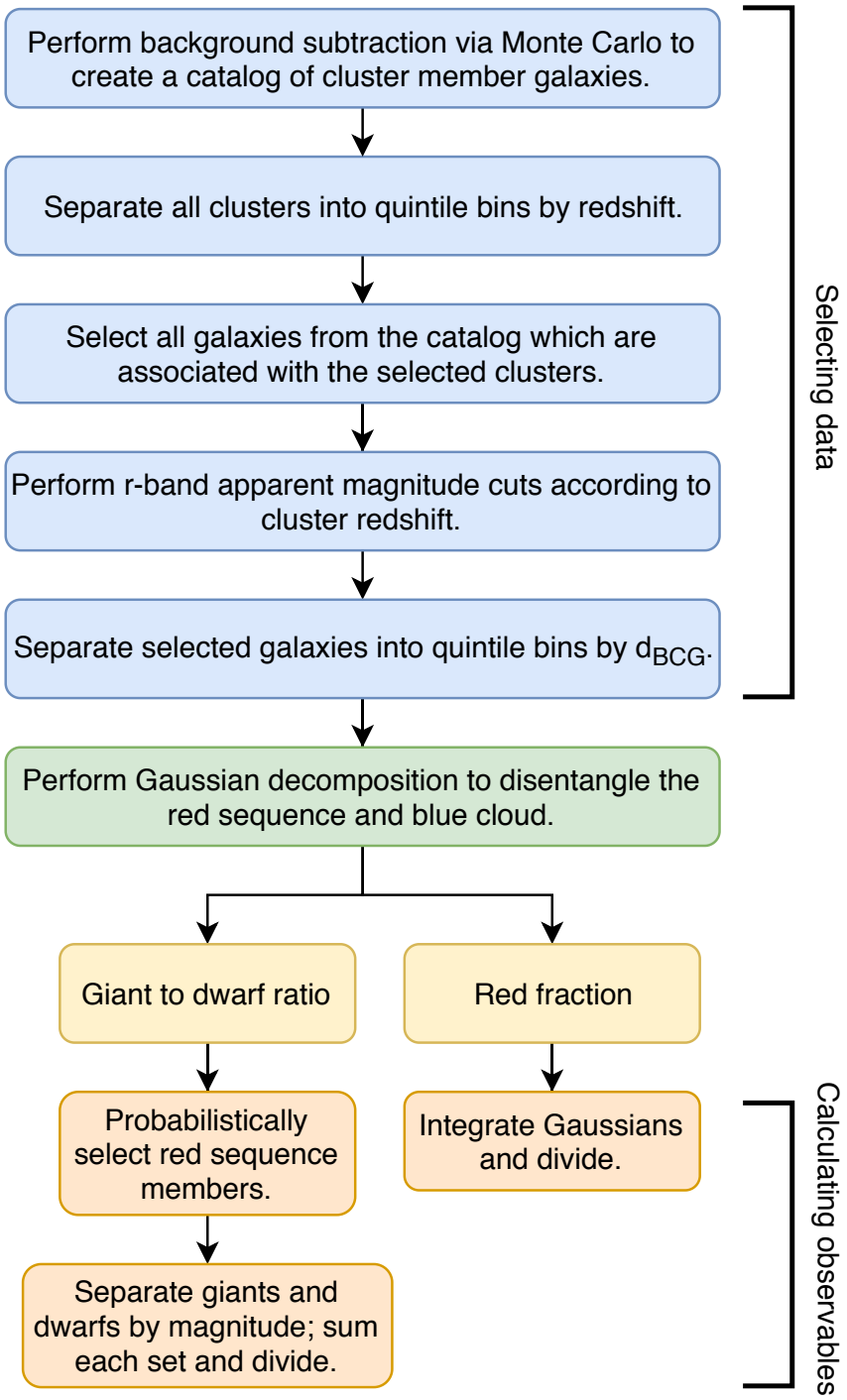

Figure 4.1: Flowchart of steps taken in Chapter 4.

cluster, we began with all of the SDSS galaxies within 1 Mpc of the BCG presented by redMaPPer.

As we were now working on a cluster-by-cluster basis and there was no need to group clusters by redshift bin, we determined the angular radius corresponding to 1 Mpc as a function of each cluster's redshift as reported by redMaPPer. We then performed the following steps in order to obtain a catalog of cluster member galaxies.

4.1.1 Applying magnitude cuts

In the previous chapter, we used redshift bins when applying magnitude cuts to account for survey completeness. The focus on local environment made the binned approach unnecessary; instead, we determined an appropriate faint r-band cutoff magnitude for each cluster by interpolating our results for cutoff magnitude vs. redshift shown in Figure 3.7. For a review of how these cutoff magnitudes were first calculated, see Section 3.4.

4.1.2 Background subtraction via Monte Carlo sampling

Since we were no longer taking the binned statistical background subtraction approach used in the previous chapter, an alternate method was needed to perform background subtraction for a single cluster at a time. We took a Monte Carlo approach in which a selection of member galaxies were chosen probabilistically for each cluster. For each galaxy left in the cluster aperture after applying the magnitude cuts from the previous section, we determined its probability of not being a cluster member but part of the filed. To define the probability p(member) of the galaxy being a member of the field, we use the following relation (e.g. Pimbblet et al., 2002; Urquhart et al., 2010):

$$p(\text{field}|N_{c+f}, N_f) = \frac{N_f}{N_{c+f}} \tag{4.1}$$

where N_{c+f} represents the number of cluster aperture galaxies (pre-background subtraction) and N_f represents the number of field galaxies in a given colour-magnitude bin. These color-magnitude bins come from CMDs created for the cluster and field apertures as in Section 3.5.1. The only difference in how the CMDs were created this time is that the cluster CMD represents the galaxies from only a single cluster, and the background population is scaled before creating the CMD such that is repre-

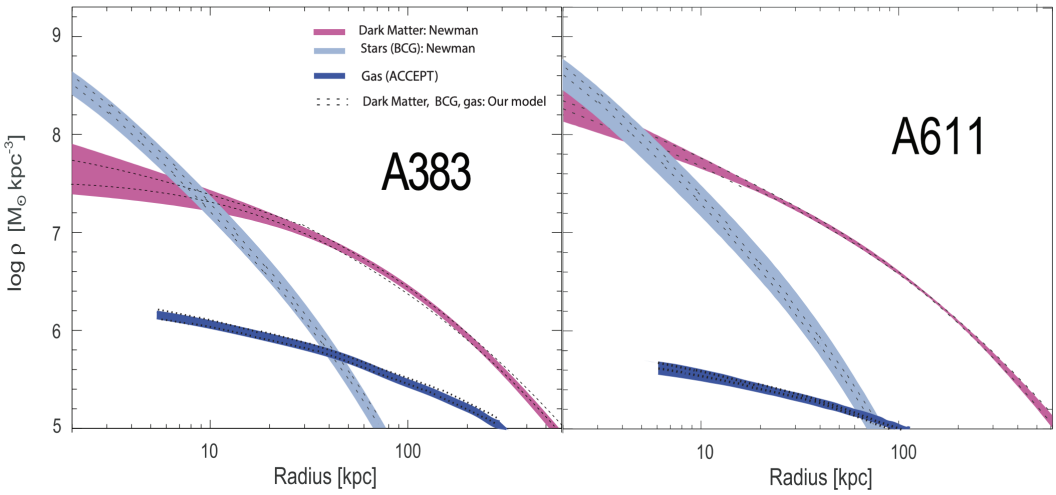

Figure 4.2: Mass density profiles for the galaxy clusters A383 and A611. The magenta curves represent the clusters' dark matter components, the light blue curves represent their stellar components, and the dark blue curves represent the gaseous components (the ICM). Note how the mass density decreases smoothly as the radius increases. These are X-ray detected CLASH galaxy clusters which have high-quality weak- and strong-lensing measurements from the Subaru and Hubble Space Telescopes. Figure from Del Popolo et al. (2019).

sents the same angular area as covered by the cluster in question (following the same process as the areal scaling described in Section 3.5).

For each galaxy in a given cluster aperture, we used its $g - r$ color and its r-band magnitude to place it in one of the color-magnitude bins and determine its probability of being a member of the field. We then chose a random number from the uniform distribution between 0 and 1. If this number was greater than the galaxy's probability of being a field member, the galaxy was selected as a cluster member, and if not, it was ignored.

4.2 Calculating d_{BCG}

Galaxy clusters are densest in their centers and smoothly decrease in density with increasing radius (Del Popolo et al., 2019); see Figure 4.2 for typical mass density profiles within galaxy clusters, separated into the dark matter, stellar, and gas components.

For this reason, we can expect that if local density affects red fraction and GDR, then we should also observe a trend in red fraction and GDR versus cluster-centric

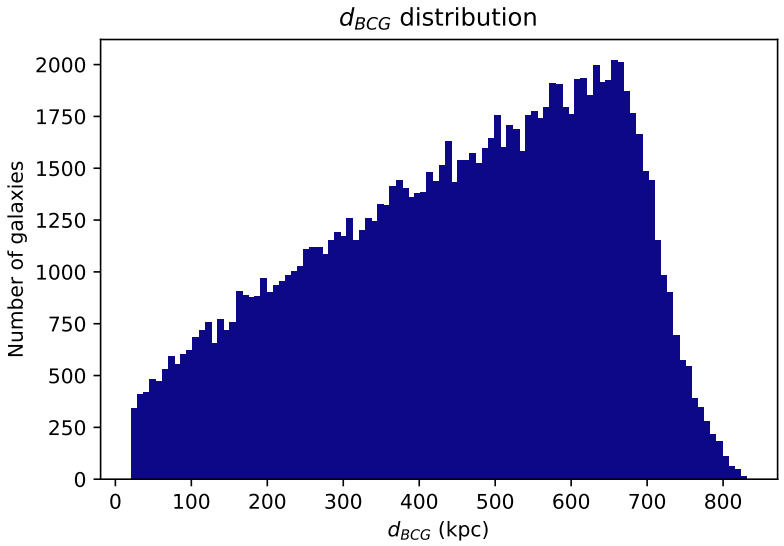

Figure 4.3: Distribution of d_{BCG} for all cluster member galaxies.

radius. This distance d_{BCG} was computed for each cluster member galaxy as the 2D projected distance between it and the BCG of its host cluster. There are several ways of estimating the centroid of a cluster indicated in the literature, but the only one we have access to is the BCG. In relaxed clusters, the BCG is a reliable indicator for the deepest point in the cluster's gravitational potential well.

The coordinates of the BCG were obtained from redMaPPer , and the coordinates of the cluster member galaxies were obtained from SDSS. For each galaxy, we used Astropy's `match_coordinates_sky` function to obtain its angular separation from its host cluster's BCG, and then we used WMAP9 cosmology and Astropy's `kpc_proper_per_arcmin` to convert the angular separation to a projected physical separation in kpc, assuming that the cluster member galaxy in question had the same redshift as redMaPPer reported for its corresponding cluster (Robitaille et al., 2013; Price-Whelan et al., 2018). The BCGs themselves are not included in the data for this chapter, as d_{BCG} is meaningless for them. The distribution of d_5 values that we obtained is shown in Figure 4.3.

4.3 Calculating σ_5

Once a catalog of member galaxies was compiled for each cluster, we were able to compute σ_5 for each of these galaxies. σ_5 is a two-dimensional number density measurement defined as

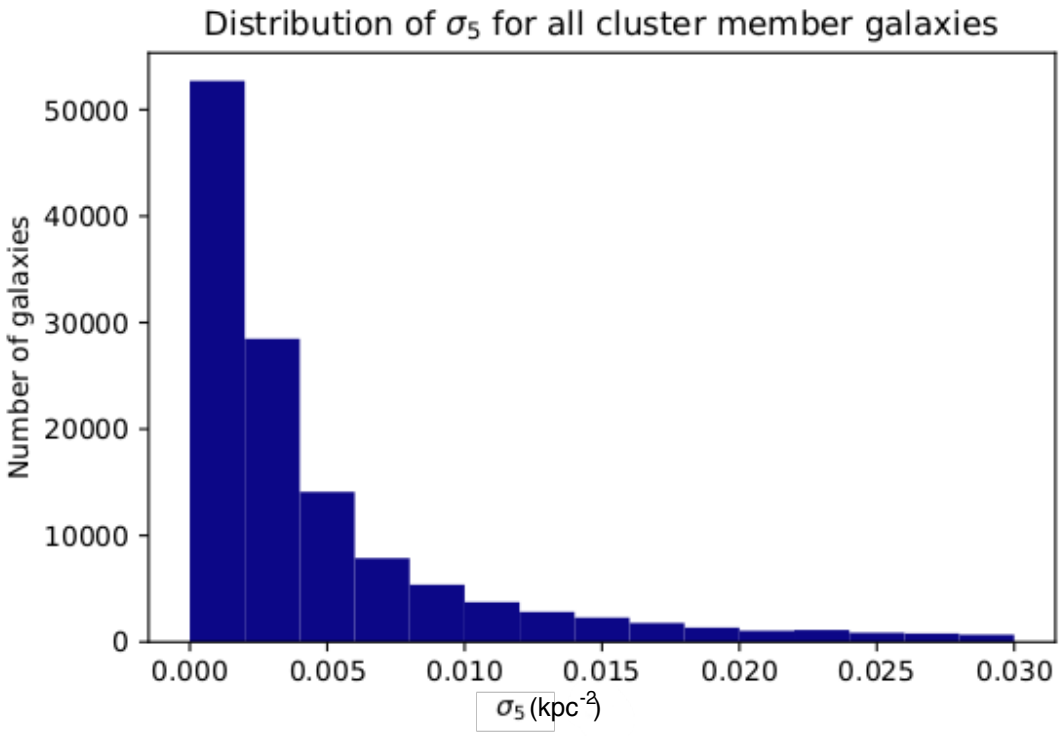

Figure 4.4: Distribution of cluster member galaxies' d_5 values.

$$\sigma_{5,i} = \frac{5}{\pi d_{5,i}^2} \tag{4.2}$$

where d_5 is the projected distance between a cluster member galaxy i and its fifth nearest neighbor galaxy within the cluster.

We used the method described in the previous section to find the distance d_5 between each cluster member galaxy and its fifth nearest neighbor within the same cluster. Figure 4.4 shows the distribution of d_5 values we calculated. We used these results to evaluate Equation 4.2 and determine the density σ_5 associated with each cluster member galaxy in units of kpc^{-2}.

A contour plot of the cluster member galaxies in redshift-σ_5 space as well as in cluster richness λ-σ_5 is shown in Figure 4.5. We also performed a sanity check by plotting the 2-dimensional histogram for σ_5 and d_{BCG}, as shown in Figure 4.6. As expected, we see that as density increases at smaller radii, σ_5 increases. The near-linear relation between the two implies that σ_5 and d_{BCG} should hold very similar information about red fraction and GDR; indeed, we performed the full analysis using both, and found nearly identical results. For the sake of brevity, we will focus only

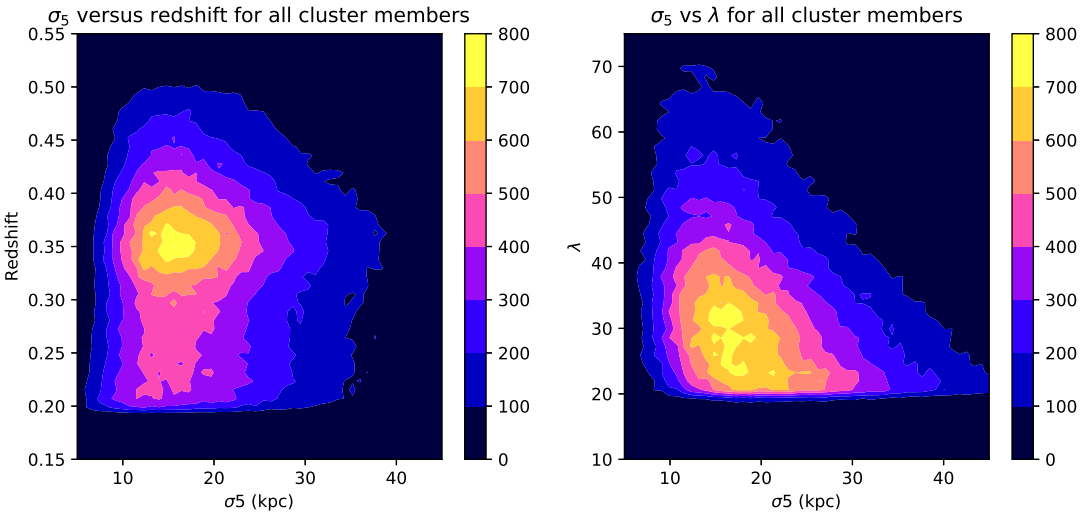

Figure 4.5: Top panel: a contour plot of cluster member galaxies in redshift-σ_5 space. The color bar values represent the number of galaxies within a cell on the plot. Bottom panel: the same, only in cluster richness λ-σ_5 space.

on d_{BCG} in this document.

4.4 Red fraction as a function of redshift

The Monte Carlo-based equivalent of Figure 3.18 which shows the decomposition of red sequence and blue cloud as a function of redshift and d_{BCG} is shown in Figure 4.7. Red fraction as a function of redshift for each σ_5 bin is shown in the top panel of Figure 4.8. We observe that, as in the previous chapter, red fraction decreases with increasing redshift. This is encouraging, as we see that our choice of background-subtraction method does not affect the trend. As discussed in Section 3.9, the inverse relationship between red fraction and redshift is intuitive as it shows that galaxies in clusters become redder with time.

4.5 Red fraction as a function of d_{BCG}

Of more interest is the bottom panel of Figure 4.8, which shows the red fraction as a function of d_{BCG} for clusters grouped by redshift. There is a notable, nonlinear, inverse relationship between red fraction and d_{BCG}. Near the edge of clusters, it appears that galaxies are very rapidly quenched. As the galaxies spiral in toward the centroid of their clusters, quenching quickly becomes saturated so that effectively all

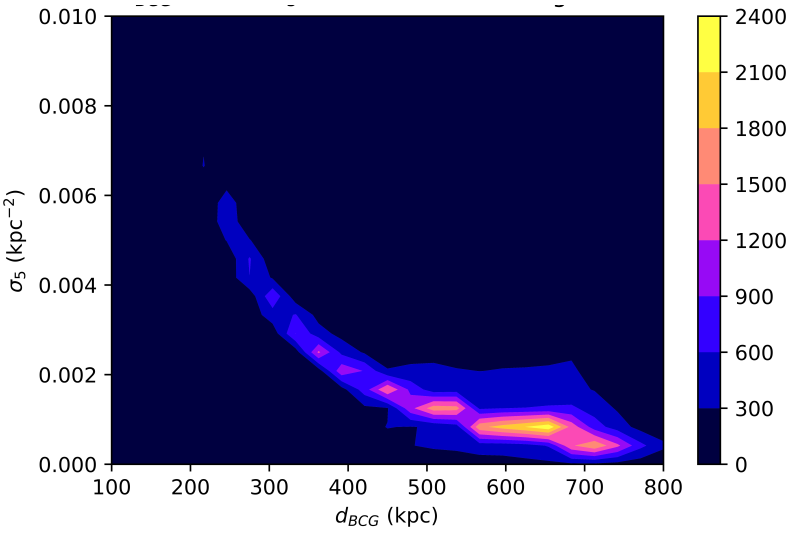

Figure 4.6: σ_5 versus d_{BCG} contour plot. As expected, we see that as density increases at smaller radii, σ_5 increases.

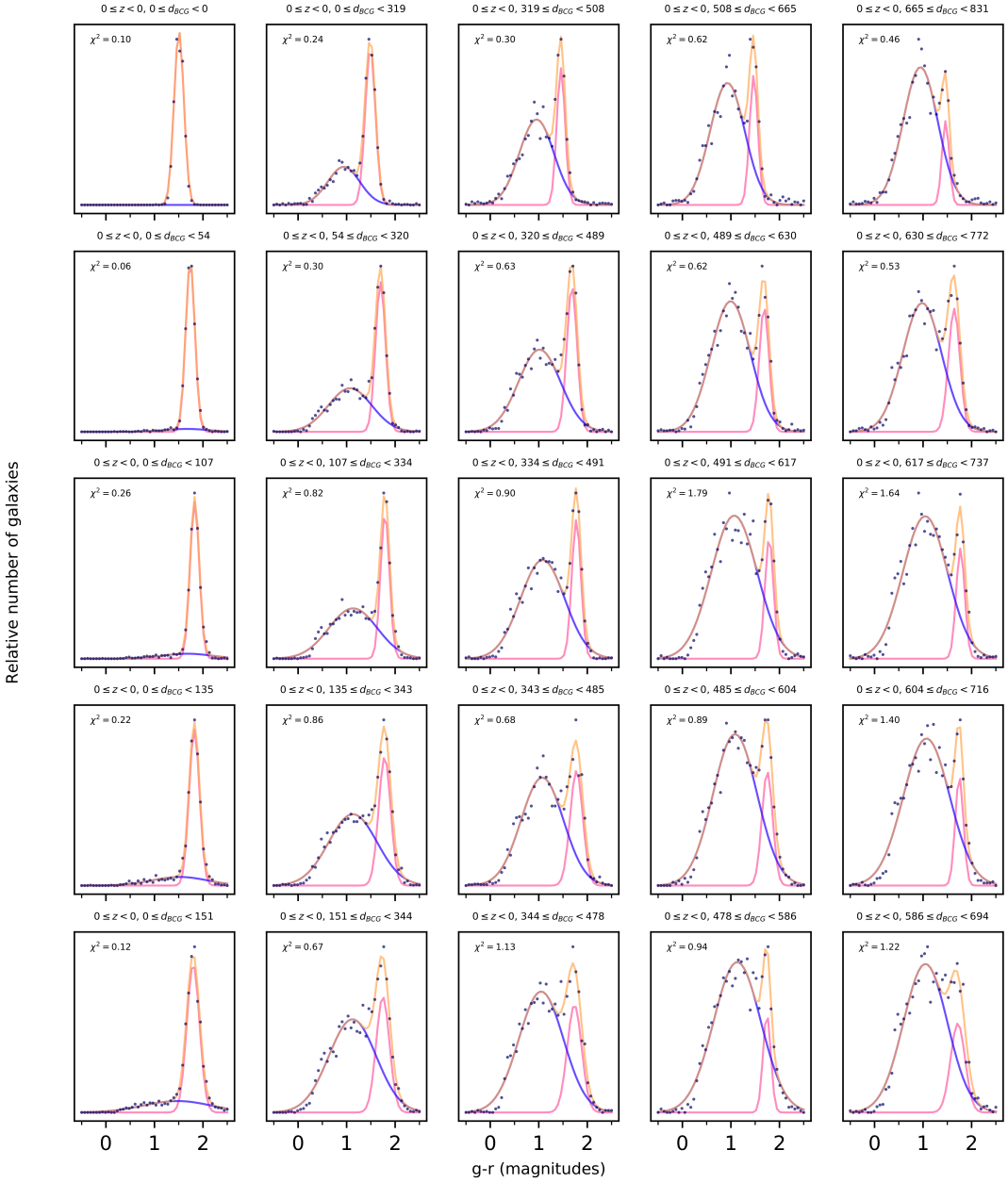

Figure 4.7: Color histogram for red sequence and blue cloud decomposition. The dark blue points here are the galaxies remaining after the Monte Carlo background subtraction. The pink and blue curves represent the fitted red sequence and blue cloud respectively. To visually check the goodness-of-fit, the sum of the red sequence and blue cloud curves is plotted in orange.

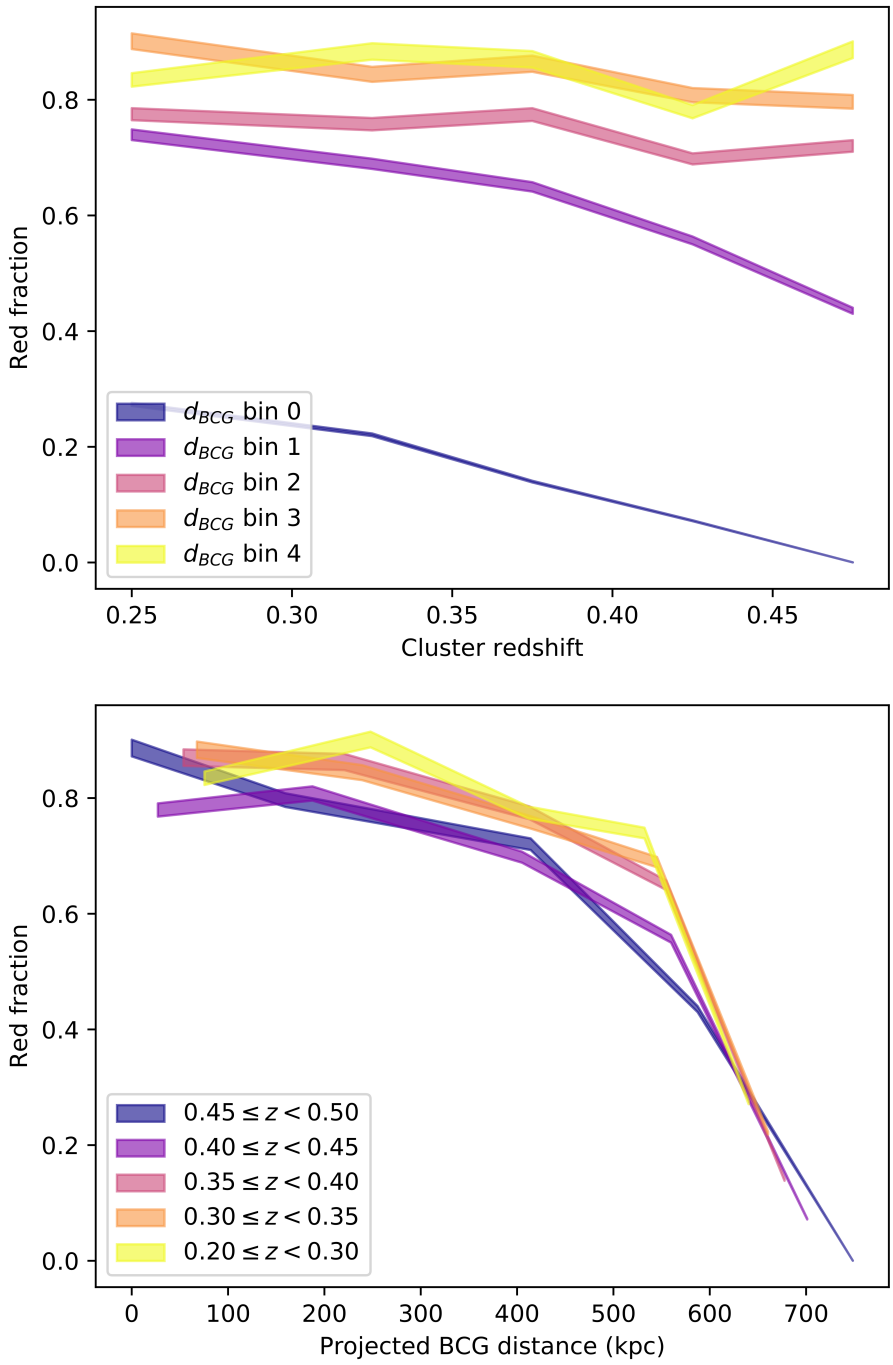

Figure 4.8: Top panel: red fraction as a function of redshift for each d_{BCG} bin. Note that d_{BCG} bin 0 refers to galaxies closest to their associated BCG and d_{BCG} bin 4 refers to those farthest away from their BCG. Bottom panel: red fraction as a function of d_{BCG} for each redshift bin. For both panels, the width of the lines correspond to the Poissonian-based uncertainty interval.

of the galaxies within the inner regions of clusters are quenched. The speed with which galaxies are quenched upon entering a cluster suggests that at least for the richest of clusters (the ones redMaPPEr is sensitive to) within our admittedly limited redshift window, a fast-acting quenching mechanism must be dominant. Ram pressure stripping in particular seems likely, as galaxies encounter the ICM immediately upon entering clusters, and so they experience the quenching effects of ram pressure stripping immediately. While other mechanisms such as an increased rate mergers and harassment within clusters are likely also at play, their effects seem to be more subdued. Consider that if at any moment, the likelihood of a galaxy experiencing a merger is some value depending on the density of the environment. While this likelihood would increase as the galaxy approaches the cluster's centroid, at every timestep we can consider the possible event of a merger or harassment to be independent of previous timesteps. This means that the red fraction would increase when approaching the cluster from the field, but not nearly as suddenly as we observe.

Our results are in agreement with Wake et al. (2005) who calculate the blue fraction in 12 X-ray selected clusters as a function of cluster-centric radius d_{BCG}, normalized by virial radius. Like several other authors (Butcher & Oemler, 1984; Abraham et al., 1996; Fairley et al., 2002; Kodama & Bower, 2001, e.g), they find that blue fraction increases with increasing cluster-centric radius. A direct comparison with our results is not possible because we do not have knowledge of each cluster's virial radius (discussed in further detail in Chapter 5.2), but these results are in qualitative agreement with ours.

An interesting aspect of our results is the manner in which red fraction steeply climbs on the outer edges of clusters and then quickly plateaus within the clusters' inner regions. This suggests that quenching must occur almost immediately after galaxies pass a certain threshold when falling into a cluster. Ram pressure stripping is a likely candidate for the cause of this quenching (at least for clusters within our limited redshift and richness ranges), as galaxies will invariably make contact with a cluster's ICM upon entering. Events like mergers and harassment, while more likely to occur in dense environments like clusters, are not guaranteed to occur when a galaxy falls into a cluster. If these were the dominant quenching mechanisms, red fraction would increase more gradually approaching the clusters' cores.

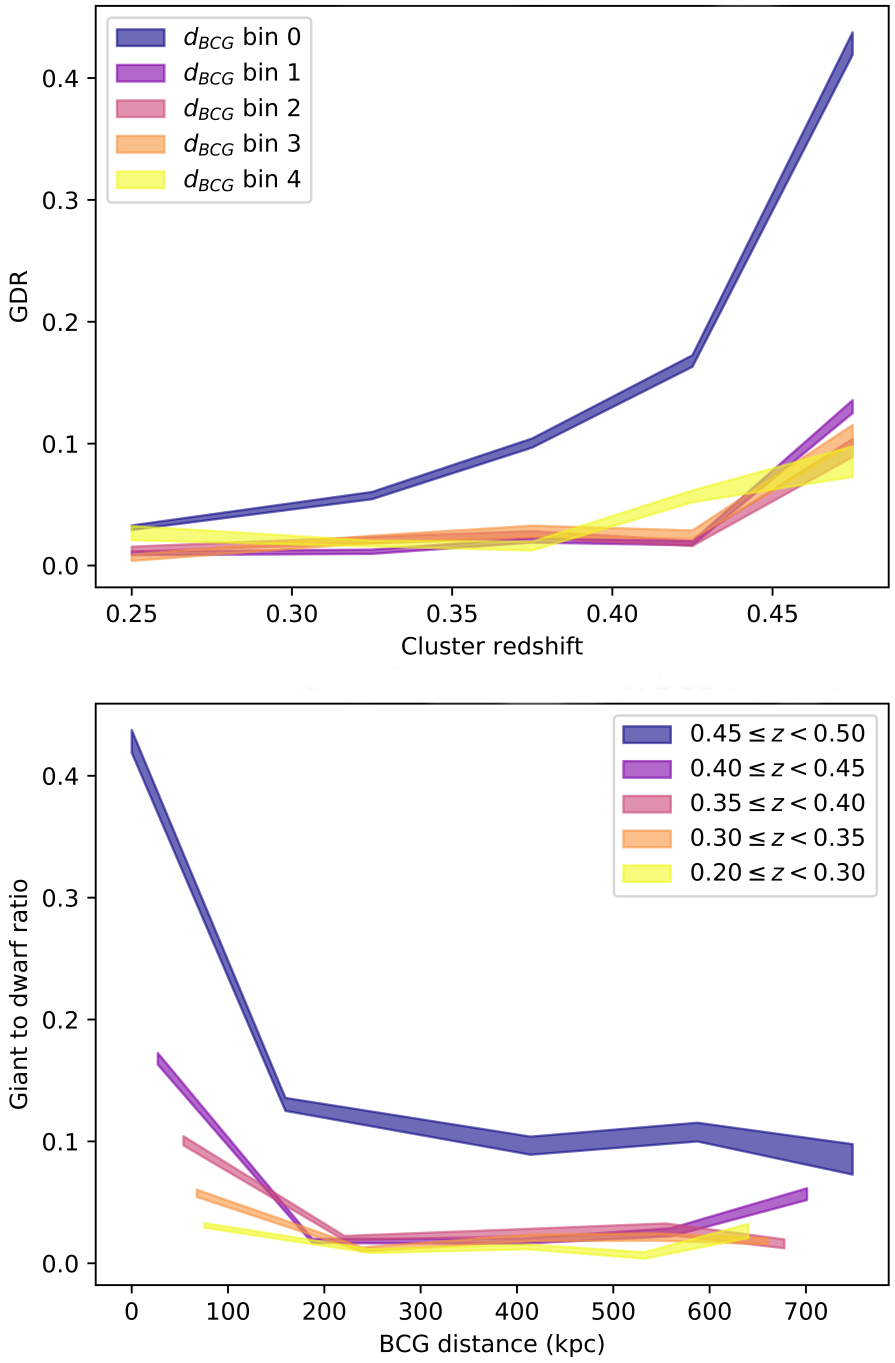

Figure 4.9: Top panel: GDR as a function of cluster redshift for each d_{BCG} bin. Note that d_{BCG} bin 0 refers to galaxies closest to their associated BCG and d_{BCG} bin 4 refers to those farthest away from their BCG. Bottom panel: GDR as a function of d_{BCG} for each redshift bin. For both panels, the width of the lines correspond to the Poissonian-based uncertainty interval.

4.6 Giant-to-dwarf ratio as a function of redshift

The GDR as a function of redshift for each d_{BCG} bin is shown in the top panel of Figure 4.9. As in the previous chapter, we observe that the GDR increases with redshift, implying that the red sequence was first populated by giant galaxies which were later joined by their fainter dwarf counterparts in the process known as downsizing (e.g. Barkhouse et al., 2007; Stott et al., 2007; De Lucia et al., 2007; Gilbank & Balogh, 2008; Hansen et al., 2009; Lu et al., 2009; Capozzi et al., 2010). We notice that this trend is most pronounced for d_{BCG} bin 0, defined as the 20% of galaxies in each cluster aperture closest to the BCG. This suggests that at early times in the universe's history, the typical cluster's red sequence was composed primarily of giant galaxies which lay extremely close to the cluster's BCG.

Figure 4.10 shows the distribution of apparent r-band magnitudes of galaxies within the red sequence, separated by redshift and d_{BCG}. The apparent magnitude range of the histograms varies with redshift bin in order to maintain consistent bright and faint absolute magnitude cutoffs. For comparison, we show De Lucia et al. (2007)'s versions of these histograms in Figure 4.11. A direct comparison would be difficult to interpret as they used I-band photometry while we used r-band photometry, and their redshift range spans $0.4 \leq z \leq 0.8$ while ours spans $0.2 \leq z \leq 0.5$. However, we can observe that De Lucia et al. (2007)'s observations are deep enough to see the "elbow" in the luminosity function at M^*, and while ours are not, both sets of analysis have identified the trend of GDR increasing with decreasing cluster-centric radius.

4.7 Giant-to-dwarf ratio as a function of d_{BCG}

The GDR as a function of d_{BCG} for each redshift bin is shown in the bottom panel of Figure 4.9. We observe that the GDR peaks significantly in proximity to the BCG, drops sharply approaching a distance of 200 kpc, and then more or less plateaus. This is the case in all redshift bins, but the effect is most pronounced at high redshifts. Figure 4.10 supports the difference between galaxies very near the BCG versus galaxies farther away; we observe that for all redshift bins, the smallest d_{BCG} bin displays a "turnover", while the galaxies in bins representing a greater distance from the BCG do not. Note also that while we began with an equal number of galaxies in each d_{BCG}-z bin, but for the GDR calculations we are only considering the number of galaxies which are identified as red sequence members. As demonstrated by our

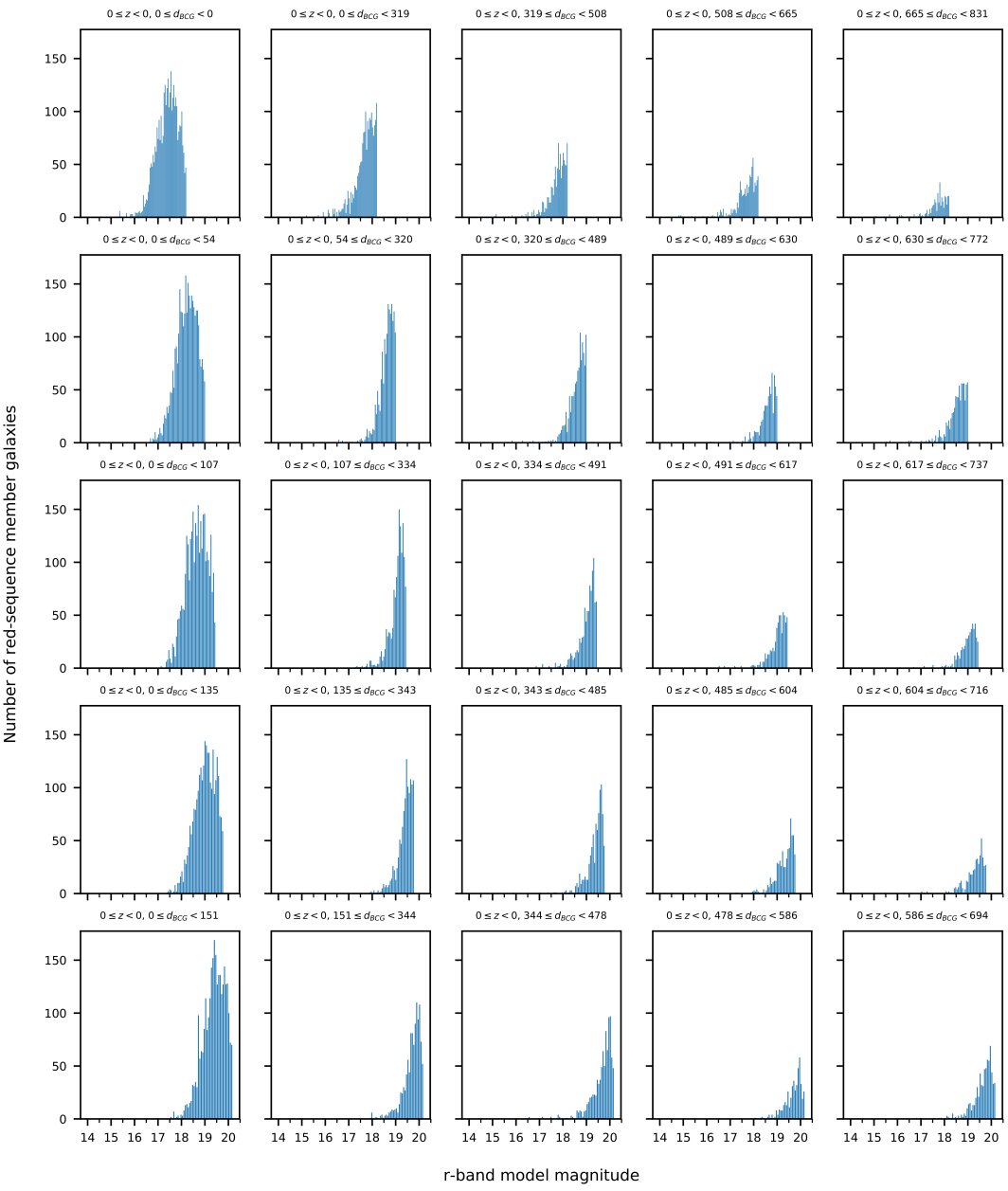

Figure 4.10: Histogram of r-magnitudes for red sequence members from all clusters as a function of d_{BCG} and redshift.

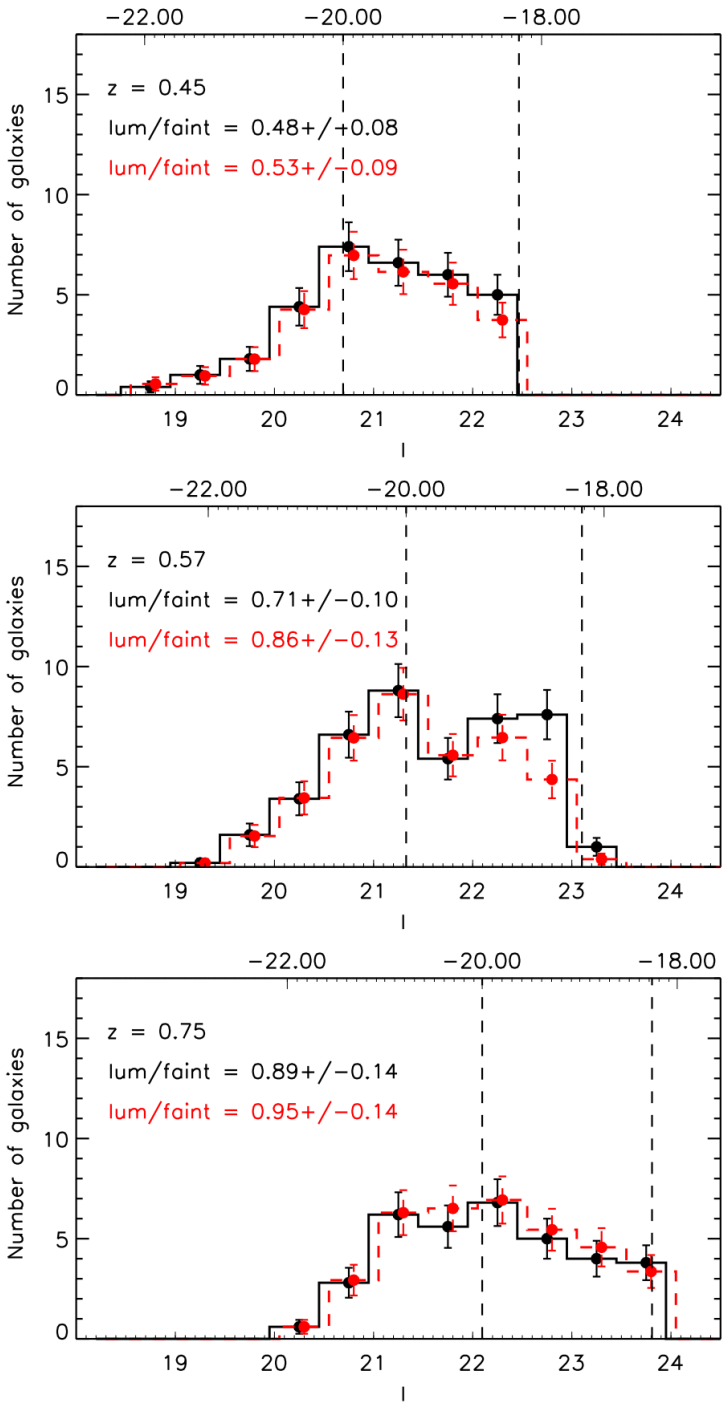

Figure 4.11: Histogram of I-band magnitudes for De Lucia et al. (2007)'s sample of red sequence member galaxies. Black represent cluster members chosen by photometric redshift, and red represents cluster members chosen by statistical subtraction. Each panel represents a redshift bin. The scale on the top of each panel shows the rest-frame V-band magnitude which corresponds to the I-band magnitude. The faint magnitude limit and the GDR cutoff magnitude for each panel are represented by vertical dashed lines. Image credit: De Lucia et al. (2007).

results for red fraction as a function of redshift and d_{BCG} (see Figure 4.8), the number of galaxies within the red sequence varies considerably with redshift and particularly with d_{BCG}.

Figure 4.12 from Barkhouse et al. (2007) shows how M^*[1] becomes brighter with cluster-centric radius d_{BCG} in both the red and blue populations of their sample of 57 galaxy clusters; this is equivalent to the GDR decreasing with cluster-centric radius. Tanaka et al. (2005)'s results are also in agreement with ours; they group their sample of 41695 galaxies into cluster, group, and field environments and observe that the GDR increases as the density increases.

Our results tell the story of bright, massive galaxies falling into clusters at high redshifts and quickly being quenched, as dynamical friction is more effective on massive galaxies and they quickly spiral in to the densest regions in the core of the cluster. As time progresses and redshift increases, the clusters begin to accrete smaller and fainter galaxies, building up the red sequence as they are quenched. This process continues until we observe the clusters as they are today.

4.8 Summary of implications for galaxy evolution

To summarize the results from this chapter, we found that both the red fraction and the GDR are significantly higher in the center of a cluster than at its edges. For red fraction, the sharp increase when approaching a cluster's core suggests that galaxies are very quickly quenched upon entering a cluster environment. Ram pressure stripping is likely to be in effect. For GDR, our results mean that the brightest, most massive galaxies in a cluster are preferentially concentrated toward the centroid. Again, this is intuitive given that dynamical friction is more effective for more massive galaxies, so they will be relatively quick to spiral in towards the center of a gravitational potential well compared to less massive galaxies.

[1] M^* is defined as the turnover or "elbow" magnitude at which the Schechter function (luminosity function of a galaxy cluster; see Section 1.8.2) hinges. For example, in Figure 1.8, M^* would be approximately $M_b - 5\log_{10} h = -22$.

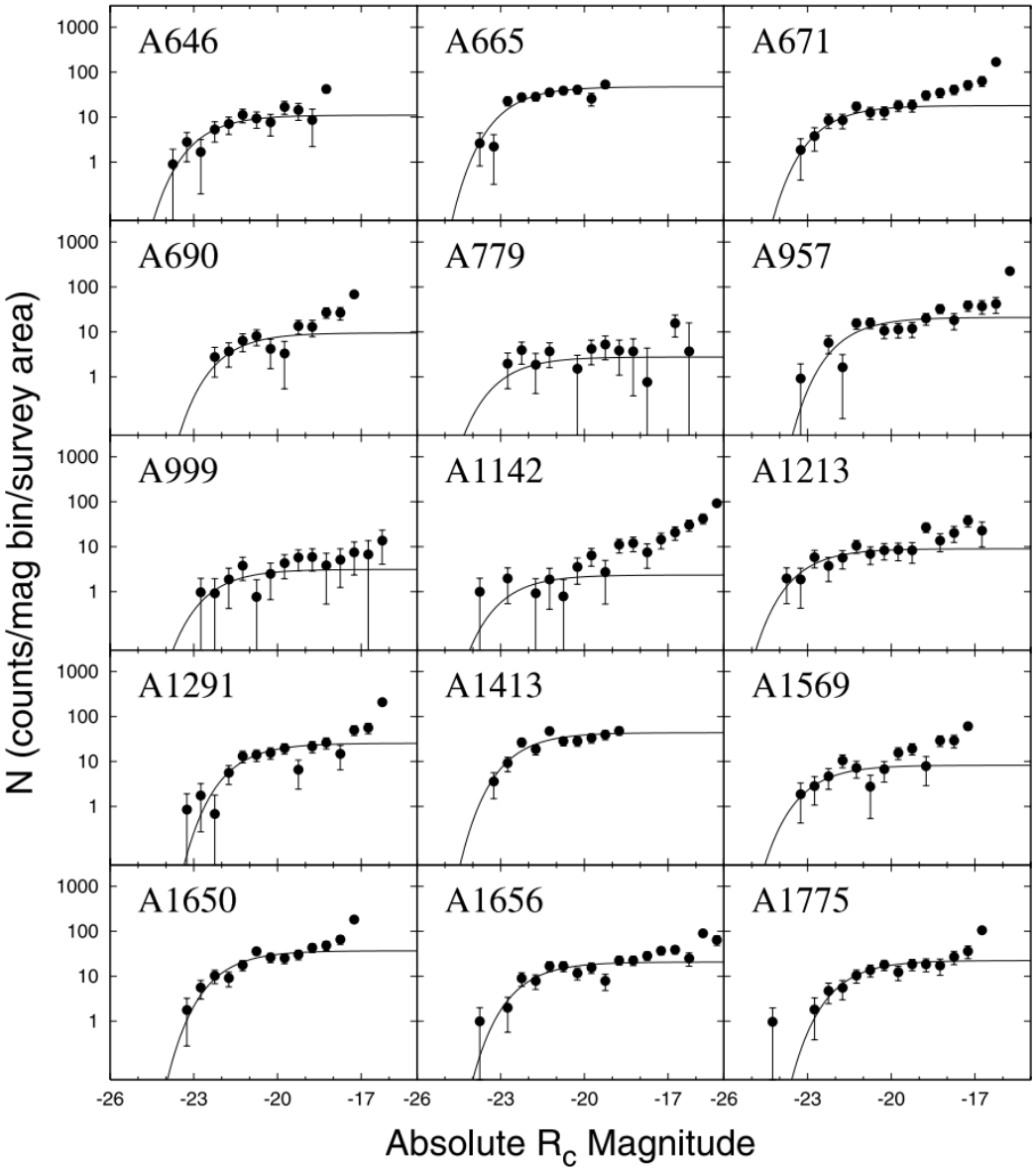

Figure 4.12: Luminosity functions for a subsample of Barkhouse et al. (2007)'s 57 clusters. Black points represent galaxies within a cluster-centric radius $d_{BCG} \leq 0.4$. BCGs are omitted from the data set. Solid lines represent the best-fitting Schechter function. Image credit: Barkhouse et al. (2007).

Chapter 5

Conclusion

5.1 Summary of results

We can summarize our results by observing the effects of redshift, cluster richness λ, and cluster-centric distance d_{BCG} on red fraction and GDR, and then considering their implications for galaxy evolution. Below is a list of our main conclusions:

Let's begin by considering the effects of redshift on red fraction. The top panels of Figures 3.22 and 4.8 illustrate a clear trend in which the red fraction within redMaPPer clusters decreases with redshift. This is intuitive given our understanding of the way stars move around the Hertzprung-Russel diagram (see Figure 1.6); bright, blue galaxies evolve more quickly than their fainter, redder counterparts. As the universe ages, the stellar populations within galaxies age as well, and passive stellar evolution makes the typical galaxy redder in color. However, there is also the effect of galaxy clusters accumulating more mass with time, rendering their gravitational potential wells deeper and, in theory, making them more efficient at quenching galaxies.

Seemingly contradictory is the bottom panel of Figure 3.22 which shows a distinct lack of noticeable relationship between red fraction and richness. We must consider, though, that this is only valid for clusters within our limited redshift and richness window. Quenching is likely to be richness dependent on smaller scales than redMaPPer is sensitive to, and by the time clusters have grown large enough for redMaPPer to detect them, most galaxies have already been quenched.

We then turned to cluster-centric radius d_{BCG} to probe the relationship between local environment within clusters and red fraction. We know from the mass density profiles of galaxy clusters (see Figure 4.2 for a couple examples) that the density within a galaxy cluster varies with radius, peaking at the cluster's centroid and falling to the field value as radius increases. The bottom panel of Figure 4.8 shows how red

fraction quickly spikes at some threshold when entering a cluster and then effectively plateaus. We interpret this as a sign of ram pressure stripping's relative dominance as a quenching mechanism in our high richness, low redshift cluster population.

Now we consider the evolution of GDR with redshift. The top panels of Figures 3.24 and 4.9 show how GDR increases with redshift. This relationship supports the downsizing paradigm for galaxy cluster formation, in which clusters are first populated by bright, massive galaxies which are quickly exhausted of star-forming materials. These massive galaxies within the cluster core accrete increasingly small and faint galaxies over time, and this is how the red sequence is assembled.

The bottom panel of Figure 3.24 displays the relationship between GDR and cluster richness λ. There is no noticeable relationship between them, at least for our limited redshift and richness windows. It is entirely possible, though, that richness affects GDR for smaller clusters and groups.

Finally, we observe the bottom panel of Figure 4.9 which illustrates the relationship between GDR and cluster-centric radius d_{BCG}. We see that the GDR spikes dramatically near the core of the cluster and quickly drops to the field value with increasing d_{BCG}. This spiking tendency becomes more pronounced with increasing redshift. The implication is that the giant red sequence galaxies within a cluster are heavily concentrated toward the center of the cluster. This is intuitive when we consider that dynamical friction is more effective for more massive galaxies, leading them to quickly spiral in to the center of their clusters' gravitational potential wells.

Taken together, these observations tell a story of galaxy evolution in clusters. At early times, massive galaxies were gravitationally attracted to areas of slight overdensity in the universe. As these large, bright galaxies stopped forming stars, they became the foundation of the red sequences in their clusters. Over time, clusters grew by accreting smaller and smaller galaxies; these galaxies experienced quenching. While most of the quenching was completed by the time clusters reached our redshift range, the un-quenched galaxies at low redshifts are likely to be strongly affected by ram pressure stripping when they encounter clusters' ICM. Dynamical friction becomes more efficient with increasing mass, and so massive galaxies quickly spiraled into the densest regions in the center of their clusters' gravitational potential wells. This caused massive galaxies to fall to the center of their clusters where quenching efficiency is high; smaller galaxies, on the other hand, are slower to spiral in and so are more likely to be found in the outskirts of their clusters, where we found the quenching efficiency to be lower.

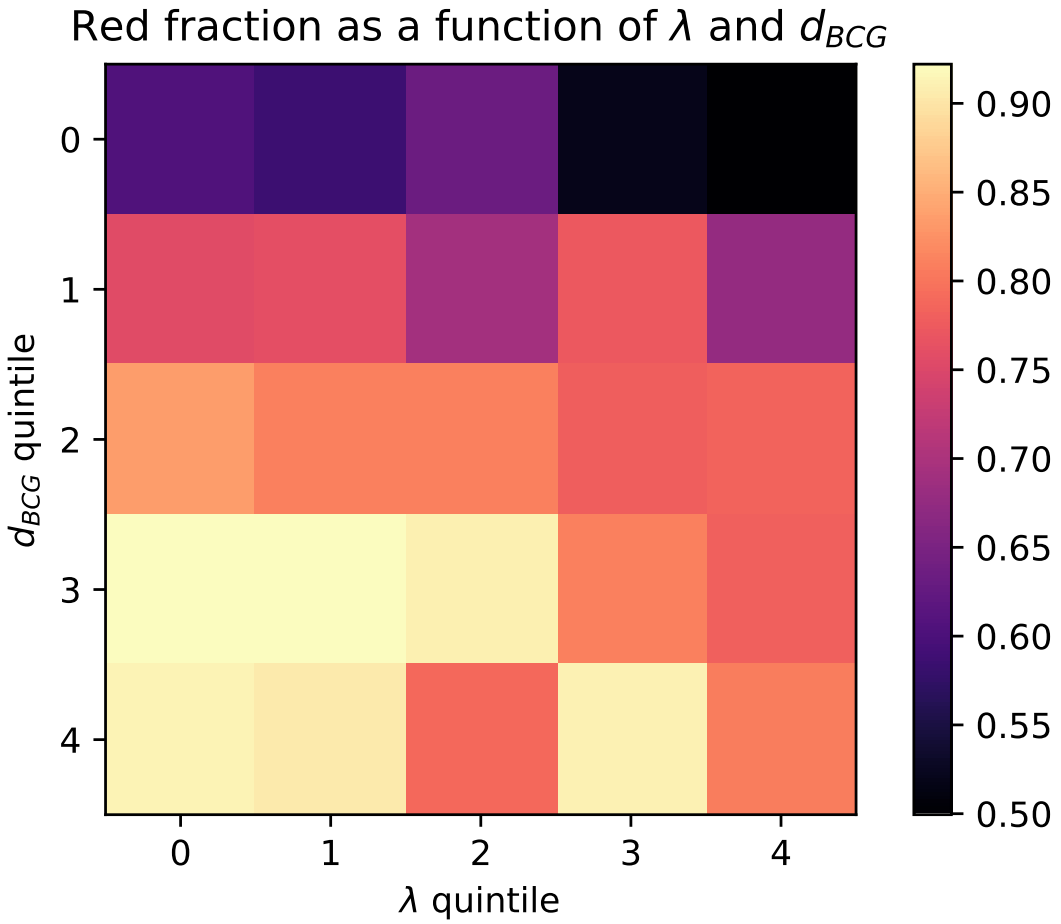

Figure 5.1: Red fraction as a function of λ and d_{BCG} in our central redshift bin $0.353 \leq z < 0.3936$. Note that the quintiles are numbered in order from high to low, so the bottom left cell represents the galaxies closest to their BCGs in the richest clusters.

Our results allow us compare the relative effect of local and global environment within our limited redshift and richness windows. Note that with our dataset, it is possible to make this comparison in a preliminary manner, but any more detailed comparison would require an improved dataset (see Section 5.2 for ways the dataset could be improved). Figure 5.1 shows red fraction as a function of λ and d_{BCG} in our central redshift bin $0.353 \leq z < 0.3936$. This plot was created for all redshift bins, but for clarity we will focus on this redshift bin only. Quintiles are numbered in order from high to low, so, for example, the 4th d_{BCG} quintile represents the 20% of galaxies closest to their associated BCGs (equivalently, the 20% of galaxies with lowest d_{BCG}). Meanwhile, the 0th λ quintile represents galaxies in the top 20% of richness. Therefore, the bottom left corner of the plot represents galaxies closest to their associated BCG and in the richest clusters. We see that, as expected, galaxies in the regions closest to the BCG and within the richest clusters exhibit the highest red fraction, implying that quenching is most effective in this environment. The figure shows more noticeable variation along the d_{BCG} axis than along the λ axis; while both global and local environment play a role in determining the red fraction within our population of clusters, local environment's effect appears to be somewhat more significant.

Figure 5.2 is the equivalent of Figure 5.1, this time for GDR rather than red fraction. It is difficult to perceive much of a relationship between GDR, d_{BCG}, and λ. This is not unexpected when we consider how quickly GDR drops off with radius after peaking at the clusters' centroids. Indeed, considering the top panels of Figures 3.24 and 4.9, redshift seems to have the most dominant effect.

5.2 Suggestions for future work

There are several ways that this work could be expanded upon. The most impactful of these ways would be to use a dataset which is photometrically complete to a fainter apparent magnitude than SDSS's limit of r=14. With a sufficiently deep survey, it would become possible to use De Lucia et al. (2007)'s absolute GDR cutoff magnitude, and then a direct comparison with many other authors would be possible while maintaining the benefits of our large sample size. Additionally, a deeper survey would allow us to study clusters at higher redshift, which would be interesting as we would be able to see more of the red sequence's formation. This would require an updated redMaPPer catalog to be created using the new survey, however.

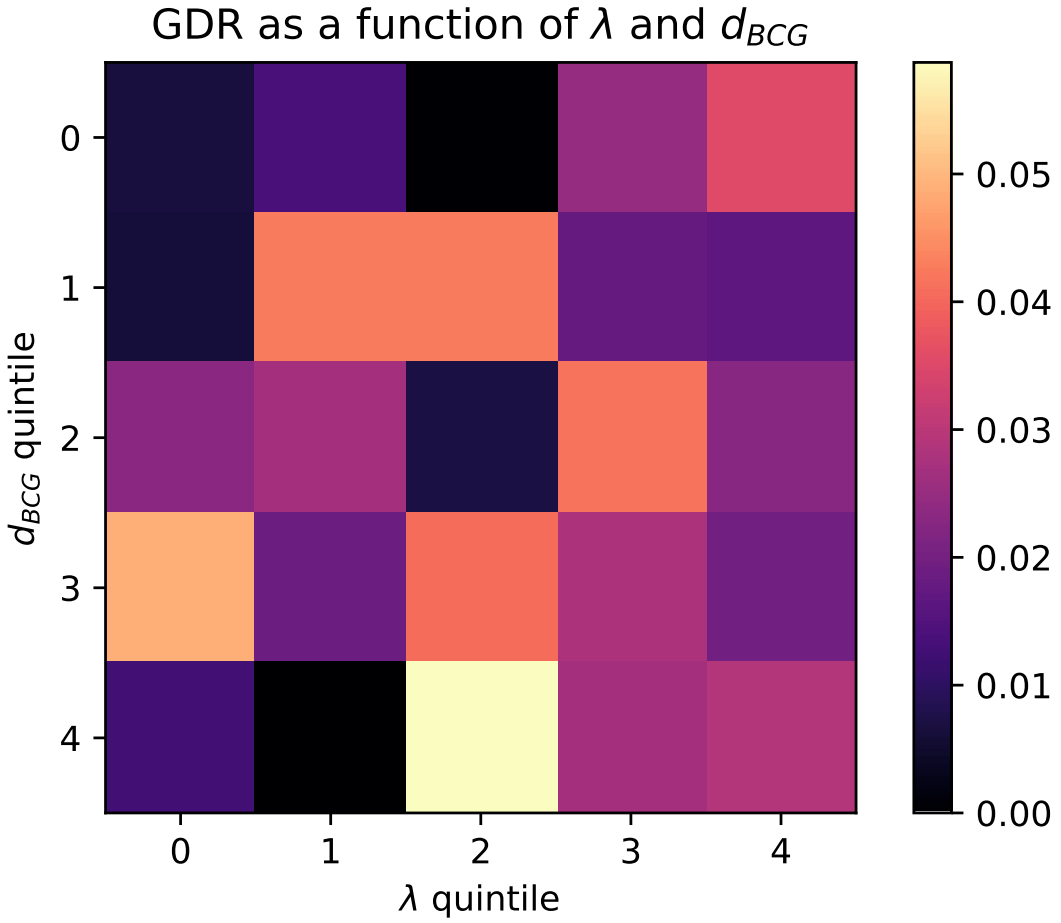

Figure 5.2: GDR as a function of λ and d_{BCG} in our central redshift bin $0.353 \leq z < 0.3936$. Note that the quintiles are numbered in order from high to low, so the bottom left cell represents the galaxies closest to their BCGs in the richest clusters.

It would also be useful to have a large survey of spectroscopically observed cluster member galaxies. The galaxies' spectra would allow us to determine the galaxies' redshifts; we could then unambiguously determine which galaxies belong to each cluster. With a spectroscopic survey, we could determine the red fraction and GDR of clusters with greater precision; however, as discussed above, if the survey was not complete to a fainter apparent magnitude than SDSS, we would not be sensitive to any new phenomena and our results would be essentially unchanged.

Another improvement could come with identifying the virial radius of each cluster and measuring red fraction and GDR as a function of virial radius rather than distance in kpc. This would account for the different physical scales of clusters and allow us to better isolate the effects of redshift, richness, σ_5, and d_{BCG} on galaxy evolution within clusters. It would also have allowed us to compare our results for GDR versus d_{BCG} directly with Barkhouse et al. (2007)'s measurements of M^* versus cluster-centric radius. This data is not available for the large number of galaxies used in this study, but in the future this may become a possibility.

It would also be interesting to analyze the results of a cluster-finding algorithm that is sensitive to clusters of lower richness than redMaPPer is, particularly if this new survey were able to detect over-densities on a group scale. This would allow us to see more quenching in action; currently, we only have access to clusters so rich that almost all of their galaxies have already been quenched in smaller-scale clusters or groups. We would expect to see a much more significant trend in red fraction versus richness in this case, and this could further constrain the possibilities of different quenching mechanisms being dominant in various environments.

Bibliography

Abadi M. G., Moore B., Bower R. G., 1999, Monthly Notices of the Royal Astronomical Society, Volume 308, Issue 4, pp. 947-954., 308, 947

Abraham R. G., et al., 1996, , 471, 694

Andreon S., 2008, Monthly Notices of the Royal Astronomical Society

Aragon-Salamanca A., Ellis R. S., Couch W. J., Carter D., 1993, Monthly Notices of the Royal Astronomical Society, 262, 764

Baldry I. K., Glazebrook K., Brinkmann J., Ivezić Ž., Lupton R. H., Nichol R. C., Szalay A. S., 2004, The Astrophysical Journal, 600, 681

Baldry I. K., Balogh M. L., Bower R. G., Glazebrook K., Nichol R. C., Bamford S. P., Budavari T., 2006, Monthly Notices of the Royal Astronomical Society, Volume 373, Issue 2, pp. 469-483., 373, 469

Balogh M. L., Baldry I. K., Nichol R., Miller C., Bower R., Glazebrook K., 2004, The Astrophysical Journal, Volume 615, Issue 2, pp. L101-L104., 615, L101

Barkhouse W. A., Yee H. K. C., LopezCruz O., 2007, The Astrophysical Journal

Bell E. F., et al., 2004, The Astrophysical Journal, Volume 608, Issue 2, pp. 752-767., 608, 752

Bennett C. L., et al., 2012, The Astrophysical Journal Supplement Series, 208, 20

Bildfell C., et al., 2012, Monthly Notices of the Royal Astronomical Society, 425, 204

Blakeslee J. P., et al., 2009, The Astrophysical Journal, 694, 556

Bohringer H., et al., 2002, The Astrophysical Journal, 566, 93

Boselli A., et al., 2016, Astronomy & Astrophysics, Volume 587, id.A68, 17 pp., 587

Boselli A., et al., 2018, Astronomy & Astrophysics, 614, A56

Butcher H., Oemler A. J., 1978, The Astrophysical Journal, 226, 559

Butcher H., Oemler A. J., 1984, The Astrophysical Journal, 285, 426

Capozzi D., Collins C. A., Stott J. P., 2010, Mon. Not. R. Astron. Soc, 403, 1274

Cavaliere A., Colafrancesco S., 1989, Springer, Dordrecht, pp 73–92, doi:10.1007/978-94-009-0903-8˙6, http://www.springerlink.com/index/10.1007/978-94-009-0903-8{_}6

Chung A., van Gorkom J. H., Kenney J. D. P., Vollmer B., 2007, The Astrophysical Journal, Volume 659, Issue 2, pp. L115-L119., 659, L115

Collaboration T. D. E. S., 2005

Collaboration L. D. E. S., 2012

Conroy C., Gunn J. E., 2010, Astrophysical Journal, 712, 833

Conroy C., Gunn J. E., White M., 2009, Astrophysical Journal, 699, 486

Cox T. J., Jonsson P., Somerville R. S., Primack J. R., Dekel A., 2007, Monthly Notices of the Royal Astronomical Society, Volume 384, Issue 1, pp. 386-409., 384, 386

De Lucia G., et al., 2007, Monthly Notices of the Royal Astronomical Society, 374, 809

Del Popolo A., Le Delliou M., Lee X., 2019, Physics of the Dark Universe, 26

Di Matteo P., Combes F., Melchior A. L., Semelin B., 2007, Astronomy and Astrophysics, Volume 468, Issue 1, June II 2007, pp.61-81, 468, 61

Djorgovski S. G., Mahabal A. A., Drake A. J., Graham M. J., Donalek C., 2012, Technical report, Sky Surveys, http://heasarc.nasa.gov/docs/heasarc/fits.html. http://heasarc.nasa.gov/docs/heasarc/fits.html

Dressler A., Oemler, Augustus J., Sparks W. B., Lucas R. A., 1994, The Astrophysical Journal, 435, L23

Eisenstein D. J., et al., 2011, The Astronomical Journal, 142, 72

F. Meekins J., Fritz G., A. Chubb T., Friedman H., Henry R., 1971, Nature, 231, 107

Fairley B. W., Jones L. R., Wake D. A., Collins C. A., Burke D. J., Nichol R. C., Romer A. K., 2002, , 330, 755

Fisenko A. I., Lemberg V. F., 2018, Astrophysics and Space Science, 363, 224

Foley R. J., et al., 2011, The Astrophysical Journal, 731, 86

Forman W., Kellogg E., Gursky H., Tananbaum H., Giacconi R., 1972, The Astrophysical Journal, 178, 309

Fukugita M., Ichikawa T., Gunn J. E., Doi M., Shimasaku K., Schneider D. P., 1996, The Astronomical Journal, 111, 1748

Gal R. R., de Carvalho R. R., Odewahn S. C., Djorgovski S. G., Margoniner V. E., 2000, The Astronomical Journal, 119, 12

Gavazzi R., Soucail G., 2006, Astronomy & Astrophysics, 462, 459

Geller M. J., Huchra J. P., 1989, Science (New York, N.Y.), 246, 897

Gilbank D. G., Balogh M. L., 2008, Tracking down a critical halo mass for killing galaxies through the growth of the red sequence, doi:10.1111/j.1745-3933.2008.00445.x

Giodini S., et al., 2009, The Astrophysical Journal, Volume 703, Issue 1, pp. 982-993 (2009)., 703, 982

Gioia I. M., Luppino G. A., 1994, The Astrophysical Journal Supplement Series, 94, 583

Gladders M. D., Yee H. K. C., Majumdar S., Barrientos L. F., Hoekstra H., Hall P. B., Infante L., 2007, The Astrophysical Journal, 655, 128

Gunn J. E., Gott J. Richard I., 1972, The Astrophysical Journal, 176, 1

Gunn J. E., et al., 1998, The Astronomical Journal

Gursky H., Solinger A., Kellogg E. M., Murray S., Tananbaum H., Giacconi R., Cavaliere A., 1972, The Astrophysical Journal, 173, L99

Hansen S. M., Sheldon E. S., Wechsler R. H., Koester B. P., 2009, Astrophysical Journal

Hao J., et al., 2009, The Astrophysical Journal, 702, 745

Hollowood D. L., et al., 2019, , 244, 22

Hubble E. P., 1925, The Observatory, Vol. 48, p. 139-142 (1925), 48, 139

Hubble E. P., 1926, The Astrophysical Journal, 64, 321

Hubble E., Humason M. L., 1931, The Astrophysical Journal, 74, 43

Jian H.-Y., et al., 2017, The Astrophysical Journal, 845, 74

Jung S. L., Choi H., Wong O. I., Kimm T., Chung A., Yi S. K., 2018, The Astrophysical Journal, 865, 156

Kaiser N., Squires G., Broadhurst T., 1995, , 449, 460

Kawata D., Mulchaey J. S., 2008, The Astrophysical Journal, 672, L103

Kellogg E., Murray S., Giacconi R., Tananbaum T., Gursky H., 1973, The Astrophysical Journal, 185, L13

Kodama T., Bower R. G., 2001, Monthly Notices of the Royal Astronomical Society, 321, 18

Kravtsov A. V., Borgani S., 2012, Annual Review of Astronomy and Astrophysics, 50, 353

Lavoie S., et al., 2016, , 462, 4141

Lin Y., Mohr J. J., 2004, The Astrophysical Journal, 617, 879

Lin Y.-T., Stanford S. A., Eisenhardt P. R. M., Vikhlinin A., Maughan B. J., Kravtsov A., 2011, The Astrophysical Journal Letters, Volume 745, Issue 1, article id. L3, 5 pp. (2012)., 745

Łokas E. L., Mamon G. A., 2003, Monthly Notices of the Royal Astronomical Society, 343, 401

Lu T., Gilbank D. G., Balogh M. L., Bognat A., 2009, Monthly Notices of the Royal Astronomical Society

Makino J., Hut P., 1997, The Astrophysical Journal, 481, 83

Marriage T. A., et al., 2010, The Astrophysical Journal, Volume 737, Issue 2, article id. 61, 10 pp. (2011)., 737

McLaughlin D. E., 1998, The Astrophysical Journal, 512, L9

Mehrtens N., et al., 2012, Monthly Notices of the Royal Astronomical Society, 423, 1024

Mei S., et al., 2006, The Astrophysical Journal, Volume 644, Issue 2, pp. 759-768., 644, 759

Mei S., et al., 2007, The Astrophysical Journal, Volume 655, Issue 1, pp. 144-162., 655, 144

Messier C., 1783, Connaissance des temps pour l'anne, p. 225254

Messier C., 1784, Connaissance des temps pour l'anne, p. 227272

Miyazaki S., et al., 2002, The Astrophysical Journal, Volume 580, Issue 2, pp. L97-L100., 580, L97

Moore B., Katz N., Lake G., Dressler A., Oemler A., 1995, Nature, Volume 379, Issue 6566, pp. 613-616 (1996)., 379, 613

Muzzin A., et al., 2009, The Astrophysical Journal, 698, 1934

Norberg P., et al., 2002, Monthly Notices of the Royal Astronomical Society, 336, 907

Nulsen P. E. J., Bohringer H., 1995, Monthly Notices of the Royal Astronomical Society, 274, 1093

Odegard N., Weiland J. L., Fixsen D. J., Chuss D. T., Dwek E., Kogut A., Switzer E. R., 2019

Pimbblet K. A., Smail I., Kodama T., Couch W. J., Edge A. C., Zabludoff A. I., O'Hely E., 2002, Monthly Notices of the Royal Astronomical Society, 331, 333

Planck Collaboration et al., 2018

Poggianti B. M., et al., 2016, The Astronomical Journal, 151, 78

Postman M., Lubin L. M., Gunn J. E., Oke J. B., Hoessel J. G., Schneider D. P., Christensen J. A., 1996, Astronomical Journal v.111, p.615, 111, 615

Price-Whelan A. M., et al., 2018, The Astronomical Journal, 156, 123

Reichardt C. L., et al., 2012, The Astrophysical Journal, 763, 127

Rines K. J., Geller M. J., Diaferio A., Hwang H. S., 2016, The Astrophysical Journal

Robitaille T. P., et al., 2013, Astronomy & Astrophysics, Volume 558, id.A33, 9 pp., 558

Rozo E., Rykoff E., Koester B., Nord B., Wu H.-Y., Evrard A., Wechsler R., 2011, The Astrophysical Journal, 740, 53

Rykoff E. S., et al., 2012, Astrophysical Journal

Rykoff E. S., et al., 2014, The Astrophysical Journal, 785, 104

Sanderson A. J., Edge A. C., Smith G. P., 2009, Monthly Notices of the Royal Astronomical Society, 398, 1698

Sarazin C. L., 1986, Reviews of Modern Physics, 58, 1

Schindler S., Binggeli B., Boehringer H., 1998

Smith S., Sinclair 1936, The Astrophysical Journal, 83, 23

Stanford S. A., Eisenhardt P. R., Dickinson M., 1998, The Astrophysical Journal, 492, 461

Staniszewski Z., et al., 2008, The Astrophysical Journal, 701, 32

Stern C., et al., 2018, Monthly Notices of the Royal Astronomical Society, 485, 69

Stott J. P., Smail I., Edge A. C., Ebeling H., Smith G. P., Kneib J., Pimbblet K. A., 2007, The Astrophysical Journal

Struble M. F., Rood H. J., 2002, The Astrophysical Journal Supplement Series

Su Y., et al., 2019, The Astronomical Journal

Sunyaev R. A., Zeldovich Y. B., 1970, Astrophysics and Space Science, Volume 7, Issue 1, pp.3-19, 7, 3

Sunyaev R. A., Zeldovich Y. B., 1972, Comments on Astrophysics and Space Physics, Vol. 4, p.173, 4, 173

Sunyaev R. A., Zel'dovich Y. B., 1980, Annual Review of Astronomy and Astrophysics, 18, 537

Tanaka M., Kodama T., Arimoto N., Okamura S., Umetsu K., Shimasaku K., Tanaka I., Yamada T., 2005, Monthly Notices of the Royal Astronomical Society, 362, 268

Thanjavur K., Willis J., Crampton D., 2009, The Astrophysical Journal, 706, 571

Urban O., Werner N., Simionescu A., Allen S. W., Böhringer H., 2011, Monthly Notices of the Royal Astronomical Society, 414, 2101

Urquhart S. A., Willis J. P., Hoekstra H., Pierre M., 2010, Monthly Notices of the Royal Astronomical Society, 406, 368

Vanderlinde K., et al., 2010, The Astrophysical Journal, 722, 1180

Veilleux S., Cecil G., Bland-Hawthorn J., 2005, Annual Review of Astronomy and Astrophysics, 43, 769

Visvanathan N., Sandage A., 1977, The Astrophysical Journal, 216, 214

Wake D. A., Collins C. A., Nichol R. C., Jones L. R., Burke D. J., 2005, The Astrophysical Journal, 627, 186

Willis J. P., et al., 2005,] 10.1111/j.1365-2966.2005.09473.x, 363, 675

Willis J. P., Ramos-Ceja M. E., Muzzin A., Pacaud F., Yee H. K. C., Wilson G., 2018, Monthly Notices of the Royal Astronomical Society, 477, 5517

Wilson G., et al., 2009, Astrophysical Journal, 698, 1943

Wittman D., Dell'Antonio I. P., Hughes J. P., Margoniner V. E., Tyson J. A., Cohen J. G., Norman D., 2005, The Astrophysical Journal, 643, 128

Yang X., Mo H. J., van den Bosch F. C., Pasquali A., Li C., Barden M., 2007,] 10.1086/522027

York D. G., et al., 2000, The Astronomical Journal, 120, 1579

Zwicky F., 1937, The Astrophysical Journal, 86, 217

Zwicky F., Andernach H., 1933

de Vaucouleurs G., Gerard 1961, The Astrophysical Journal Supplement Series, 5, 233

van Dokkum P. G., Franx M., Fabricant D., Kelson D. D., Illingworth G. D., 1999, The Astrophysical Journal, 520, L95